Dear Reader,

Thank you for your interest in this paper. This manuscript has been **accepted for publication** in ***Quaternary Science Reviews*** as an invited research article as of **June 8, 2020** after initial submission on December 8, 2019. The version uploaded here to EarthArXiv represents a revised version of the manuscript after peer review. The final typeset version of this manuscript is accessible via the 'Peer-reviewed publication DOI' link on the right-hand side of the webpage.

If the content of this preprint has informed your thinking on your own work, we ask that you cite our paper using the following citation, using the format appropriate for your journal:

```
Chen, C. Y., McGee, D., Woods, A., Pérez, L., Hatfield, R. G., Edwards, R.
L., Cheng, H., Valero-Garcés, B. L., Lehmann, S. B., Stoner, J. S., Schwalb,
A., Tal, I., Seltzer, G. O., Tapia, P. M., Abbott, M.A., Rodbell, D. T.
(2020). U-Th dating of lake sediments: Lessons from the 700 ka sediment
record of Lake Junín, Peru. Quaternary Science Reviews. 244: 106422. doi:
10.1016/j.quascirev.2020.106422
```

We would also like to highlight that the data and tools associated with this publication are freely available on the open-access data repository Zenodo: https://doi.org/10.5281/zenodo.3788100

For more information on EarthArXiv, visit the following sites:

- FAQs: https://eartharxiv.github.io/faq.html
- EOS article: https://eos.org/science-updates/earth-science-is-ready-for-preprints

We have elected to make our manuscript available on EarthArXiv in the spirit of open science. Therefore, we welcome you to contact the lead author, **Christine Y. Chen** (cychen[at]caltech[dot]edu) with any feedback to help improve the manuscript.

Happy reading!

Sincerely,
Christine Y. Chen and co-authors

This page is intentionally left blank.

U-Th dating of lake sediments: Lessons from the 700 ka sediment record of Lake Junín, Peru

Christine Y. Chen[a,b,*], David McGee[b], Arielle Woods[c], Liseth Pérez[d], Robert G. Hatfield[e,f], R. Lawrence Edwards[g], Hai Cheng[h,i,g], Blas L. Valero-Garcés[j,k], Sophie B. Lehmann[c], Joseph S. Stoner[f], Antje Schwalb[d], Irit Tal[b], Geoffrey O. Seltzer[l,**], Pedro Miguel Tapia[m], Mark B. Abbott[c], Donald T. Rodbell[n]

[a] *Massachusetts Institute of Technology-Woods Hole Oceanographic Institution Joint Program in Oceanography, Cambridge, MA, USA*
[b] *Department of Earth, Atmospheric and Planetary Sciences, Massachusetts Institute of Technology, Cambridge, MA, USA*
[c] *Department of Geology and Environmental Science, University of Pittsburgh, Pittsburgh, PA, USA*
[d] *Institut für Geosysteme und Bioindikation, Technische Universität Braunschweig, Braunschweig, Germany*
[e] *Department of Geological Sciences, University of Florida, Gainesville, FL, USA*
[f] *College of Earth, Ocean, and Atmospheric Science, Oregon State University, Corvallis, OR, USA*
[g] *Department of Earth and Environmental Sciences, University of Minnesota Twin Cities, Minneapolis, MN, USA*
[h] *Institute of Global Environmental Change, Xi'an Jiaotong University, Xi'an, China*
[i] *State Key Laboratory of Loess and Quaternary Geology, Institute of Earth E¬nvironment, Chinese Academy of Sciences, Xi'an, China*
[j] *Pyrenean Institute of Ecology, CSIC, Avda Montañana 1005, 50059, Zaragoza, Spain*
[k] *Laboratorio Internacional en Cambio Global, CSIC-PUC-UFRJ, Zaragoza, Spain*
[l] *Department of Earth Sciences, Syracuse University, Syracuse, NY, USA*
[m] *Instituto Nacional de Investigación en Glaciares y Ecosistemas de Montañas, Huaraz, Ancash, Peru*
[n] *Department of Geology, Union College, Schenectady, NY, USA*

Abstract

Deep sediment cores from long-lived lake basins are fundamental records of paleoenvironmental history, but the power of these reconstructions has been often limited by poor age control. Uranium-thorium (U-Th) dating has the potential to fill a gap in current geochronological tools available for such sediment archives. We present our systematic approach to U-Th date carbonate-rich sediments from the ∼100 m drill core from Lake Junín, Peru. The results form the foundation of an age-depth model spanning ∼700 kyrs. High uranium concentrations (0.3–4 ppm) of these sediments allow us to date smaller amounts of material, giving us the opportunity to improve sample selection by avoiding detrital contamination, the greatest factor limiting the success of previous U-Th dating efforts in other lake basins. Despite this advantage, the dates from 174 analyses on 55 bulk carbonate samples reveal significant scatter that cannot be resolved with traditional isochrons, suggesting that at least some of the sediments have not remained closed systems. To understand the source of noise in the geochronological data, we first apply threshold criteria that screen samples by their U/Th ratio, reproducibility, and $\delta^{234}U_{initial}$ value. We then compare these results with facies types, trace element concentrations, carbonate and total organic carbon content, color reflectance, mineralogy,

*Corresponding author. Currently at the Division of Geological and Planetary Sciences, California Institute of Technology, CA, USA. Email address: cychen@caltech.edu (C. Y. Chen).
**Deceased.

and ostracode shell color to investigate the causes of open system behavior. Alongside simulations of the isotopic evolution of our samples, we find that the greatest impediment to U-Th dating of these sediments is not detrital contamination, but rather post-depositional remobilization of uranium. Examining U-Th data in these contexts, we identify samples that have likely experienced the least amount of alteration, and use dates from those samples as constraints for the age-depth model. Our work has several lessons for future attempts to U-Th date lake sediments, namely that geologic context is equally important as the accuracy and precision of analytical measurements. In addition, we caution that significant geologic scatter may remain undetected if not for labor intensive tests of reproducibility achieved through replication. As a result of this work, the deep sediment core from Lake Junín is the only continuous record in the tropical Andes spanning multiple glacial cycles that is constrained entirely by independent radiometric dates.

Keywords: Quaternary; Paleoclimatology; South America; U-Th series; Sedimentology, lakes lagoons & swamps; Geochronology; ICDP; age model

---

1. Introduction

Since the founding of the International Continental Scientific Drilling Program (ICDP) in 1996 (Colman, 1996), scientific teams have recovered dozens of deep lake sediment cores from nearly every continent in the world. Due to their continuity, resolution, and wide geographic distribution, these sediment records have provided important long-term perspectives on Earth's terrestrial environmental history. As the spatial and temporal coverage of such records expand, the next step is to combine these records with complementary work from marine and ice cores to reveal linkages among terrestrial, marine, and atmospheric phenomena. Here, the challenge lies in comparing the timing of past land surface changes to those of past events identified elsewhere. Thus, tests of causal relationships between different parts of the climate system are often limited by the quality of the temporal constraints.

While ice and marine cores are often amenable to layer counting or anchoring to globally synchronous reference timescales (e.g., oxygen isotope "chronostratigraphy" in marine sediments, methane gas concentrations in ice cores), determining a reliable age-depth model for long lacustrine sediment sequences is more problematic. Because lake basins occupy a broad range of environments, each drilling location contains a site-specific accumulation of terrigenous and biogenic sediment and a unique post-depositional alteration history influenced by non-climatic processes like tectonics and volcanism. Thus, aligning such records to external reference timescales—colloquially known as "tuning"—requires a thorough investigation of how proximal geologic processes affect local paleoenvironmental proxies before connections to global climate events can be made. Proving such relationships can be a formidable undertaking, but in the absence of other data, tuning is often the only means available to establish time constraints. As a result, such records are limited in their ability to address climatic questions that are dependent on the relative timing of events (e.g., Prokopenko et al., 2006; Nowaczyk et al., 2013; Stockhecke et al., 2014; Francke et al., 2016).

Therefore, absolute chronological data from radiometric and paleomagnetic dating techniques are desirable and serve as first-order constraints on age-depth models of sediment cores. The success of such methods are dependent on factors such as the availability and quality of datable materials, the time range of the method, and the adherence to assumptions underpinning each technique within a given sediment sequence. When these factors align, the resulting independent chronologies allow for compelling investigations of forcing relationships (e.g., the radiocarbon- and

tephra-based chronologies of Laguna Potrok Aike in Patagonia [Kliem et al., 2013] and Lake Petén Itzá in Guatemala [Kutterolf et al., 2016]). However, problems commonly arise when suitable dating materials are absent or the true age of the sediments is outside the applicable temporal range of a method: for instance, datable tephras are rare in most environments and the radiocarbon method is limited to the last 50 ka.

Currently, there exists a gap in comprehensively tested high-precision geochronological tools for sediments in the time interval between 50 and 780 ka, beyond the limit of radiocarbon dating and up to the most recent geomagnetic reversal (Brunhes–Matuyama). Here, methods like uranium-thorium (U-Th), cosmogenic exposure, and optically stimulated luminescence (OSL) dating have potential (e.g., Roberts et al., 2018). However, these systems have been underexplored in their broad application to lake sediments compared to their more popular application to substrates like stalagmites, glacial moraines, and fluvial deposits. Ideally, data from multiple complementary chronological tools with different operating assumptions can be used to cross-validate one another (e.g., Colman et al., 2006; Shanahan et al., 2013), and in the process, reveal information about the nature of uncertainties and biases specific to each technique.

To this end, we present our efforts to U-Th date the carbonate-rich sediments from the deep drill core extracted in 2015 from Lake Junín, Peru. Our strategy for sample selection, tests for internal consistency that leverage stratigraphic coevality constraints, and use of other corresponding data to inform our geochronological interpretations can serve as a framework for future attempts to apply U-Th dating techniques to long cores. Our results also indicate that future work to establish or refine U-Th-based lake sediment chronologies must include deliberate tests that probe for possible open system behavior or excess "geologic scatter"—unresolved errors that can affect the accuracy and precision of dates due to unknown geologic complexities not accounted for in typical uncertainty calculations and corrections (Ludwig and Paces, 2002). Without a methodical exploration of U-Th data in context of other geologic information, age-depth models that contain single, standalone U-Th analyses that, at face value, seem like valid ages, may in fact hide the existence of geologic scatter and therefore be inaccurate.

The organization of this paper is as follows: we first provide a basic overview of the principles behind U-Th dating and review previous efforts to apply U-Th geochronology to lake sediments (Section 2). After describing the relevant background of Lake Junín (Section 2.3) and our methods for core sampling, U-Th geochemistry, and isotopic measurement (Section 3), we present the results of 174 U-Th analyses from 55 unique samples (Section 4). Of these, only 72 analyses from 18 samples are used in the final chronology for the core. We explain our screening procedure for evaluating the validity of each U-Th date (Section 5), and then interpret our analyses alongside other sedimentological, geochemical, and paleoecological data to show that uranium remobilization, not detrital contamination, is the most likely cause for excess scatter in our data (Section 6). We then simulate the impact of detrital contamination and uranium remobilization on the isotopic evolution of our samples to test this hypothesis (Section 7). Using the U-Th age constraints that pass our criteria and radiocarbon dates from Woods et al. (2019), we then describe the construction of the age-depth model for the Lake Junín sediment record (Section 8). We end with a discussion on the uncertainties in U-Th age estimates learned from this study and propose considerations for future U-Th dating of lake sediments (Section 9).

Hereafter, we distinguish between the terms *date* and *age*, adopting the convention followed by other geochronologists (e.g., Schoene et al., 2013; Dutton et al., 2017): a date is a number calculated from a decay equation and isotopic measurements, whereas an age is an interpretation of a date in the context of other information and represents a geologically meaningful time.

2. Background

The application of U-Th dating in continental paleoclimate archives has been most visible and transformative in unrecrystallized corals and dense carbonate precipitates like cave stalagmites and groundwater vein calcites (e.g., Winograd et al., 1992; Cheng et al., 2000; Wang et al., 2001). In comparison, U-Th dating of lake sediments has been less straightforward, challenging many geochronologists to devise creative solutions to dating these non-ideal substrates. To contextualize the challenges of our work, in this section, we briefly describe the basic principles of U-Th dating, the geologic processes in lake sediments that can compromise the underlying assumptions of this dating system, and the strategies used by other studies to overcome or account for these issues.

2.1. Basic principles of U-Th dating

There are several "uranium-series disequilibrium" dating methods that make use of the decay chains of various nuclides (e.g., ^{238}U, ^{235}U; see Bourdon et al., 2003). Unlike other notable radiometric chronometers such as uranium-lead or potassium-argon, which compare the concentrations of a parent nuclide to that of its stable daughter product, uranium-series disequilibrium dating schemes instead compare the activity—the number of disintegrations per unit time per unit mass of a material—of a parent nuclide to those of their series of unstable daughter products. These methods estimate time by measuring the degree to which different daughter isotopes along a decay chain are out of *secular equilibrium*, a steady state in which the activity of both the parent and daughter nuclides are equal (i.e., the number of daughter nuclides forming is equal to the number of daughter nuclides decaying). Because the half-lives of the parent isotopes are much longer than that of all intermediate daughter products in these decay chains, a material containing the parent isotope that has remained unperturbed for several million years will have reached secular equilibrium (i.e., the activity ratio of the parent nuclide to its daughter product will be equal to 1).

Disturbances to this equilibrium caused by various natural geochemical processes form the basis of uranium-series disequilibrium dating. In this paper, we use the widely applied ^{230}Th-^{234}U-^{238}U disequilibrium dating method, for which "U-Th dating" commonly serves as shorthand (Fig. 1). This dating system takes advantage of the differences in solubility between uranium and thorium complexes in natural waters of surface environments: in oxic environments, uranium generally assumes its highest oxidation state (U^{6+}) in the form of the highly soluble uranyl ion (UO_2^{2+}), whereas thorium generally is insoluble and immobile in most aqueous environments where pH > 3, with some exceptions (Chabaux et al., 2003). Thus, in most surface conditions, fluids are enriched in uranium and depleted in thorium, and this extreme fractionation is preserved when precipitants form from such waters. Carbonates are the most widely utilized materials for U-Th dating due to their near ubiquity in continental waters. In addition, because UO_2^{2+} easily forms stable complexes with carbonate ions and is adsorbed onto, co-precipitated with, or structurally incorporated into carbonate mineral host phases (Langmuir, 1978; Reeder et al., 2000, 2001; Kelly et al., 2003, 2006), carbonates tend to have higher amounts of uranium than other precipitates, like halite.

After the initial fractionation, the isotopic system will follow the laws of radioactivity to restore equilibrium between the parent and daughter nuclides at a rate determined by their respective decay constants. Thus, the timing of precipitate formation is determined by measuring the extent to which daughter product growth has restored the system to secular equilibrium (i.e., the extent to which the activity ratio of the parent nuclide and its daughter product has returned to unity). Using measurements of relevant activity ratios, a date can then be calculated from decay equations and constants.

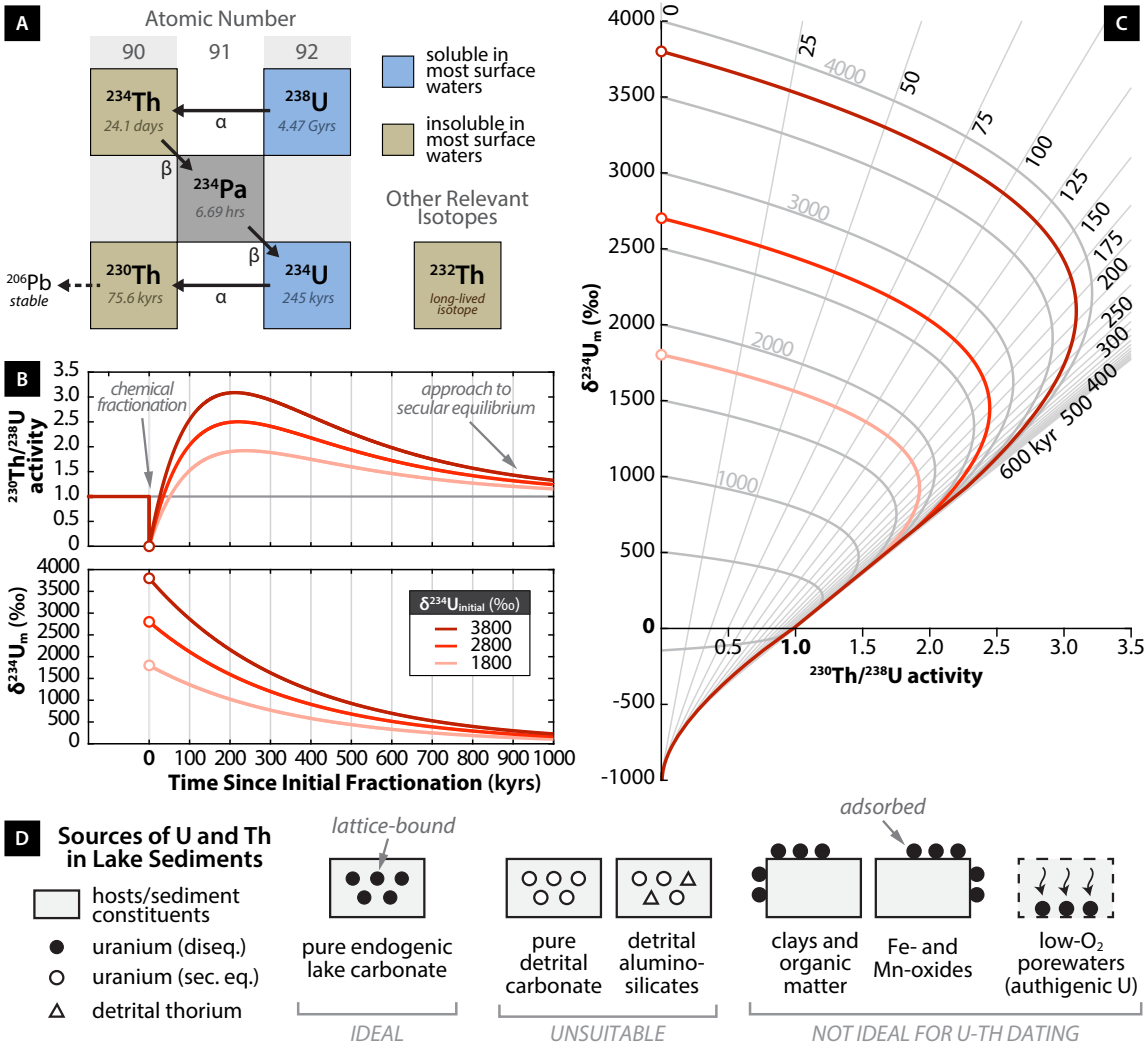

Figure 1: The basic principles of U-Th dating. [**A**] Schematic of the portion of the ^{238}U decay chain that is relevant for U-Th dating. The half-lives and type of particle emitted during radioactive decay (an α or β particle) of each isotope are shown. Ultimately, the decay chain ends with the stable ^{206}Pb. [**B**] and [**C**] Isotope evolution diagrams showing the change in ^{230}Th/^{238}U activity and measured δ^{234}U ($\delta^{234}U_m$)—the two ratios used for the calculation of U-Th dates—after initial fractionation (adapted from Edwards, 1988). The three thick red-shaded lines represent different pathways towards secular equilibrium based on the value of $\delta^{234}U_{initial}$ (see legend in bottom panel of B). Values shown are within the range of values observed in the Lake Junín sediments, but are otherwise arbitrary and selected purely for demonstration. Panel C plots the same curves in Panel B but in ^{230}Th/^{238}U activity-$\delta^{234}U_m$ space to show the graphical solution to the age equations. Hollow circles mark the initial isotopic composition of the sample. Straight gray lines represent solutions to the ^{230}Th age equation (Eq. 1, lines labeled in kyrs with black text) and curved gray contours represent solutions to the δ^{234}U equation (Eq. 2, some curves labeled with their $\delta^{234}U_{initial}$ in gray). [**D**] Schematic of uranium and thorium sources in lake sediments. Black circles represent uranium in ^{230}Th/^{238}U disequilibrium whereas white circles represent uranium in secular equilibrium. To simplify, the detrital carbonate and aluminosilicate constituents represent bedrock-derived material of old age (>2 Ma). The placement of circles and triangles within or around boxes represents how uranium and thorium are associated with each host: bound within the crystal lattice or adsorbed to the substrate surface. The box furthest to the right represents the low-oxygen porewater uranium sink, where uranium changes from a soluble to insoluble valence state and accumulates authigenically.

Two equations form the backbone of U-Th dating. The first is the ^{230}Th age equation:

$$\left[\frac{^{230}\mathrm{Th}}{^{238}\mathrm{U}}\right] - 1 = -e^{-\lambda_{230}t} + \left(\left[\frac{^{234}\mathrm{U}}{^{238}\mathrm{U}}\right] - 1\right)\left(\frac{\lambda_{230}}{\lambda_{230} - \lambda_{234}}\right)\left(1 - e^{-(\lambda_{230}-\lambda_{234})t}\right) \quad (1)$$

where square brackets around ratios indicate activity ratios; λ symbols are decay constants; and t is the date (Bateman, 1910; Broecker, 1963; see Edwards, 1988 and Ivanovich and Harmon, 1992 for derivation). The ^{234}U/^{238}U activity is more commonly expressed using delta (δ) notation, representing the deviation in parts per thousand (permil; ‰) of ^{234}U/^{238}U from secular equilibrium: $\delta^{234}\mathrm{U} = ([^{234}\mathrm{U}/^{238}\mathrm{U}]-1) \times 1000$. From this equation, it is clear that measuring three key isotopes—^{238}U, ^{234}U, and ^{230}Th—allows us to solve for t (Fig. 1A).

The term in Eq. 1 involving δ^{234}U exists to account for the enrichment of ^{234}U over ^{238}U commonly observed in natural waters (Thurber, 1962). This disequilibrium occurs because of the displacement of the daughter nuclide ^{234}Th due to recoil from the alpha decay of ^{238}U (Fig. 1A): around the radiation damaged site, ^{234}Th and its daughter product ^{234}U are preferentially leached from the host mineral during water-rock interactions, leading to disequilibrium between ^{234}U and ^{238}U (Kigoshi, 1971; Kronfeld, 1974; Fleischer, 1982; Chabaux et al., 2008). After solving for t using Eq. 1, we can use a second equation to determine the starting value of δ^{234}U at the time of fractionation ($\delta^{234}\mathrm{U}_{\mathrm{initial}}$):

$$\delta^{234}\mathrm{U}_{\mathrm{m}} = \left(\delta^{234}\mathrm{U}_{\mathrm{initial}}\right) e^{-\lambda_{234}t} \quad (2)$$

where the subscript m represents the present measured value. Thus, these two equations allow us to solve for two unknowns with the measurement of two isotopic ratios.

Fig. 1B shows the expected isotopic evolution of ^{230}Th/^{238}U activity and $\delta^{234}\mathrm{U}_{\mathrm{m}}$ over time, provided the system remains closed. Fig. 1C shows the graphical solution to Eqs. 1 and 2: the straight, sub-vertical lines represent solutions to the ^{230}Th age equation and the curved lines emanating from the y-axis are solutions to the δ^{234}U equation. Each straight line is a line of equal age and each curved line is a line of equal $\delta^{234}\mathrm{U}_{\mathrm{initial}}$ value. From this figure, two observations about this dating system can be made: (1) for a given analytical error, as the true age of the sample increases, so too does the uncertainty in the age estimate due to the increasing closeness of the age isolines; and (2) although both ^{230}Th/^{238}U and ^{234}U/^{238}U have not yet returned to their secular equilibrium values even after 1 Myrs, the age isolines eventually are so closely spaced that current levels of measurement precision cannot distinguish between a sample of a finite age and a sample of infinite age. Because of these limitations, the oldest application of U-Th dating is ~700 kyrs, thus far only achieved in well-preserved corals and cave deposits (Edwards et al., 2003; Stirling and Andersen, 2009; Cheng et al., 2016; Fig. 1A).

2.2. Previous work on U-Th dating of lake sediments

With the U-Th chronometer, a date is only interpretable as a meaningful age if the system meets the following criteria for *closed-system behavior*: (1) all decay products were absent at the time of formation, or can be corrected for if present; and (2) there was no gain or loss of any radionuclides after formation other than by radioactive decay. For U-Th dating of lake sediments, the most common obstacle is the lack of material that fulfill these criteria. Even carbonate-rich sediments remain difficult to date, as the carbonates often contain non-ideal constituents or have experienced post-depositional alteration due to various weathering, transport, and mixing processes common in lake basins (Fig. 1D).

Despite the challenge, geochronologists have devised ways to circumvent these issues. Table 1 is a list of lake sediment studies in which U-Th dating was applied, each with varying degrees of success. We distinguish between studies working with carbonates (e.g., calcite, aragonite) and evaporites (e.g., halite, gypsum), as these are the two most common materials used. Success has been limited primarily by the incorporation of detrital materials that introduce initial ^{230}Th, which increases uncertainties and, if not fully corrected for, potential inaccuracies. Detrital contamination usually is more problematic for non-carbonate evaporites like gypsum or halite because these materials typically have very low amounts of uranium derived from precipitating waters. The most common detrital materials found in carbonates and evaporites are clay particles (Fig. 1D). Attempts to chemically separate detritus from bulk sediment have been made, but selective acid leaches meant to isolate endogenic material from the detrital component also differentially fractionate the uranium and thorium isotopes in unpredictable ways (Bischoff and Fitzpatrick, 1991; Luo and Ku, 1991), making sequential acid leaching techniques for age determination ineffective in all but the most controlled experimental cases (Ku and Liang, 1984; Schwarcz and Latham, 1989).

Thus, most U-Th dating applications of lake sediments have applied corrections for detrital contamination by processing a series of coeval samples through total sample dissolution and then using "isochron" techniques. Here, the long-lived isotope ^{232}Th (Fig. 1A) acts as a tracer of contamination: assuming that the endogenic material contains no ^{232}Th or initial ^{230}Th, any detected ^{232}Th is attributed to the detrital component. For this reason, a sample with a higher measured ^{230}Th/^{232}Th or ^{238}U/^{232}Th ratio (more ^{238}U leads to more abundant ^{230}Th) is considered more "clean," while a sample with a lower measured ^{230}Th/^{232}Th or ^{238}U/^{232}Th ratio is considered "dirty" (colloquial terms used in the literature; e.g., Schwarcz and Latham, 1989; Przybylowicz et al., 1991; Stein and Goldstein, 2006).

By plotting the isotope ratios of several portions of a single sample that have varying amounts of detritus, a line fit through those analyses can pinpoint the isotope ratios of the endogenic material, and thus provide a date (e.g., Fig. S3; Osmond et al., 1970; Kaufman, 1971; Rosholt, 1976). The limit of this approach is that it is only applicable when there is a single, homogenized source of detritus with a consistent ^{230}Th/^{232}Th ratio forming one end member of the sample mixtures. Most studies listed in Table 1 apply this isochron method, but the process is labor intensive because at least three analyses are required for a date, and many more for one that is statistically rigorous (Powell et al., 2002). Nevertheless, if considerable effort is put towards multiple analyses and characterizing sources of detritus, the results can be rewarding (e.g., Haase-Schramm et al., 2004, Torfstein et al., 2013 in the Dead Sea).

In some cases where the measured ^{230}Th/^{232}Th ratio of sample material is sufficiently high, single-sample dates are possible by applying an initial ^{230}Th/^{232}Th correction,which defines the proportion by which detrital ^{230}Th is assumed to accompany ^{232}Th. The ^{230}Th age equation modified to correct for initial ^{230}Th is

$$\left\{\left[\frac{^{230}\mathrm{Th}}{^{238}\mathrm{U}}\right] - \left[\frac{^{232}\mathrm{Th}}{^{238}\mathrm{U}}\right]\left[\frac{^{230}\mathrm{Th}}{^{232}\mathrm{Th}}\right]_i \left(e^{-\lambda_{230}t}\right)\right\} - 1 = \\ - e^{-\lambda_{230}t} + \left(\left[\frac{^{234}\mathrm{U}}{^{238}\mathrm{U}}\right] - 1\right)\left(\frac{\lambda_{230}}{\lambda_{230}-\lambda_{234}}\right)\left(1 - e^{-(\lambda_{230}-\lambda_{234})t}\right), \quad (3)$$

where i refers to the initial value at the time of fractionation (Edwards et al., 1987). For impure carbonates, this detrital correction is usually the largest contributor to the uncertainty of the final date, having greatest effect on samples with low uranium or low ^{230}Th/^{232}Th ratios. The impact

Table 1: A list of sites and studies which used U-Th dating to develop an age model for a lacustrine sediment sequence. Also indicated are other types of age constraints used for age model construction, separated into two categories: *absolute constraints* and *other tie points*. In these columns, '1' indicates that the chronological tool played a primary, first-order role in the age model, whereas '2' indicates that the tool played a second-order role, used only after application of first-order data. If no number appears beneath a column, this indicates that the chronological tool was not used to construct the age model at the site. The contribution of U-Th dating to the chronology of each record varies but is always limited to the first ~600 ka of the record.

				ABSOLUTE CONSTRAINTS					OTHER TIE POINTS			
Site	**Country**	**Duration**	**References**	**^{14}C**	**U-Th[a]** *carb.*	*evap.*	*other*	**OSL[b]**	**pmag.[c]**	**tephra[d]**	**strata[e]**	**tuning[f]**
Lake Junín	Peru	~700 ka	this study	1	1							
Lake Igelsjön	Sweden	12 ka	Israelson et al. (1997)	1	1							
Babicora Basin	Mexico	65 ka	Metcalfe et al. (2002)	1			1[g]					
Salar de Atacama	Chile	106 ka	Bobst et al. (2001); Lowenstein et al. (2003)			1						
Lake Balikun	China	150 ka	Ma et al. (2004)		1				2			
Death Valley	USA	200 ka	Li et al. (1996); Ku et al. (1998)			1						
Searles Lake	USA	3 Ma	Peng et al. (1978); Bischoff et al. (1985); Lin et al. (1998)	1	1	1			1			
Qaidam Basin	China	4 Ma	Luo and Ku (1991); Phillips et al. (1993); Wang et al. (2013) and references therein	1		1			1			
Dead Sea	Israel	230 ka	Kaufman et al. (1992); Haase-Schramm et al. (2004); Stein and Goldstein (2006); Torfstein et al. (2015), references therein	1	1						1	1[h]
Bear Lake	USA	250 ka	Colman et al. (2006)	1	1				1			1[i]
Great Salt Lake	USA	280 ka	Balch et al. (2005)	1	1	1			1	1		
Lake Titicaca	USA	370 ka	Fritz et al. (2004, 2007)	1	1	1						1[j]
Lake Bosumtwi	Ghana	450 ka	Shanahan et al. (2013)	1	1			1	1		1	2[k]

[a]Applications of U-Th dating are separated into three categories based on material: carbonates ('carb.'), which includes minerals such as calcite and aragonite, and evaporites ('evap.'), which includes minerals such as halite and gypsum.

[b]'OSL' refers to optically stimulated luminescence dating.

[c]'pmag.' refers to matching paleomagnetic excursions, reversals, and changes in intensity to other records for age constraints.

[d]'tephra' refers to records that match tephras from the sediment sequence to well-dated tephras from other sites.

[e]'strata' refers to matching stratigraphic units in the core to equivalent units in other well-dated records.

[f]'tuning' refers to the alignment of proxy data to specific anchor points in the standardized timescales of external records ("wiggle matching").

[g]Diatom silica.

[h]The drill core from the Dead Sea Deep Drilling Project was also tuned to the LR04 benthic stack (Lisiecki and Raymo, 2005) and Soreq Cave (Bar-Matthews et al., 2003).

[i]For the deeper part of the core, lithologic units were tied to the Devils Hole oxygen isotope record (Winograd et al., 1992).

[j]Peaks in calcium carbonate content were tied to the Vostok CO_2 record (Petit et al., 1999).

[k]As a test of the age model, the dust record from Lake Bosumtwi was tied to that of EPICA Dome C (Lambert et al., 2008).

of this correction decreases with the age of the sample: with time, radiogenic ^{230}Th builds up and any initial ^{230}Th decays away, making the proportion of radiogenic ^{230}Th to initial ^{230}Th more favorable. Single-sample dating has been applied at sites where carbonates with high uranium concentrations (>3 ppm) are available and inductively-coupled plasma mass spectrometers allow for smaller amounts of material to be processed, making it easier to avoid detritus when sampling (e.g., Balch et al., 2005; Fritz et al., 2007; see Table 1).

Thus, the presence of initial ^{230}Th in sample materials is non-ideal but surmountable. However, less directly addressed is the issue of possible post-depositional gain or loss of uranium. In addition to clays, other sediment constituents like organic matter and Fe-Mn hydroxides serve as sources of uranium separate from endogenic carbonate; here, uranium is adsorbed to the mineral and solid surfaces of these impurities (Ames et al., 1983a,b,c; Porcelli et al., 1997; Ku et al., 1998; Schmeide et al., 2000; Chappaz et al., 2010; Fig. 1D). In theory, utilizing these other uranium sources for dating can be satisfactory if the uranium was adsorbed at the time of sediment deposition and has since remained immobile, as they are initially without ^{230}Th and would accumulate radiogenic ^{230}Th with time. Indeed, uranium associated with organic matter and clays enclosed in evaporites has been beneficial to the dateability of such low-uranium deposits (e.g., Ku et al., 1998). However, adsorbed uranium is far more susceptible to post-depositional remobilization than uranium bound within the crystal lattice of carbonates (Alam and Cheng, 2014). Furthermore, organic matter, clays, and oxides can also adsorb additional uranium introduced to the materials via fluid flow, for instance when low-oxygen porewaters render uranium insoluble and cause it to accumulate authigenically as metallogenic uranium (Fig. 1D). Unlike in offshore marine settings, in lake sediments, the authigenic accumulation of uranium is a minor to negligible contributor to the total amount of uranium compared to the aforementioned sources (Chappaz et al., 2010; Mikutta et al., 2016; Bone et al., 2017).

Due to the capacity for organic matter to uptake uranium, there have been some attempts to date peats in highly organic-rich sediments that exhibit high uranium concentrations of 1–100 ppm (Van Der Wijk et al., 1986; Rowe et al., 1997; Geyh and Mu, 2005; Frechen et al., 2007), but open system behavior is commonly evidenced by age reversals or anomalous uranium isotope values in these materials. The sediment sequence at Lake Junín is interspersed with thick peat and organic-rich mud layers throughout its length, signaling that the lake has experienced changes in lake level and redox conditions.

2.3. Background on the lake sediments from Lake Junín

Lake Junín (11.0°S, 76.2°W, 4100 m a.s.l.; Fig. 2) was targeted as a site for deep drilling because of its potential to yield the first continuous, absolutely dated sediment record in the tropical Andes that spans multiple glacial-interglacial cycles. Located on the high plateau between the eastern and western cordilleras of the central Peruvian Andes, this relatively shallow (<15 m) lake is the largest water body located entirely within Peru, occupying an area of ∼300 km^2 fringed by marshlands and dense sedge mats (Wright, 1983). Bedrock consists primarily of Paleozoic-Mesozoic marine limestones and dolostones, with some exposure of pre-Cambrian crystalline silicate rocks along the eastern cordillera (Cobbing et al., 1981). The lake owes its origin to >250-ka-aged coalescing glacial outwash fans that dam the northern and southern ends of the lake (Hansen et al., 1984). Moraine mapping and cosmogenic exposure ages from boulders on moraine crests indicate that the lake was not overridden by glaciers or ice at any time in the last 1 million years (Smith et al., 2005a, 2005b), making it one of the few studied lakes in the Andes that predates the Last Glacial Maximum.

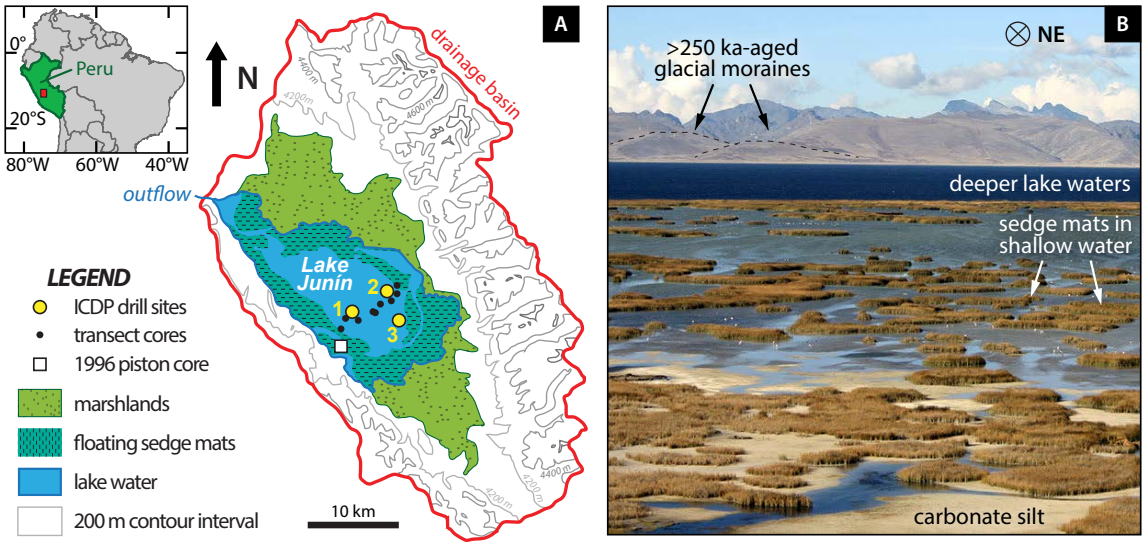

Figure 2: [**A**] Map of Lake Junín and its drainage basin, and the location of the three ICDP drill sites (yellow circles), the nine Livingstone-type piston core locations taken along a transect across the lake (black circles), and the 1996 piston core (white square; Seltzer et al., 2000). The composite splice for Lake Junín is composed of cores from Site 1 and two transect cores from the center of the basin (Hatfield et al., 2020b). [**B**] More recently deposited carbonate silt found among the sedge mats fringing the lake margins. The carbonate silt is subaerially exposed during the dry season (June-July-August) when lake levels drop ∼1–2 m. For scale, small white specks in the shallow water are Chilean flamingos (∼1 m). Photograph by Charles Casey, taken from the western shore facing northeast across the lake.

Previously extracted short (∼20–25 m) cores spanning the last ∼50 kyrs revealed that the lake sediments consist of alternating packages of fine-grained glaciogenic silt and endogenic carbonate silt deposited at a high rate (0.2–1.0 mm yr^{-1}; Hansen et al., 1984; Seltzer et al., 2000). The carbonate silts are interpreted to have formed similar to the way such silts form in present day, in which springs and streams supersaturated in calcite enter the fringing wetlands along the western side of the lake and precipitate carbonate on rooted macrophytes (Fig. 2B; Flusche et al., 2005; Rodbell et al., 2012). Based on the modern carbonate production processes observed, the prediction was that a longer core would contain more carbonate-rich sections, coinciding with warm interglacial and interstadial periods when retreating piedmont glaciers allowed for the formation of marginal wetlands that isolated the basin center from detrital sediment input (Rodbell et al., 2012).

Proving such a temporal link between carbonate deposition, periods of reduced ice cover, and past warm intervals in a longer core would rest on the reliability of the age-depth model. Thus, we conducted a pilot study on the 1996 piston core from the shallow western margin of the lake extracted by Seltzer et al. (2000) to determine if U-Th dating could be applied to bulk samples of the carbonate silts (Fig. 2A). The results from this initial test were encouraging: most of the U-Th analyses attempted on carbonates from the upper 10 m of the core were consistent with the chronology produced by ^{14}C ages on molluscs and organic macrofossils (Fig. 3A). The preliminary results also revealed that Lake Junín carbonates have high uranium concentrations (0.3–2 ppm) and low detrital content, with ratios of radiogenic ^{230}Th to initial ^{230}Th that are 10 times greater than sediments from Lake Titicaca (Fritz et al., 2007) and the Great Salt Lake (Balch et al., 2005).

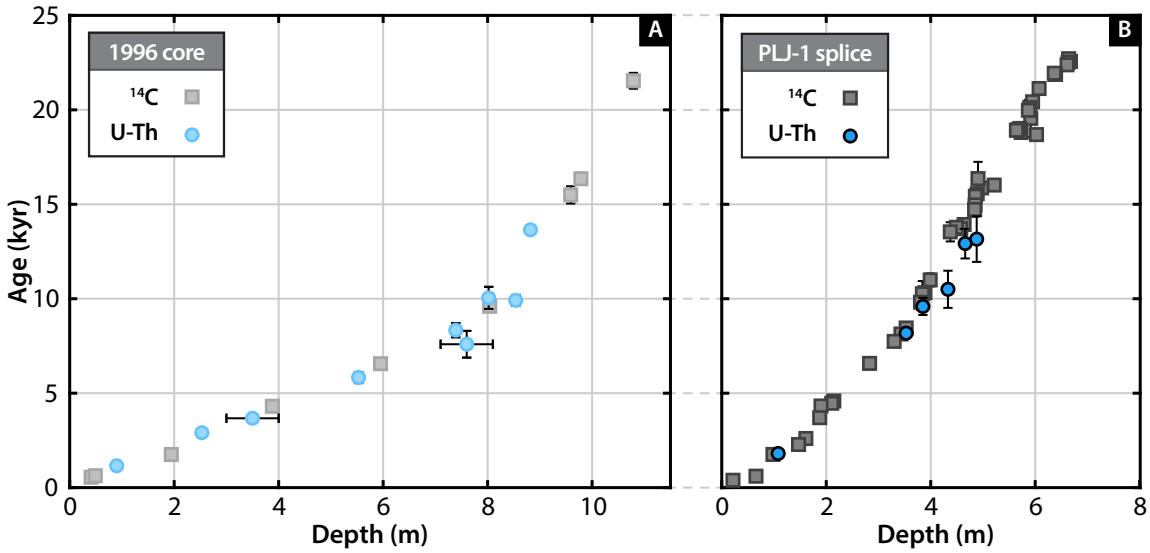

Figure 3: Comparison of radiocarbon (gray squares) and U-Th (blue circles) dates from the 1996 core [**A**] and the PLJ-1 splice [**B**]. Radiocarbon data are from Seltzer et al. (2000) for the 1996 core and Woods et al. (2019) for the PLJ-1 splice. Note that most U-Th data shown represent a weighted mean of multiple analyses (see Tables A1–A3). Vertical error bars represent 2-σ ranges; horizontal error bars, if shown, indicate uncertainties in the depth location of samples. Based on the PLJ-1 data, the inferred sedimentation rate (not normalized by dry bulk density) at the lake depocenter over the last 25 kyrs is ∼0.3 m kyr^{-1}, which is ∼50–60% slower than that of the 1996 core located on the western lake margin (Fig. 2).

Following project approval, the uppermost ∼100 m of sediment was drilled and cored in eleven holes across three sites in August 2015. This paper focuses only on sediments recovered from Site 1, the deepest core extracted from the approximate depocenter of the lake. We work primarily from the PLJ-1 splice, which is generated by stratigraphic correlation and comparison of physical property data of core sections from four of the five holes at Site 1 and core sections from two piston transect cores close to the lake depocenter (Fig. 2). More specifics regarding the coring operation and the subsequent generation of the PLJ-1 splice are described in Hatfield et al. (2020b); hereafter, all references to depth in the Lake Junín core refer to the core composite depth below lake floor (CCLF). For complete information on the radiocarbon dates constraining the first ∼50 kyrs of the record, we refer the reader to Woods et al. (2019).

Here we briefly describe the stratigraphy of the PLJ-1 splice; a full description will be detailed in subsequent publications elsewhere. Broadly, the prediction that a long core from Lake Junín would also contain alternating packages of carbonate and glaciogenic sediment was correct: ∼10 m thick packages of cream-colored carbonate silt alternate with ∼10–15 m thick intervals of dark gray, fine-grained carbonate-rich glaciogenic silt throughout the length of the core until ∼85 m, where a thick package of carbonate-rich sand occurs (Fig. 4A). The mean grain size of this bed was incompatible with the drilling tools during core extraction, preventing deeper core recovery. Peat and organic-rich mud layers of ∼1- to 50-cm thickness punctuate both the carbonate and glaciogenic silt intervals and contain abundant microfossils that suggest that the peats represent times of wetland encroachment towards the lake center during lake level lowstands (Woods et al., 2019). Despite this interpretation, there is no stratigraphic evidence of any depositional hiatus

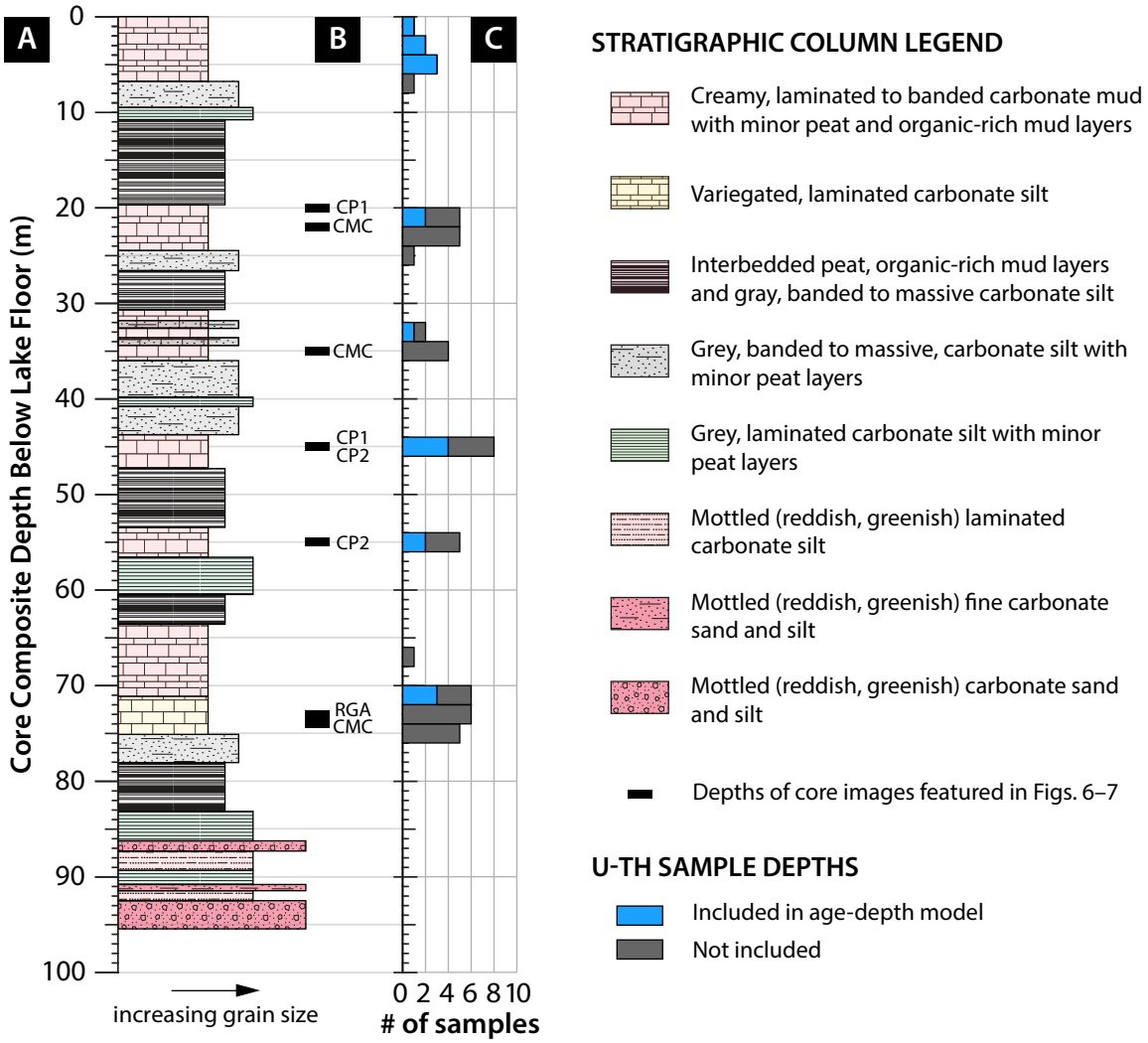

Figure 4: [**A**] Stratigraphic column of the PLJ-1 splice, described following the core description scheme proposed by Schnurrenberger et al. (2003). Lithologies in the stratigraphic column legend are listed in ascending order of mean grain size (smaller at the top, larger at the bottom). [**B**] Rectangular bars mark the depths of the cores featured in Figs. 6 and 7 and are labeled by facies (see Section 3.1). [**C**] Stacked histogram of depths of samples collected for U-Th dating, in which blue represents samples that yielded dates included in the age-depth model and gray represents samples that yielded dates that were not included.

or unconformity throughout the core, suggesting that the drill site has been submerged, however shallow in depth, for the duration of the record (Rodbell, Abbott, et al., in prep.).

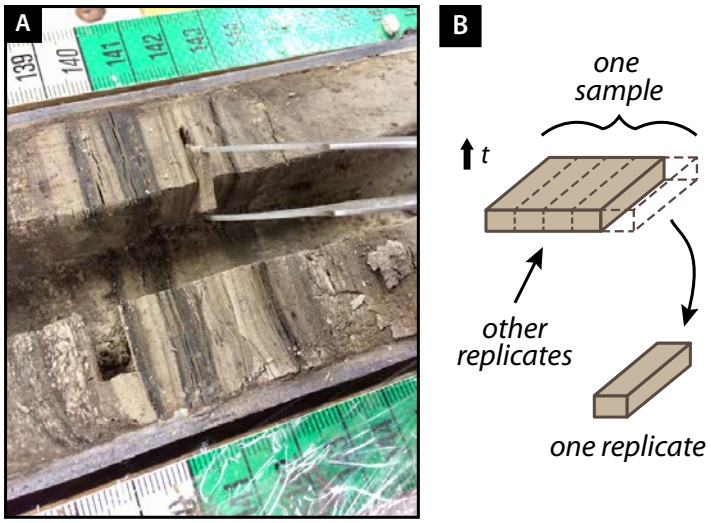

Figure 5: [**A**] The core sampling process for U-Th dating. Surgical straight edges and blades from a fruit carving knife set were used to cut out thin (∼0.2–0.3 cm) wafers of sediment, which then were extracted with tweezers. [**B**] One *sample* consists of a single wafer of sediment extracted as shown in Panel A. Replicate analyses are made on separate sections of the sediment wafer.

3. Methods

3.1. Core sampling for U-Th dating

Within the U-Th geochronology community, there is a common expectation that samples with the following characteristics, regardless of substrate type (speleothems, sediments, tufas, *et cetera*), have greater potential for success: light in color (considered an indicator of sample purity), non-porous, homogeneous (either as thin laminae or thicker intervals), and free of shell fragments and other detritus. We took advantage of the opportunity provided by modern mass spectrometry to process smaller amounts of material (∼10–70 mg) in an effort to isolate small, relatively low-detritus domains of sediment.

Cores were visually assessed for material that fulfilled the criteria described above. Once a carbonate interval was identified, we used utility blades, knives from a fruit and vegetable carving set, and tweezers to cut and extract thin wafers of sediment ∼0.2–0.5 cm in thickness (Fig. 5). In sections of core containing finely laminated carbonate sequences, we took care to isolate individual laminae, only sampling the cleanest parts and scraping away undesirable material when necessary. In addition, when possible, we sampled layers that appeared to have more detritus immediately adjacent to these cleaner laminae with the intention of using this material for building isochrons. We examined sample smear slides in order to verify petrographically that samples identified by eye as being relatively detritus-free were so, and made real-time adjustments in sampling strategy based on results. Fig. 4C shows the depths from which U-Th samples were taken and their relation to stratigraphic units. Sedimentary lithologies were defined following protocols by Schnurrenberger et al. (2003), including smear slide observations.

During sampling, we also documented the macro-scale sedimentological characteristics associated with each sample. After observing a variety of carbonate-rich sequences, we divided them into

four lithological facies categories:

- **C**ream-colored **m**assive **c**arbonates (**CMC**): cream-colored, massive, medium to thick (∼10–50 cm) bedded carbonate silts found in close association with gray, massive, banded or mottled silt, with some thin (∼1–2 cm thick) peat or organic-rich mud layers (Fig. 6)
- **R**ed-**g**reen **a**lternating (**RGA**): red and green laminated sets of carbonate silts that alternate in color every ∼5–20 cm, with some organic-rich peat laminae (Fig. 6)
- **C**ream-colored carbonates with **p**eat beds (**CP1**, **CP2**): Cream-colored, faintly banded carbonate silt interbedded with peat layers, with some associated with thick (∼30–50 cm) overlying peat beds that were laterally continuous across multiple holes at Site 1 (CP1), and others associated with thin (∼3–5 cm), laterally discontinuous peat beds (CP2) (Fig. 7)

Each sample extracted for U-Th dating was subsequently categorized into one of these four facies. At times, we will refer to specific samples by their sample ID, which consists of an alphabetical letter A–P followed by a number 1–6.

3.2. Sample preparation and chemistry for U-Th dating

After core sampling, sediment wafers were frozen and then placed in a vacuum freeze drier to remove moisture from all material. Most samples retained their original wafer shape after this process. A small portion of each sample was then disaggregated for micro-scale sedimentological characterization under a picking microscope. We made qualitative observations of the following: color; hardness of bulk sediment (friable or compacted); and the relative abundance of mollusc shell fragments, ostracode valves, organic fibers (peat fragments, grasses, seed pods), sponge spicules, siliciclastic grains, or other mineral precipitates. For subsequent U-Th analyses, we manually removed mollusc shell pieces from the sample before dissolution, or avoided processing samples containing abundant mollusc shell fragments that could not be reliably removed. Except for one case in which we processed both the sediment sample and removed mollusc shell fragments separately as two unique analyses (F14), all analyses discussed are measurements on bulk samples containing all other aforementioned constituents (total sample dissolution).

Because U-Th column elutions are time and resource intensive, a small set of samples from different facies were screened for their uranium and thorium concentrations to determine which facies would most likely yield material viable for dating. Powders of ∼2 mg were dissolved in dilute HNO_3, and analyses of uranium and thorium concentration were performed on a VG PQ2+ quadrupole ICP-MS and an Agilent 7900 ICP-MS at MIT. Samples with higher U/Th ratios were then identified as materials worth further processing as they are more likely to yield "clean" samples with high $^{230}Th/^{232}Th$ ratios (Section 2.2).

Replicate analyses were then processed through U-Th column elusions in sample sets of 5 to 15 from February 2016 to July 2019. When possible, we analyzed at least three replicates from each sample horizon. Here, we purposefully apportion different aliquots of the original sediment wafer for each replicate analyses in order to test the reproducibility of dates from stratigraphically coherent material (Fig. 5B). This step is an important distinction from repeated analyses of a homogenized powder, which would only provide a measure of internal lab errors or the quality of sample homogenization. Our original intention in processing samples this way was not only to test for reproducibility, but also to build isochrons, for which it is necessary to analyze subsamples that span a range of detrital contamination levels.

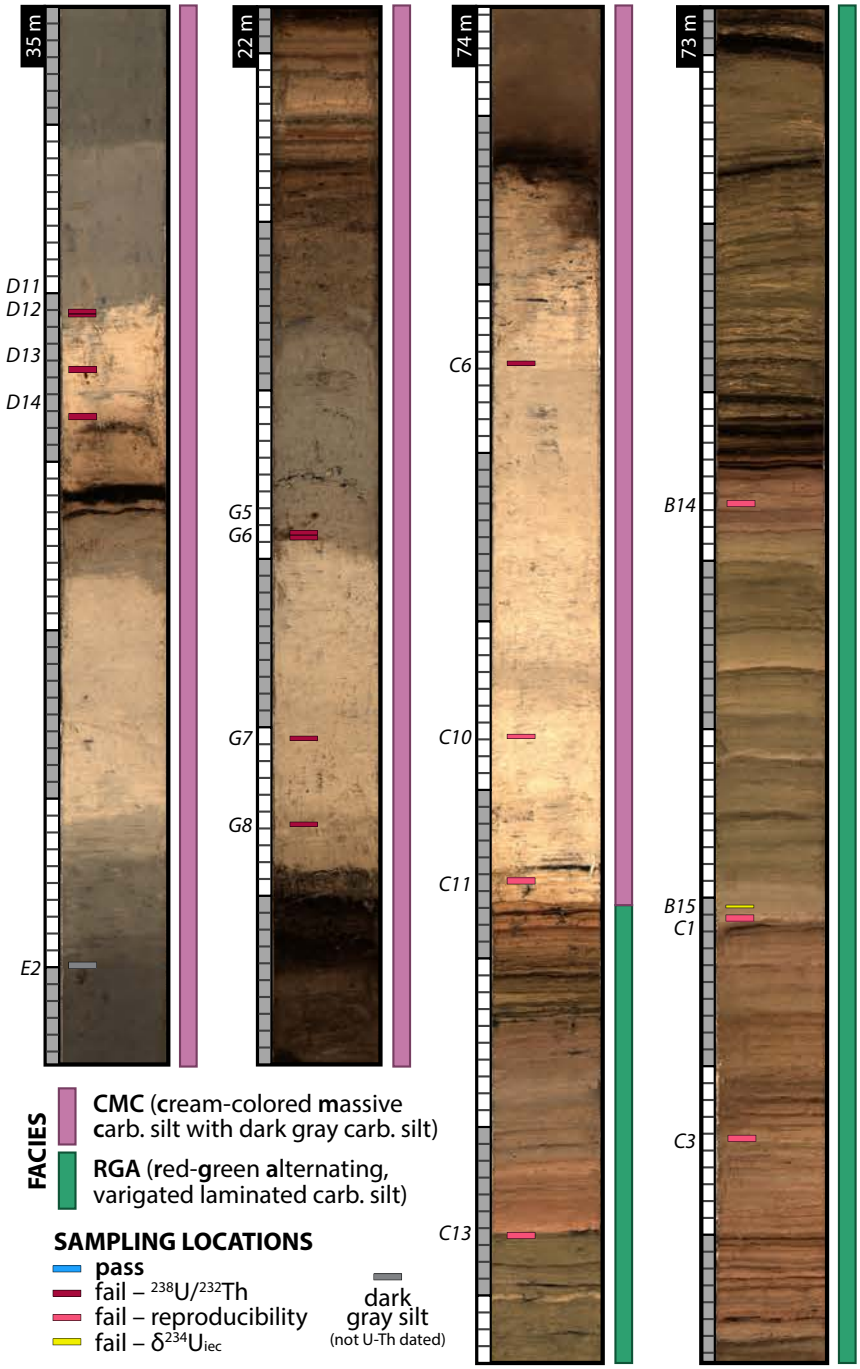

Figure 6: Core scanning images and U-Th sample locations of four selected cores that feature the CMC and RGA facies. The approximate corresponding CCLF is noted in the black rectangular box at the top left of each core image. The column of gray and white boxes appended to the left of each core image is a ruler representing alternating blocks of ten centimeters, mimicking the actual ruler used during scanning at LacCore's facilities. Small rectangles plotted on top of the core image represent sample locations and are labeled by sample ID and color-coded by threshold criteria result (see Section 5 and Fig. 8). The columns to the right of each core image represent the facies that is given to a sample collected in that depth interval; for example, for the third core image, samples C6, C10, and C11 are categorized as CMC, while C13 is categorized as RGA. Core scanning images were made using a Geotek MSCL-CIS at the National Lacustrine Core Facility (LacCore).

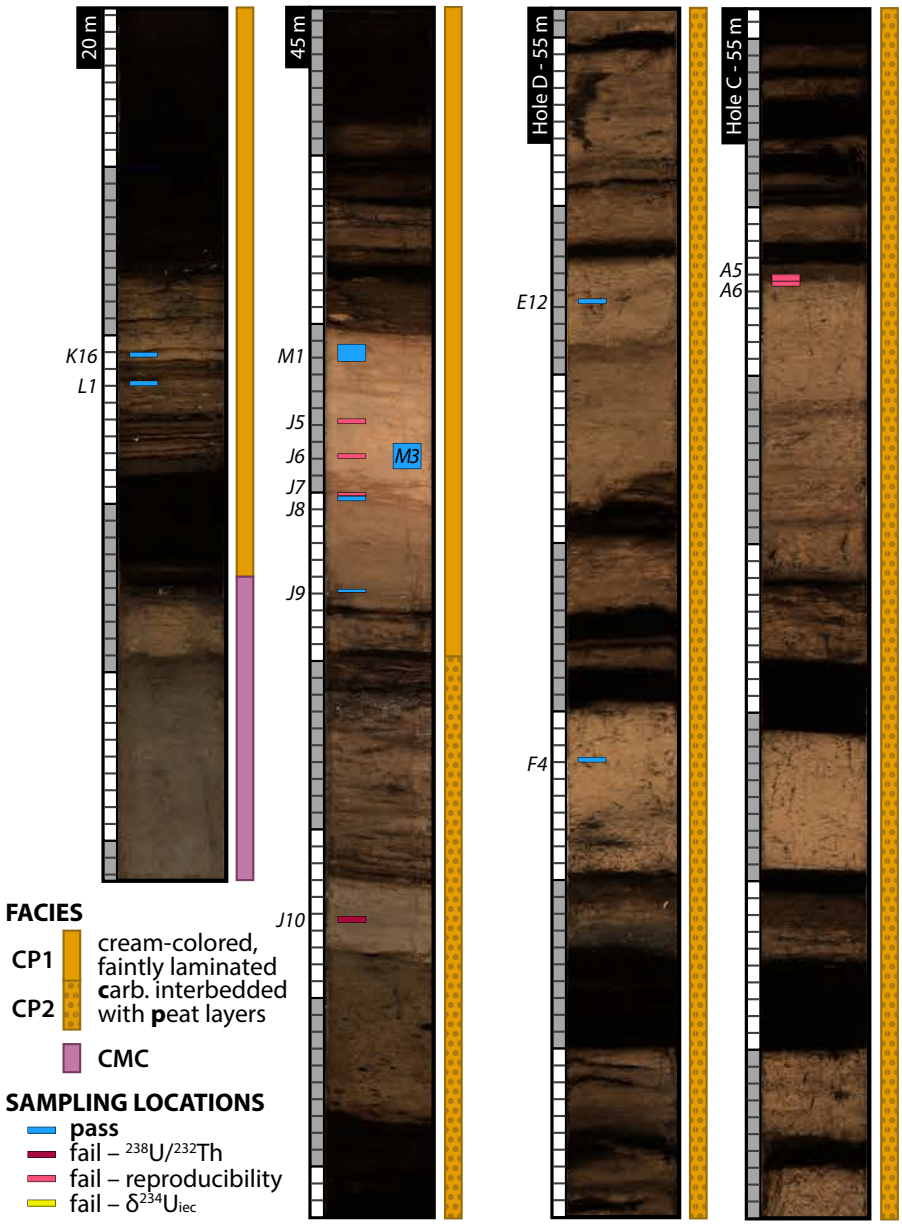

Figure 7: Core scanning images and U-Th sample locations of four cores that feature the CP facies, which is subdivided into CP1 and CP2 to differentiate between samples that are associated with thick (>10 cm) peat layers that are laterally continuous across cores from multiple holes (CP1) and those that are not (CP2). Note that the third and fourth images are of cores from the same exact depth but from different holes at Site 1, shown here to demonstrate the lateral discontinuity of some peat and carbonate beds. Holes at Site 1 were spaced approximately ∼20 m apart. Small rectangles plotted on top of the core image represent sample locations and are labeled by sample ID and color-coded by threshold criteria result (see Section 5 and Fig. 8). See caption in Fig. 6 for explanation of other symbology used in the figure.

After sample selection and preparation, sample dissolution was performed in a clean laboratory at MIT. Samples of 5–60 mg were dissolved in HNO_3 and spiked with a ^{229}Th-^{233}U-^{236}U tracer in clean Teflon beakers. Next, following methods described by Edwards et al. (1987) and Shen et al. (2002), uranium and thorium were co-precipitated with ∼4–8 mg of Fe oxyhydroxides and then separated using BioRad AG1-X8 anion exchange resin (100–200 mesh, 0.5 mL column volume). The isotopic compositions of the resulting uranium and thorium fractions were then measured on a Nu Plasma II-ES multi-collector ICP-MS at MIT. We introduced sample solutions through a CETAC Aridus II desolvating nebulizer system coupled to a PFA nebulizer with a 100 µL/min uptake capillary. To monitor mass bias and variable SEM yield, each uranium sample analysis was bracketed by a 12.5 ng/g solution of the CRM-112a standard (New Brunswick Laboratories), and each thorium sample analysis was bracketed by an in-house ^{229}Th-^{230}Th-^{232}Th standard. See Section S1 for further details on U-Th measurements, as well as information on U-Th dating of materials from the 1996 core, which occurred around 1999 and 2011 at the University of Minnesota-Twin Cities.

3.3. Estimating the initial ^{230}Th correction

As discussed in Section 4, the correction for initial ^{230}Th has a greater impact on impure sample materials, so we must carefully consider this correction for the lake sediments at Lake Junín. Ten samples processed from the 1996 core yielded indeterminate ('infinite') dates, in which a unique solution to the ^{230}Th age equation could not be found after iteration. These samples all had ^{232}Th concentrations that were 20–200 times greater than other samples from the 1996 core that yielded calculable dates (2–7 ppm, compared to 0.04–0.1 ppm), forming a statistically distinct population. Similarly, these samples also had ^{238}U/^{232}Th ratios that were ∼50 times lower than that of other samples (0.3–0.6 ppm). These results suggest that the samples yielding indeterminate ages had high amounts of detrital contamination that contributed a significant amount of initial ^{230}Th at secular equilibrium with ^{238}U, thereby causing apparent infinite dates.

Assuming that the detrital component of the indeterminate samples of the 1996 core is representative of the isotopic composition of detrital end member material found in all sediments of the PLJ-1 splice, we calculated the average ^{230}Th/^{232}Th ratio of the indeterminate samples and used this ratio for the initial ^{230}Th correction in our calculations. This way of estimating the true ^{230}Th/^{232}Th ratio is not perfect because it counts radiogenic ^{230}Th accumulated in these samples as detrital, but the depths of these samples suggest that their true age is no older than 30 kyrs and thus we do not expect an appreciable proportion of the ^{230}Th to be radiogenic.

The average ^{230}Th/^{232}Th atomic ratio of the indeterminate samples from the 1996 core is 7.9 ± 0.9 ppm (Fig. S1). Our starting assumption is that this ratio is invariant through time, but it is entirely possible—if not expected—that the isotopic composition of detritus is variable due to changes in clastic transport or source regions. To account for these unknowns and other unknown unknowns, we apply an uncertainty of 50% to this average and use an initial ^{230}Th/^{232}Th atomic ratio of 8.0 ± 4.0 ppm for U-Th data from the PLJ-1 splice. This value is higher than the average ^{230}Th/^{232}Th ratios for the continental crust and bulk silicate Earth, 3.2–4.5 ppm (based on estimates of ^{232}Th/^{238}U for these domains by Wipperfurth et al., 2018). Such values can occur in alkaline lakes due to dissolved ^{230}Th in the water column (hydrogenous Th; e.g., Lin et al., 1996) and in carbonate-dominated systems due to high ^{238}U/^{232}Th ratios in limestone (e.g., Carolin et al., 2013).

3.4. Calculating weighted means and uncertainties of samples with replicate analyses

As mentioned in Section 3.2, we attempted to analyze at least 3–5 replicates for each sample as a test of the reproducibility of unequivocally coeval material. We calculate a date for each individual replicate analysis using Eq. 1 and the initial $^{230}Th/^{232}Th$ ratio stated above. We then use these dates to calculate an error-weighted mean ($\bar{x}$) and uncertainty ($\sigma_{\bar{x}}$) of all replicate analyses in a sample, in which weights are equal to the inverse of the variance of each date:

$$\bar{x} = \frac{\sum^{N} \frac{x_i}{\sigma_i^2}}{\sum^{N} \frac{1}{\sigma_i^2}}, \quad \sigma_{\bar{x}} = \sqrt{\frac{1}{\sum^{N} \frac{1}{\sigma_i^2}}} \tag{4}$$

where N is the number of replicate analyses in the sample; x_i is the individual date of each replicate; and σ_i^2 is the variance of the individual dates of each replicate.

We then determine the degree of agreement between replicate analyses to estimate an uncertainty that is appropriate for the observed scatter between dates. Here we calculate the Mean Square of Weighted Deviates (MSWD), a measure of the ratio of the observed scatter around the mean to the expected degree of scatter given the analytical uncertainties of each data point (McIntyre et al., 1966; Wendt and Carl, 1991). The value is essentially the chi-squared statistic (goodness of fit) divided by the number of degrees of freedom (f=N−1), or the "reduced" chi-squared:

$$\text{MSWD} = \frac{1}{f} \sum^{N} \frac{(x_i - \bar{x})^2}{\sigma_i^2}. \tag{5}$$

The value of the MSWD tells us if the calculated uncertainties for each date are over- or under-estimated based on the observed scatter in data. A value of ∼1 indicates that the observed scatter is equal to the predicted scatter; values less than 1 indicate that the observed scatter is less than is predicted by the uncertainties; and values greater than 1 indicate that the observed scatter is more than the predicted scatter. Samples with an MSWD much greater than 1 are considered to have excess "geologic scatter," suggesting possible biases in the calculated dates, perhaps due to a violation of the assumptions underpinning the system (e.g., open system behavior).

Thus, for any sample with an MSWD > 1, we expand the uncertainties of the replicate analyses by a factor of $\sqrt{\text{MSWD}}$ and then recalculate the weighted means with these larger uncertainties using Eq. 4 (Ludwig, 2003). The `IsoplotR` program by Vermeesch (2018) also includes this strategy as one option of treating data with excess geologic scatter (referred to as "overdispersion"). While the presence of excess scatter is non-ideal and raises concerns about the validity and practical use of such dates, the data still represent geologically meaningful information and should not be rejected outright without further consideration (and we will do much considering, starting in Section 5).

Using the MSWD as a black-and-white parameter to evaluate the validity of dates is discouraged, since the highest permissible MSWD is dependent on N (Wendt and Carl, 1991) and sometimes subject to interpretation (Powell et al., 2002; Ludwig, 2003). Thus, we calculate the probability of the observed scatter occurring given the uncertainties for each replicate analysis—a "probability of fit" index—by computing the chi-square cumulative distribution for MSWD×f (the chi-squared statistic) about f degrees of freedom (York, 1968). The probability of fit is the probability that the uncertainties assigned to each replicate will produce at least the amount of scatter observed by the replicates; thus, samples with high probabilities of fit are considered reproducible whereas

those with lower probabilities of fit are considered less so.

Some samples only have 1–2 replicates; these were cases in which early replicate analyses yielded unfavorable results (e.g., low $^{238}U/^{232}Th$ ratios) and were not repeated in the interest of time and resources. For the remainder of this paper, our discussion of U-Th dates will refer to the weighted means and uncertainties (MSWD-adjusted) of samples rather than the individual dates of replicate analyses, unless otherwise noted.

3.5. Other corresponding data

We use other sedimentological, geochemical, paleoecological, and physical data to interpret and understand our U-Th data. We provide a list of these datasets in Table 2 and their intended use. More information regarding these methods of measurement can be found in the Supplementary Materials (Section S2) and other publications currently being prepared elsewhere.

Dataset	**Brief Methods**	**Purpose**
Elemental concentrations	ICP-MS	Determine if there are relationships between U-Th data and concentrations of Ca and trace elements Mg, Sr, Al, Ti, P, V, Mn, and Fe. Measurements are made on the same sample material used for U-Th dating.
Total inorganic and organic carbon	coulometry, at approx. 1 cm resolution for non-glaciogenic intervals	Determine if there is a relationship between U-Th data and carbon content. Only measurements made within 1 cm of the U-Th sample are paired with U-Th data.
Color reflectance	spectrophotometry on automated core logger at 5 mm resolution	Determine if there is a relationship between U-Th data and any spectral reflectance wavelength band. Data is paired with a U-Th sample only if there is a measurement made within 2.5 mm of the sample.
Mineralogy	X-ray diffraction	Determine the mineral composition of the carbonate phases, and if there are discernible differences between endogenic and detrital carbonate.
Ostracode assemblages	picking and identification following Pérez et al. (2010) and Karanovic (2012)	Determine if there exists a relationship between U-Th data and ostracode color, taphonomy (number of broken vs. intact valves; adults vs. juveniles), or ecology (benthic vs. swimmer species, ornamentation).

Table 2: Other datasets used in this study for comparison with U-Th data.

4. Results

In total, we generated 174 U-Th dates from 55 bulk samples from the PLJ-1 splice. Uranium and thorium geochemical data as well as the number of replicates produced for each sample (N = 3–8) can be found in Table A3. Samples originate from each of the five high (>70%) $CaCO_3$ intervals that occurred every ∼10–15 m in the core (Fig. 4C). All U-Th dates from the uppermost 5 m are broadly consistent with radiocarbon dates from terrestrial macrofossils and charcoal in the same depth interval (Fig. 3B; Woods et al., 2019), suggesting that our correction for initial ^{230}Th

is appropriate. In addition, a sample from ∼6.5 m (P10, Table A3) yielded an indeterminate date and had a $^{230}Th/^{232}Th$ atomic ratio of 7.7 ± 0.2 ppm, consistent with our estimate of the detrital $^{230}Th/^{232}Th$ ratio applied in corrections. Sample ^{238}U concentrations are variable and are generally 0.2–4.0 ppm (mean = 1.5 ± 1.2 ppm, 1-σ); ^{232}Th concentrations are also variable, ranging 0.02–2.4 ppm (mean = 0.6 ± 0.5 ppm, 1-σ).

For the deepest part of the core, the oldest U-Th dates suggest that the record is no older than ∼800 ka. This observation is consistent with the absence of evidence of the Brunhes-Matuyama magnetic reversal (aged ∼780 ka) in the paleomagnetic secular variation record (Hatfield et al., 2020a). However, the scatter of dates throughout the entirety of the core is, at first glance, alarming: at ∼20–25 m, the first high-$CaCO_3$ section beyond the interval covered by radiocarbon, U-Th dates already span a range of ∼200 kyrs (Fig. 8). The spread of dates increases with depth, reaching ∼300 kyrs at the bottom of the record. As is, the scatter of data is too great to build any practical age-depth model, even after applying outlier analysis. Furthermore, all attempts to reduce scatter by building isochrons from replicate analyses and adjacent dirty-clean sample pairs failed (high MSWD and low probability of fit; Section S4 and Fig. S3).

Here, we arrive at the main crux of this paper. The scatter of data and the failure to build isochrons is clear evidence that at least some of the dated materials have not remained closed systems or do not otherwise satisfy the operating assumptions of U-Th dating. Despite this noise, is there a way to objectively assess the quality of each U-Th date, and subsequently curate the dataset without biases (i.e., avoid "cherry-picking")? In the following sections, we detail our approach to this question.

5. Curation of U-Th data using threshold criteria

Noisy U-Th geochronological datasets are nothing new; in attempts to find clarity in uncertain data, a common practice is to apply some screening criteria based on uranium and thorium concentrations. For example, some studies dating corals and carbonate slope sediments have rejected dates that exceed a certain thorium concentration or do not meet a minimum uranium concentration because such dates tend to have larger corrections and errors (Robinson et al., 2002; Henderson et al., 2006; Skrivanek et al., 2018). However, picking the values for these thresholds can be subjective, especially if there is no clear separation between distinct populations within the data.

As a start towards better understanding the scatter in our data, we consider applying similar thresholds, first by examining the $^{238}U/^{232}Th$ ratio and the probability of fit of all dates for a given sample to a single weighted mean (Fig. 8A and B). $^{238}U/^{232}Th$ ratios ranged between <1 and 30 and probabilities of fit essentially spanned the full domain of possible values, from 0% to 99%. Between 20 and 60 m, we notice that the samples with the oldest dates all have $^{238}U/^{232}Th$ ratios that are <1, including those yielding indeterminate dates (Fig. 8A). One possible explanation for this observation is that these samples have initial ^{230}Th that has not been accounted for with our initial correction, which would bias dates to be older than the true age. The effect of this bias would be greatest in samples with low radiogenic ^{230}Th due to low uranium concentrations. (Note that we later discuss another explanation for these data in Section 7.)

Regarding the probability of fit, deciding how low of a probability is acceptable is somewhat arbitrary; there is no broad consensus within the geochronology community on how best to treat such data, especially in circumstances in which the total number of subsamples is low (Ludwig, 2012), as is our case. However, we think that most geochronologists would agree that samples with a probability of fit less than 1% (especially those much closer to 0%) exhibit an amount of excess

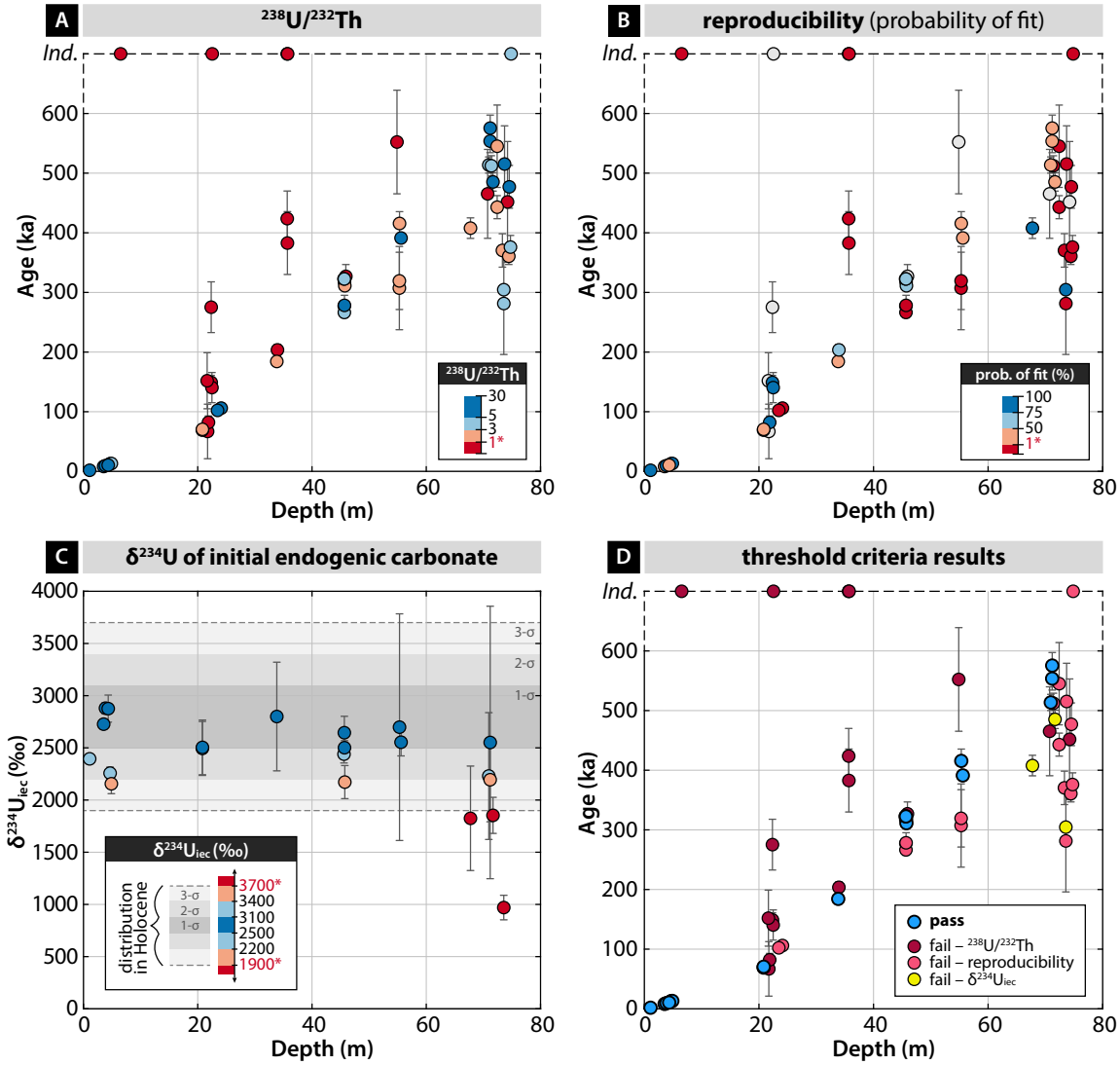

Figure 8: Step-by-step application of thresholding criteria: [**A**] $^{238}U/^{232}Th$, [**B**] reproducibility, and [**C**] $\delta^{234}U$ of initial endogenic carbonate ($\delta^{234}U_{iec}$). [**D**] shows the data that pass and fail the three aforementioned criteria. Note that each point represents the weighted mean and standard deviation of multiple replicate analyses (see Table A3). In Panels A–C, blue/red colors represent values that are more/less ideal for U-Th dating. Values of thresholds are indicated by a red asterisk (*) in each legend. Samples that do not satisfy criteria and were thus subsequently eliminated are colored in dark red. Samples plotted along the uppermost dashed line labeled 'Ind.' refer to analyses that yielded incalculable U-Th dates or were infinite (indeterminate). In Panel B, analyses plotted in light gray are those with only one replicate analysis. Panel C only includes data that pass the $^{238}U/^{232}Th$ and reproducibility thresholds. Shaded gray areas represent the distribution of $\delta^{234}U_{iec}$ values observed in the Holocene, including data from the 1996 core. For Panel D, note that some samples failed both criteria for $^{238}U/^{232}Th$ and reproducibility; in these instances, the samples were categorized as having failed the $^{238}U/^{232}Th$ criteria. All error bars in each panel are 2-σ range.

scatter that is beyond recovery of practical information about the true age of the sample.

Thus, in the interest of not using too strong of a hand in curating the U-Th data to begin, we apply two conservative threshold criteria: the $^{238}U/^{232}Th$ ratio must be >1 and the probability of fit >1% (Fig. 8A and B). Of the 55 samples, 17 fail the $^{238}U/^{232}Th$ criterion and 22 fail the reproducibility criterion. Of the 17 samples that fail the $^{238}U/^{232}Th$ criterion, eight had more than one replicate analysis, and of those eight, five also fail the reproducibility criterion (Table A3). In Fig. 8D, we show which criterion each sample fails; for the purposes of simplifying ensuing explorations into the dataset, the five samples that fail both aforementioned criterion are categorized as having failed the $^{238}U/^{232}Th$ criterion.

Next, we consider another screening approach adopted for U-Th dating of marine samples that involves $\delta^{234}U_{initial}$. Because the residence time of uranium in the ocean is very long (∼400 kyrs; Ku et al., 1977), the $\delta^{234}U$ of seawater is thought to have remained relatively constant for at least the last 400 kyrs (Henderson, 2002; Henderson and Anderson, 2003). Thus, assuming that marine samples reliably preserve the $\delta^{234}U$ values of the waters in which they formed, dates from marine samples with $\delta^{234}U$ values that deviate significantly from modern values are considered potentially inaccurate due to diagenesis (Bard et al., 1991; Hamelin et al., 1991; Gallup et al., 1994). In contrast, the $\delta^{234}U$ of surface waters is very diverse and is sensitive to basin lithology, basin-specific weathering mechanics, riverine and groundwater inputs, and climate (e.g., Sarin et al., 1990; Kronfeld and Vogel, 1991; Plater et al., 1992; Kronfeld et al., 2004; Robinson et al., 2004; Durand et al., 2005; Grzymko et al., 2007; Chabaux et al., 2008). Although few studies examine the long-term history of internal $\delta^{234}U$ variability in lakes and other surface waters (e.g., Kiro et al., 2018), the range of internal $\delta^{234}U$ variability observed in the aforementioned river and groundwater studies suggests that the internal $\delta^{234}U$ of lake waters should not vary significantly without dramatic changes in drainage basin organization. Since the lithology of a lake basin is invariant over the timescales relevant to this study, variability in $\delta^{234}U$ is driven by changes in hydrology. McGee et al. (2012) documented $\delta^{234}U$ values spanning a 200‰ range in lacustrine cave carbonates during the last deglaciation in Lake Bonneville (Utah, USA), an area that experienced a ∼2× change in precipitation.

Thus, we apply a third threshold criterion using the $\delta^{234}U$ of the initial endogenic carbonate ($\delta^{234}U_{iec}$) of each sample, which we calculate by correcting $\delta^{234}U_{initial}$ values for detrital uranium (see Section S3 for relevant equations). The average $\delta^{234}U_{iec}$ of all samples that yield dates verified by radiocarbon data (including data from the 1996 core) is 2800 ± 300‰ (1-σ). If we compare this average to the $\delta^{234}U_{iec}$ values of the remaining 21 samples, we observe that three samples at ∼70–75 m have values that fall well below the average, even outside the range defined by three standard deviations from the mean (Fig. 8C). Because the magnitude of these differences is large, we suggest that these values are unlikely to reflect real changes in the $\delta^{234}U$ of the lake waters, and thus suspect the validity of these dates. Therefore, we mark these three samples as having failed the $\delta^{234}U_{iec}$ criterion (Fig. 8D).

While the remaining 18 dates form a visually pleasing line (Fig. 8D), this observation alone does not prove that these remaining dates are accurate. However, the samples generally abide by the rules of stratigraphic order, which is behavior consistent with closed-system dates. Furthermore, the results of applying the threshold criteria may follow our theoretical expectations for normally distributed scatter about the mean. That is to say: if you were to ask someone to draw a line through the middle of the original scatter of points, the 18 samples that remain would not stray far from it.

6. Understanding the scatter

Having classified the U-Th data into categories that describe the main flaw of each nominally failed sample (Fig. 8D), we now explore the underlying causes for poor sample behavior and determine if the application of threshold criteria is justified. Essentially, we ask: Is there other evidence that supports our assertion that the threshold criteria failing samples have not remained closed systems? What is special about the 18 passing samples such that they exhibit fewer symptoms of open system behavior?

To answer these questions, we compare the U-Th data to all the datasets listed in Table 2 to assess the two most obvious causes for the scatter: detrital contamination and post-depositional uranium remobilization. This comparison suggests that redox-related processes have played a large role in dictating the behavior of the U-Th system, which is most clearly demonstrated by contrasting data from the CMC and CP facies.

6.1. Detrital contamination

The first and most obvious hypothesis for poorly behaving dates is detrital contamination that is unaccounted for with the initial $^{230}Th/^{232}Th$ correction. As stated in Section 2.2, impure sample substrates have been the main obstacle in previous U-Th dating efforts in lake sediments, and there is no evidence to suggest that Lake Junín would be an exception. If detrital contamination does indeed play a large role in the scatter of our U-Th data, we can make certain predictions for how other sedimentological and geochemical data would respond. For example, we would expect that samples with lower $CaCO_3$ content would comprise the eliminated dates, especially those that failed the $^{238}U/^{232}Th$ criterion. We are able to test this hypothesis directly using co-located measurements of $CaCO_3$ content (weight %) as well as optical lightness from color reflectance spectra (Table 2 and Section S2). Optical lightness, defined here as the sum of spectra in the visible band of the electromagnetic spectrum (400–700 nm), has been shown to be a reasonable proxy for carbonate content in marine sediments (e.g., Nagao and Nakashima, 1992; Mix et al., 1995; Balsam et al., 1999). Data for the PLJ-1 splice also shows that $CaCO_3$ content >50% appears to scale with optical lightness (see gray circles in Fig. 9A). Because color reflectance data were measured on a finer and more regular sampling interval than carbon data, there are more optical lightness data that correspond to U-Th samples than $CaCO_3$ content measurements ($N = 46$ versus 29; Fig. 9).

From Fig. 9, we notice that all but one of our U-Th samples have >50% $CaCO_3$ content, with most passing dates having >70% $CaCO_3$ content. However, there are data that failed threshold criteria occupying the same range in $CaCO_3$ content as passing data. Contrary to expectations, the five samples with the highest $CaCO_3$ content failed the threshold criteria (Fig. 9B). Likewise, the five samples with the highest optical lightness also failed (not all are the same five samples; Fig. 9C). Sample C10 is the most extreme case in this comparison, and as a visual check, we can see its sampling location in Fig. 6 and verify its optical lightness value relative to other samples. Again, there is no clear pattern between passing and failing U-Th dates and optical lightness; samples appear to exhibit the entire range of optical lightness values observed in the core (empty gray circles, Fig. 9A). One could argue that the samples failing the $^{238}U/^{232}Th$ criterion tend to have higher optical lightness values compared to passing samples, behaving opposite to our predictions (Fig. 9C). The results are similar when we compare our data with grayscale or luminance (also known as L^*), another "lightness" parameter using the CIE L*a*b* color description system.

Based on these results, we speculate that a high proportion of bedrock carbonate in the detrital component could explain the high $CaCO_3$ content of failed samples; even the darkest gray silt sections in the core with high magnetic susceptibility had 20–50% $CaCO_3$ content. The uranium from

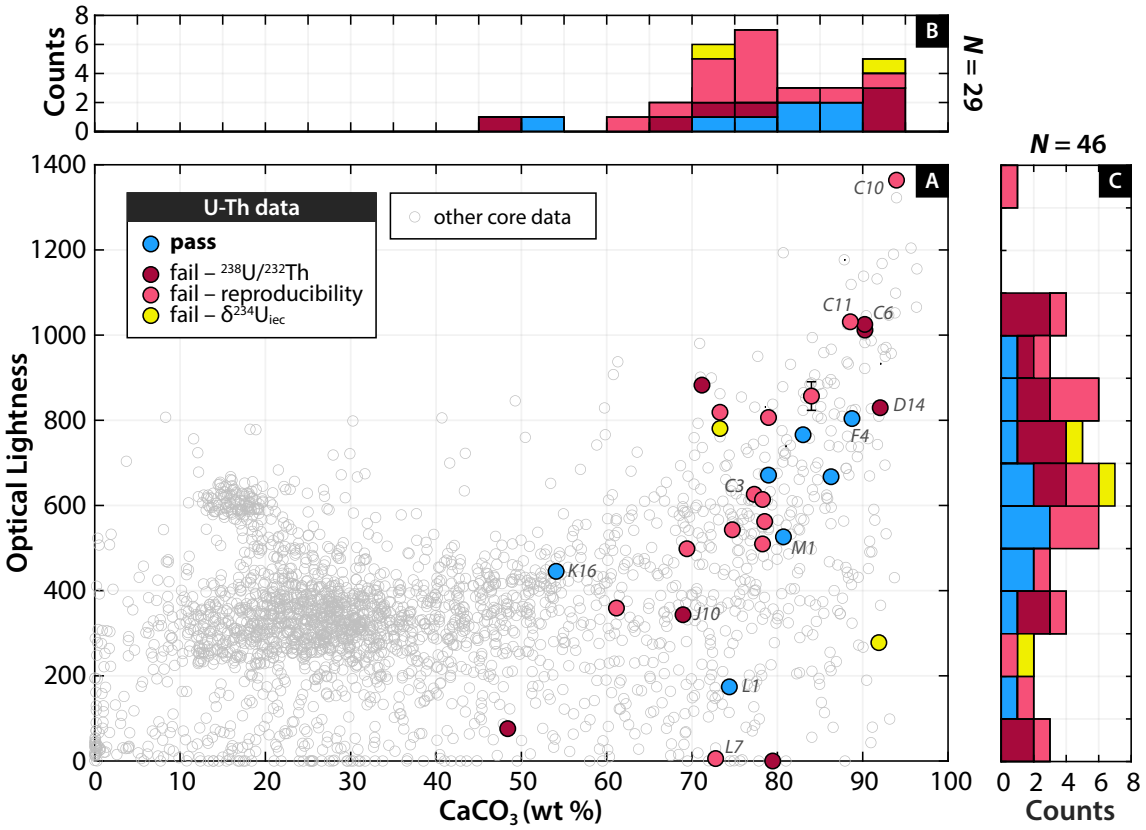

Figure 9: Cross-plot [**A**] and histograms of calcium carbonate content [**B**] and optical lightness [**C**], showing the distribution of these values for U-Th samples of each threshold criteria result. In Panel A, there are 29 colored circles which represent the U-Th samples that have both a corresponding $CaCO_3$ analysis (within 1 cm of the sample location) and a color reflectance measurement (within 2.5 mm of the sample location). Since color reflectance data were measured on a finer and more regular sampling interval than carbon data, there are more U-Th samples for which there is a corresponding color reflectance measurement ($N = 46$); thus, there are data plotted in the Panel C histogram that are not shown in Panels A and B. Empty circles with gray outlines represent other pairs of $CaCO_3$ and brightness data throughout the core and are only included if these data correspond to the exact same core depth. Note that this figure does not include any data from the upper 5 m of the core.

this detrital carbonate would be at secular equilibrium (Fig. 1D) and would thus introduce biases in the dating results. We compared the mineralogy of local carbonate bedrock to core sediments to see if mineralogical differences between these carbonates could be used to detect detrital contamination (Section S2). Unfortunately, the results show that there is no discernible difference between the carbonate bedrock and carbonate-bearing lake sediments, even when comparing different grain size groupings (see Fig. S2). All bedrock samples were dominated by low-Mg calcite, except one sample, which revealed the presence of dolomite. Low-Mg calcite was the dominant carbonate phase in all carbonate-bearing samples from the core, with no evidence of dolomite.

Despite the inconclusiveness of the mineralogical analyses, elemental ICP-MS concentration data support the prediction for detrital contamination in failed samples, especially those failing the $^{238}U/^{232}Th$ criterion. Fig. 10A is a biplot of the principal component coefficients for Ca, Mg, Sr, Fe,

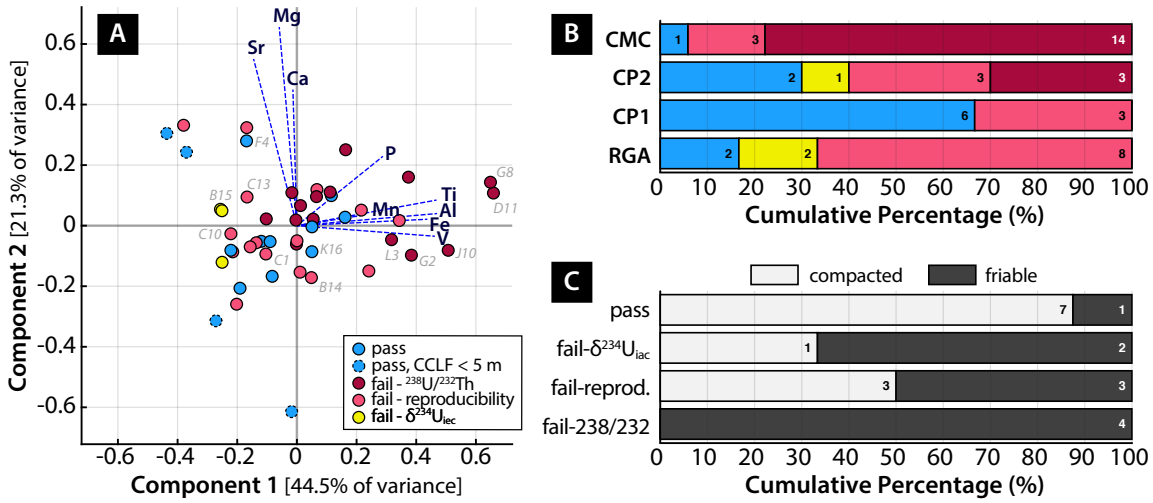

Figure 10: [**A**] Biplot of the principal component (PC) coefficients for Ca, Mg, Sr, Fe, Mn, Al, Ti, V, and P concentrations (dashed blue lines, labeled by element) and the PC scores for $N = 48$ samples (circles, color-coded by the threshold criteria result). Coefficients are scaled and projected into PC space. Light gray labels are corresponding sample IDs of samples that are featured in other figures; we encourage the reader to follow these labels in order to connect these plots with others. [**B**] Bar chart showing, for each facies, the relative proportion of samples that are each of the four threshold criteria results. **CMC** is cream-colored massive carbonate silt (Fig. 6); and **CP1** and **CP2** are cream-colored carbonate silts interbedded with peat layers; and **RGA** is red-green alternating varigated carbonate silt (Fig. 7). See Section 3 for further details. The bar colors follow the legend of Panel A. Numbers within each bar represent the actual number of samples; for example, of the 18 samples categorized as the CMC facies (top row), 1 passed, 3 failed the reproducibility criterion, and 14 failed the $^{238}U/^{232}Th$ criterion. [**C**] Bar chart showing the relative proportion of samples that are compacted (light) versus friable (dark) for samples of each threshold criteria result. Note that we qualitatively assessed sediment hardness for only 21 samples. As with Panel B, numbers within each bar represent the actual number of samples. Note that Panels B and C do not include U-Th samples from the upper 5 m of the core.

Mn, Al, Ti, V, and P and the principal component scores for each sample. Here, the first principal component (PC1) has positive coefficients for elements that are markers for aluminosilicates (Fe, Mn, Al, and Ti) and explains ∼44.5% of the variance in concentration data. Samples failing the $^{238}U/^{232}Th$ criterion generally have positive PC1 scores, indicating that those samples tend to have relatively higher concentrations of these elements. Elemental concentration data from a sample of the dark gray carbonate silt also exhibits higher concentrations of these elements (sample E2; Fig. 6, core at 35 m). As most samples that failed the $^{238}U/^{232}Th$ criterion are of the CMC facies (Fig. 10B), these data are consistent with our visual observations of this facies, in which the lighter-colored carbonates appear to have semi-gradational boundaries with the surrounding dark gray glaciogenic silts, suggesting that these samples likely contain some fraction of this material. In addition, the sample with the highest PC1 score, D11, comes from a boundary between cream-colored carbonate and dark gray carbonate silt (Fig. 6).

Despite the clear relationship between high PC1 scores and $^{238}U/^{232}Th$ criterion failing samples, samples with low PC1 scores are not ubiquitously well-behaved, indicating that another factor is influencing our data. Furthermore, there is no distinguishable difference in ^{232}Th concentrations of samples from different facies or passing versus threshold criteria failing samples. Interpreting the meaning of the second principal component (PC2) and the scores for other samples is less clear.

PC2 distinguishes among samples that have high values for Mg, Sr, and Ca. Comparison with total organic carbon data suggests that samples with negative PC2 scores have higher organic carbon content, but there are not enough corresponding carbon data to be conclusive.

6.2. Open system uranium remobilization

The data comparisons presented thus far broadly confirm that samples with higher $CaCO_3$ content are more likely to yield well-behaved U-Th dates, with the caveat that there are important inconsistencies with predictions for detrital contamination: mainly, that the samples with the highest $CaCO_3$ content and optical lightness fail the threshold criteria, especially the $^{238}U/^{232}Th$ criterion. Regarding the other sample data, there are no patterns distinguishing passing samples from samples failing the reproducibility and $\delta^{234}U_{iec}$ criteria in Figs. 9 and 10A. This information leads us to consider the next probable cause for poor sample behavior: the remobilization of uranium after initial carbonate formation. Using a qualitative assessment of sample hardness, we notice that passing samples were generally more compacted and dense, whereas failing samples were more friable and soft, especially those failing the $^{238}U/^{232}Th$ criterion (Fig. 10C). This observation fits our intuitive expectation that samples with less porosity would be more impervious to diagenesis or secondary deposition of uranium from porewater fluid flow (Fig. 1D).

We now refer back to the facies categorizations for further insight. From Fig. 10B, it is clear that facies alone does not dictate how each U-Th sample behaves. Instead, there are some broad tendencies: most CMC samples failed the $^{238}U/^{232}Th$ criterion; most RGA samples failed the reproducibility criterion; and most of the passing samples originate from the CP facies (CP1 and CP2). In considering the reasons behind these patterns, we compare both facies and threshold criteria results with uranium concentration, total organic carbon (TOC), and a*, the red-green color reflectance of sediment, where +a* values are more red and -a* values are more green (Fig. 11). The red or green color of sediments has been used as a qualitative indicator of the presence of iron-rich minerals and *in situ* redox conditions, in which red colors signify oxidizing conditions and green-gray colors suggest reducing conditions (Tomlinson, 1916; Lyle, 1983). With Fig. 11, we ask: do red-green color, uranium concentration, or TOC data form distinct distributions that follow facies or threshold criteria result categories? If so, what insight do these patterns give us into the mechanisms influencing our U-Th data?

The top half of Fig. 11 (Panels A–F) compares the mean a* of all measurements within 5 cm of the U-Th sample to the mean point-to-point difference in a* across the same interval (a measure of the 'volatility' of a* around each sample). For example, having a mean difference of 2 units/cm in a* means that the a* value changes, on average, by a magnitude of 2 along every cm within the 10 cm range surrounding the sample. Such a value would indicate significant volatility in red-green color, given that the total range of mean a* observed in U-Th samples is ∼3. From these panels, we notice that the CP samples are more red and occupy a relatively narrow range of mean a* values, whereas the CMC samples tend to be less red and exhibit less volatility in red-green color (Fig. 11D, F), particularly those failing the $^{238}U/^{232}Th$ criterion (Fig. 11A, E). These results are consistent with our qualitative observations of the CMC facies, in which the lighter colored carbonate occurs in ∼10–50 cm thick beds that are relatively uniform in color (Fig. 6).

Previous studies on sediments have interpreted changes in red-green color intensity as changes in the input of red iron-bearing materials (e.g., Giosan et al., 2002; Helmke et al., 2002; Ji et al., 2005), but because these iron-bearing minerals are highly sensitive to variations in redox environment, *in situ* reductive diagenesis can alter sediment color to be more green (Lyle, 1983; König et al., 1999; König et al., 2000). Thus, here we propose that the difference in a* values between the CP and CMC

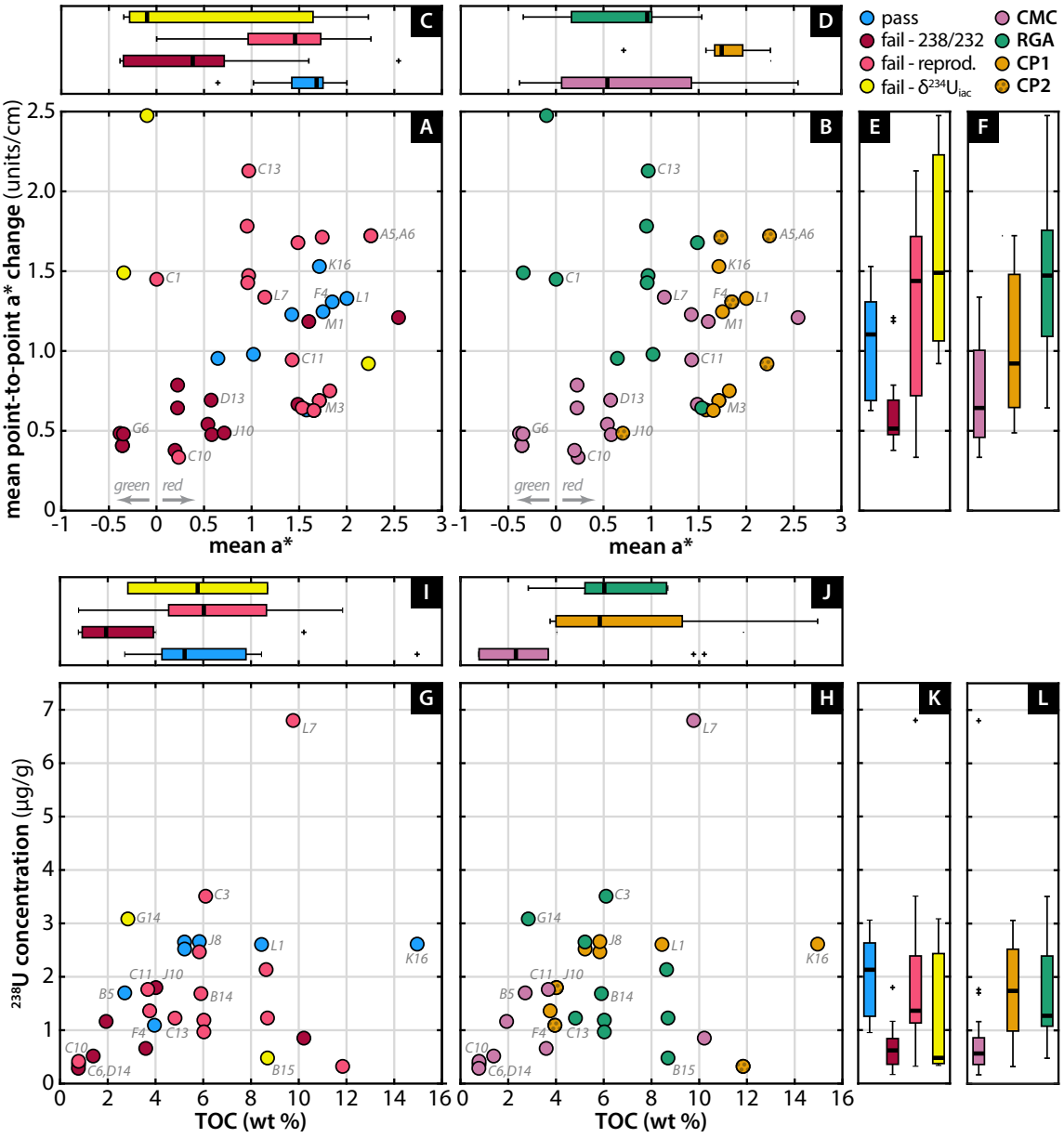

Figure 11: Cross-plots and box-and-whisker plots comparing the red-green color reflectance (a*; from the L*a*b* color space), total organic carbon (TOC) content, and ^{238}U concentration of U-Th samples and showing their relationship to threshold criteria result and facies. In all box-and-whisker plots, the thick central black line represents the median; the top and bottom edges of the box represent the 25th and 75th percentiles, respectively; the whiskers extend to the most extreme points not considered outliers; and the outliers are plotted as '+' symbols. A point is considered an outlier if it has a value >1.5x the interquartile range away from the 25th or 75th percentiles. The top half of the figure compares the mean a* of all measurements within 5 cm of the U-Th sample to the mean point-to-point difference in a* across the same interval. Note that there are some samples for which there is a ^{238}U concentration measurement but no corresponding TOC; thus, Panels K–L include data not shown in the cross-plots of Panels G–H. The bottom half of the figure compares TOC and ^{238}U concentration of each U-Th sample. Note that this figure does not include any data from the upper 5 m of the core.

samples is a reflection of diagenesis: the CP samples, being more red, have not been as altered by interactions with post-depositional reducing pore fluids and thus better preserve primary isotopic information to yield passing U-Th dates. In contrast, the CMC samples, which may have originally appeared more red like the CP samples, have been altered and as a result, have changed to a greener color.

Consistent with this hypothesis is the observation that the CMC and $^{238}U/^{232}Th$ threshold failing samples generally have much lower ^{238}U concentrations and TOC compared to other samples (Fig. 11G–L). Consider the following scenario: a package of endogenic carbonate containing organic matter is deposited and submerged under oxygenated conditions. After burial, oxygenated porewaters then interact with the organic matter and begin to degrade it, removing from the sediments any uranium associated with the organic matter (Section 2.2; Fig. 1D). This degradation of organic matter may decrease the local pH of pore fluids such that the pore fluids begin to alter the endogenic carbonate, leaching uranium originally bound within the crystal lattice. At some later point, the pore fluids are no longer recycled, and eventually all oxygen is depleted. The now reducing fluids then begin to reduce the surrounding sediment, shifting its color from red to more green. Any uranium that was removed from the carbonate into the pore fluid has now precipitated as authigenic uranium under these reducing conditions, but is no longer lattice-bound and thus is susceptible to further remobilization (Section 2.2; Fig. 1D). By the time we extract the core and measure the isotopic composition of these sediments, they are green (Fig. 11A–F), easy to physically disaggregate (Fig. 10C), and have low TOC and uranium concentrations (Fig. 11G–L). Thus, for the CMC facies, while detrital contamination is apparent given the elemental concentration data (Fig. 10), the initial ^{230}Th correction might have compensated to yield an accurate yet imprecise date, were it not for uranium loss.

As for why the CP facies would not be as affected by such pore fluids: we hypothesize that the thick peat beds associated with this facies protect the sediments from such altering fluids. In addition to acting as a hydraulically impermeable layer due to the close packing and small grain size of the organic material, the peats also act as a reductive barrier that prevents significant uranium removal and addition from the sediments. Unlike uranium in the CMC facies, any uranium remobilized by oxygenated porewaters from the cream-colored carbonate silts in the CP facies reprecipitates at the reducing peat boundaries and thus does not move relatively far. This proposed mechanism is based on the observation that the CP samples bounded on top by a thick (>10 cm) peat layer that is laterally continuous across multiple holes at the site (i.e., the CP1 facies) yield more passing dates with higher $^{238}U/^{232}Th$ ratios and probabilities of fit (Fig. 7 and 10B). In contrast, samples from the CP2 facies yield comparatively less ideal U-Th data (Fig. 10B). Fig. 7 features two depth-equivalent core sections from different holes which were classified as the CP2 facies. Examining images of these two core sections, it is clear that the uppermost layer of peat is not laterally continuous. Samples E12 and F4 are the only two samples of this facies that pass the threshold criteria, and are arguably the most tenuous of the passing dates: E12 has a $^{238}U/^{232}Th$ ratio of 1.02 and F4 has a probability of fit only slightly above 1%, both borderline values. Lastly, there are slight sedimentological differences between the CP1 and CP2 facies. While the CP1 facies exhibits faint horizontal banding, the CP2 carbonates tend to be comparatively darker in color and more massive. We speculate that this difference is caused by fabric-altering diagenetic processes (e.g., post-depositional fluid flow) that influenced CP2 more than CP1.

Thus far, we have multiple lines of evidence that point towards uranium loss as an explanation for the broad behavior of CMC samples, and the lack of such uranium remobilization in the CP facies can explain why CP samples more often pass the threshold criteria. As for the RGA samples,

these sediments tend to exhibit higher a* volatility (Fig. 11D, F), as one would expect for samples of a facies defined by alternating beds of red and green laminae (Fig. 6). Contrary to the CMC samples, the red-green color of the RGA facies seems to be controlled by sediment composition, given that the laminae are well-defined and the boundaries between color changes are sharp instead of diffuse. The sediment color of RGA facies dulled noticeably a few hours after initial core cutting and exposure, suggesting that iron-bearing minerals again strongly influence color. To explain the general lack of reproducibility of U-Th data from RGA samples (Fig. 10C), we speculate that the green layers containing ferrous iron may be reactive enough to remobilize Fe-Mn hydroxides that complex with uranium (Chappaz et al., 2010), leading to open system behavior that manifests as poor reproducibility. Reducing conditions would dissolve the oxides, releasing adsorbed uranium that would then reprecipitate and become re-adsorbed to other particles at a nearby redox front. A process which produces a net gain of uranium within the RGA facies would also help explain the observation that dates from this facies tend to yield dates that are younger than passing dates from the same depth interval (Fig. 16C).

6.3. Ostracode and mollusc shells

In this section, we compare our U-Th sample data to measures of ostracode color and mollusc shell abundance. As explored below, ostracode color and preservation may provide additional information about redox-related diagenesis, and mollusc shells may be prone to post-depositional uranium uptake that contributes to open system behavior.

During sample processing, we noticed that the color of ostracode shells often varied from sample to sample, ranging from translucent to dark gray or black. Because modern pristine ostracode shells are generally transparent and exhibit only trace pigmentation (Smith and Delorme, 2010), fossil ostracode shells with dark discoloration or coatings are thought to be altered and are avoided for geochemical analyses as a good practice (Holmes and Chivas, 2002). Many studies have made note of dark coatings on ostracode shells (e.g., Palacios-Fest et al., 2005; Wrozyna et al., 2012; Mackay et al., 2013), but there are few systematic studies that attempt to explain the origin and controls on ostracode discoloration or coatings (e.g., Ainsworth et al., 1990; Schwalb et al., 1995; Holmes, 1998).

The results of our comparison with ostracode shell color are broadly consistent with our hypothesis that the CMC facies has been altered by reductive diagenesis. Fig. 12 compares the threshold criteria result and facies with ostracode color, which we classified on a 7-point scale from translucent to black. Most CMC samples (5 out of 7) and all samples failing the $^{238}U/^{232}Th$ criteria had a higher proportion of darker shells. Sample B5, the only CMC sample that passed threshold criteria, has no ostracode shells with a color > 2. All other samples with different threshold criteria results and facies had ostracode assemblages comprised mainly of light-colored shells, with some exceptions.

We also noticed that most of the darker shells (color > 2) belonged to Darwinulidae, a family of benthic ostracodes that are considered an indicator of groundwater discharge. Schwalb et al. (1995) observed dark coatings on *Darwinula stevensoni* valves in Holocene sediments of Williams Lake (Minnesota, USA) and determined via wavelength- and energy-dispersive (WD/ED) spectrometry that the coatings were made of iron sulfide. They proposed that the coatings formed during periods of increased groundwater discharge, in which groundwater supplied additional Fe to the lake while reactive organic matter and sulfate led to reducing conditions that promoted iron sulfide formation. This mechanism is analogous to the one we propose to explain the color of the CMC facies, in which reducing conditions change the sediment color from red to green. Thus, the observation that most

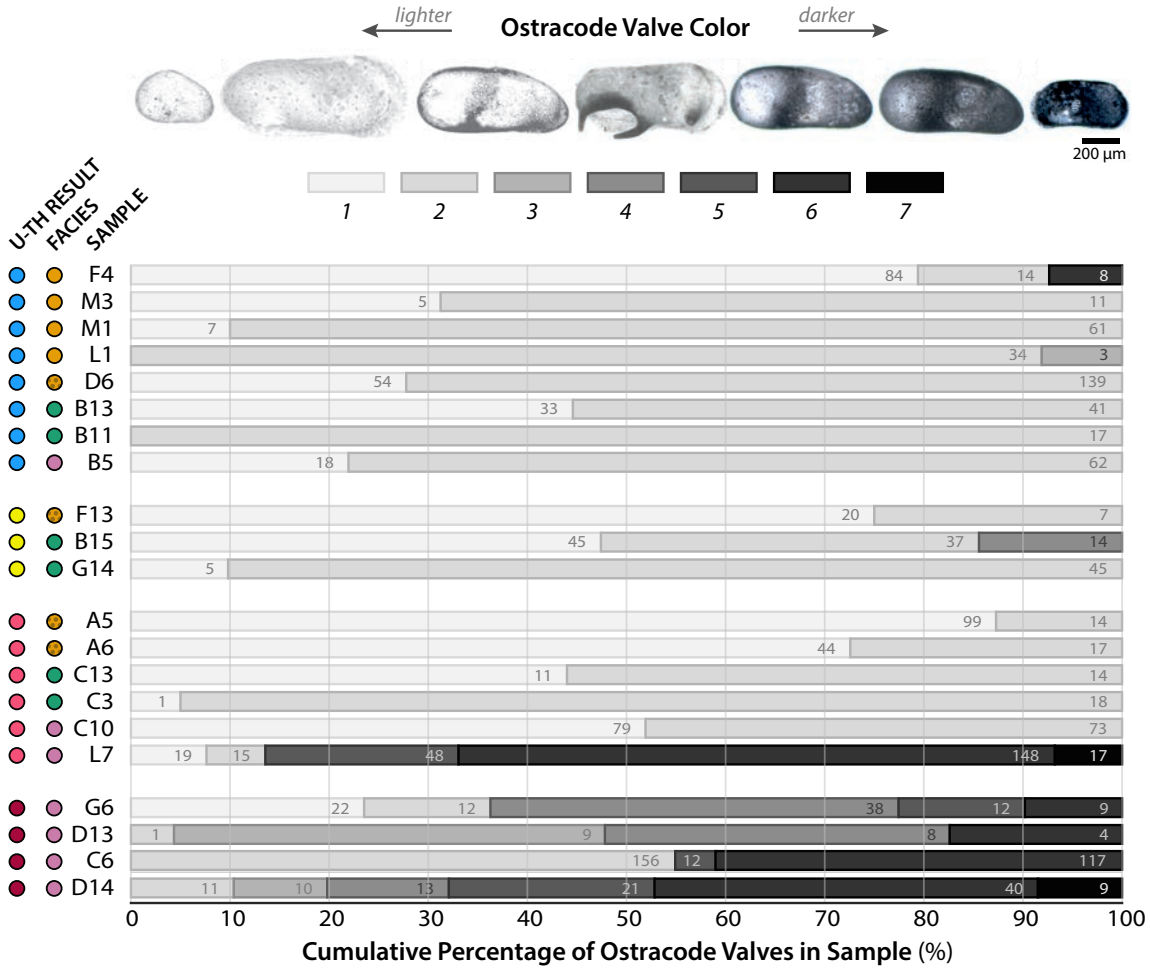

Figure 12: Relationship between ostracode color and U-Th data. Top row of microscope images of ostracode valves illustrate the coloration scale and are arranged from lightest to darkest on a scale of 1 to 7. The bar charts show the relationship between ostracode shell color, threshold criteria result, and facies for 21 samples. Each row in the chart represents ostracode count data from one sample. Rows of data are grouped together vertically by threshold criteria and then sorted within those groups by facies (see colored circles on the left). The length of bars in each row represents the relative proportion of shells in each sample that are of a particular color. The bar color represents the ostracode shell color. Numbers within bars indicate the actual number of valves of each color after normalizing sample masses. From the microscope images (left to right): (1) Translucent (LV, Cyprididae, sample B5); (2) White (RV, Limnocytheridae, sample D14); (3) Partly light gray (RV, Darwinulidae, sample D14); (4) Light gray (RV, Limnocytheridae, sample C6); (5) Partly dark gray (RV, Darwinulidae, sample C6); (6) Dark gray (RV, Darwinulidae, sample C6); (7) Black (LV, Limnocytheridae, sample L7). LV: Left valve external view, RV: Right valve external view.

CMC samples analyzed contained higher proportions of darker shells is consistent with the idea that the CMC facies has experienced more variable redox conditions, leading to uranium loss.

Aside from these observations, there were no other conclusive relationships between U-Th data and taphonomy (number of broken versus intact shells; adults versus juvenile counts) or ecology (benthic versus swimmer species; ornamentation). Future investigations should analyze the composition of the surface coatings with either WD/ED spectrometry or scanning electron microscope

energy-dispersive X-ray (SEM-EDX) analysis.

Regarding mollusc shells, extensive attempts to U-Th date mollusc shells for paleo-sea level reconstructions have shown that this material is prone to post-depositional uptake of uranium (Blanchard et al., 1967; Kaufman et al., 1971; McLaren and Rowe, 1996). Our date of mollusc shell fragments extracted from sample F14 confirms this, yielding an age ∼3000 yrs younger than that of the surrounding bulk sediment, ∼8 ka (see replicate F14(s) in Table A2). Although we visually screened for and manually removed identifiable mollusc shell fragments from samples before processing, it is possible that smaller unidentified fragments remained; if differential amounts of mollusc shell fragments were included in replicate analyses, poorly reproducing U-Th data might be an expected result. Qualitatively, we observed that on the centimeter scale, the RGA facies was generally more abundant in mollusc shell fragments than other facies.

7. Modeling the effects of detrital contamination and uranium remobilization

We have examined various sedimentological and geochemical data to evaluate a few hypotheses for poorly behaved U-Th data. In this section, we simulate the uranium and thorium isotopic evolution of samples with various compositions and uranium loss/gain pathways, and compare these model results with the actual measured isotopic composition of our samples (Figs. 13 and 14). Based on these results, we posit that the balance of evidence from both modeling and the previous data comparisons favors uranium remobilization as the main explanation for the observed scatter, rather than substantial detrital contamination.

To model the effects of detrital contamination, we calculate the impact of mixing varying amounts of detrital material with pure endogenic carbonate. We assume that the detrital end member material is isotopically homogeneous and at secular equilibrium, in which $[^{230}Th/^{238}U]$ and $[^{234}U/^{238}U]$ are both equal to 1. A dark gray silt sample extracted from a glaciogenic silt package (sample E2; Fig. 6) contained 30% $CaCO_3$, suggesting that limestone may be a significant component of the detritus entering Lake Junín. Thus, we set the composition of the detrital end member to 30% limestone and 70% aluminosilicate. The uranium and thorium concentrations of these detrital components are set to represent average values for marine limestone and the upper continental crust (Rudnick and Gao, 2003): U conc. = 2 ppm and Th conc. = 1 ppm for marine limestone, and U conc. = 2.7 ppm and Th conc. = 10.5 ppm for aluminosilicates. Using these values to simulate the detritus at Lake Junín seems within reason based on measurements of the uranium and thorium concentrations of E2. Although organic matter is a non-negligible constituent of our samples (1–16% TOC; Fig. 11) and is likely a meaningful uranium source (Fig. 1D), we chose to exclude organics in our model as a necessary simplification for this exercise. As such, the modeling results should be treated as proofs of concept, rather than a serious attempt to precisely quantify the manner by which each deviating U-Th date occurs.

We focus on modeling two groups of data: samples from ∼20–23 m and samples from ∼70–75 m. Taking the passing U-Th dates within these groups at face value, these depth ranges correspond to samples with nominally true ages of ∼75 and ∼550 ka, respectively. The scatter of threshold criteria failing data at ∼20–23 m all originate from the CMC facies and are generally biased older relative to the passing dates, whereas the data at ∼70–75 m mostly consists of the RGA facies and are biased younger (Fig. 16B).

7.1. Modeling results for ∼75 ka-aged samples (20–23 m)

Fig. 13A compares our U-Th data of samples from ∼75 ka (circles) to our simulations of isotopically evolving samples (colored lines) in $^{230}Th/^{238}U$ activity-$\delta^{234}U$ space. All models of samples

are evolved for 75 kyrs. To orient the reader: the measured isotopic composition of the two passing samples in this depth range, K16 and L1, are marked by the pair of gray circles located adjacent to the pair of blue circles (see legend). The horizontal offset between the colored and gray circles represents the effect of the initial ^{230}Th correction, the magnitude of which is controlled by the ^{238}U/^{232}Th ratio (Eq. 3). The gray shaded region delineates the age range prescribed by the age-depth model (to be shown and discussed in Section 8); here, we treat this range as the "true" age range of all samples shown. Thus, any colored circles that do not fall within the gray shaded region are samples that yielded apparent dates that are inconsistent with the true age of these sediments (see straight lines labeled by date). The goal of the subsequent exercises is to explore what pathways of isotopic evolution can explain the isotopic composition of these outlying data.

We first approximate the starting isotopic composition of a representative endogenic carbonate by reverse engineering the isotopic composition of the passing samples, K16 and L1. These samples have an average uranium concentration of 2.6 ppm, carbonate content of ∼60%, and TOC of ∼10%. These values indicate that non-carbonate detrital material in these samples accounts for ∼30% of the sample composition. Using these constraints, we find that a sample consisting of the following material can roughly match the end isotopic composition of K16 and L1 after evolving for 75 kyrs: 20–30% detrital material and 70–80% endogenic carbonate with a starting composition of $\delta^{234}U_{iec}$ = 2700‰ and uranium concentration = 2.8 ppm (Fig. 13A, colored lines labeled 20% and 30%; see legend). We then simulate the isotopic evolution of a pure endogenic carbonate of this composition over the same amount of time, 75 kyrs: with no ^{232}Th, its initial ^{230}Th/^{238}U activity is zero and its final isotopic composition matches its true age (blue pathways in Fig. **??**). Adding detrital material to this pure endogenic carbonate increases the initial ^{230}Th/^{238}U activity and decreases the initial δ^{234}U of the sample (red pathways in Fig. 13B–C), causing the sample to yield an older apparent date after 75 kyrs (red pathways in Fig. 13A).

From the pathways simulating the impact of detritus in Fig. 13A (red pathways), it is clear that no amount of detrital material is able to explain the samples with high measured ^{230}Th/^{238}U activities. Varying the relative proportions of limestone to aluminosilicate in the detrital end member does not make any meaningful difference. Furthermore, the ^{232}Th concentrations of these samples place an inexact but actionable upper bound on how much detrital material is reasonable; for example, a 30% contribution of detrital material that is 50% limestone already produces a sample with ^{232}Th concentrations of ∼1.7 ppm, higher than that of all samples from this depth range (Fig. 13G).

Thus, we invoke uranium loss to explain these data, and simulate the impact of continuous, late, and early uranium loss on the sample isotope composition (see legend and Fig. 13D–E). The samples from this depth range are also the same low uranium CMC samples failing the ^{238}U/^{232}Th criterion described earlier. We cannot infer which of these uranium loss scenarios is most likely at work from isotopic measurements alone, but our hypothesis for reductive diagenesis of the CMC samples described in Section 6.2 would favor early loss. In addition, the magnitude of uranium loss required to approach the isotopic composition of the outlying samples is similar to the difference in uranium concentration between passing and failing samples (Fig. 13F).

Note that these modeled uranium loss pathways are simplified to assume that loss occurs with no fractionation between ^{234}U and ^{238}U. Although preferential leaching of ^{234}U in a uranium loss scenario is possible (e.g., Robinson et al., 2006), this simplification does not change the conclusion that the data from ∼20–23 m cannot be explained by detrital contamination alone, and must evoke a mechanism for uranium remobilization.

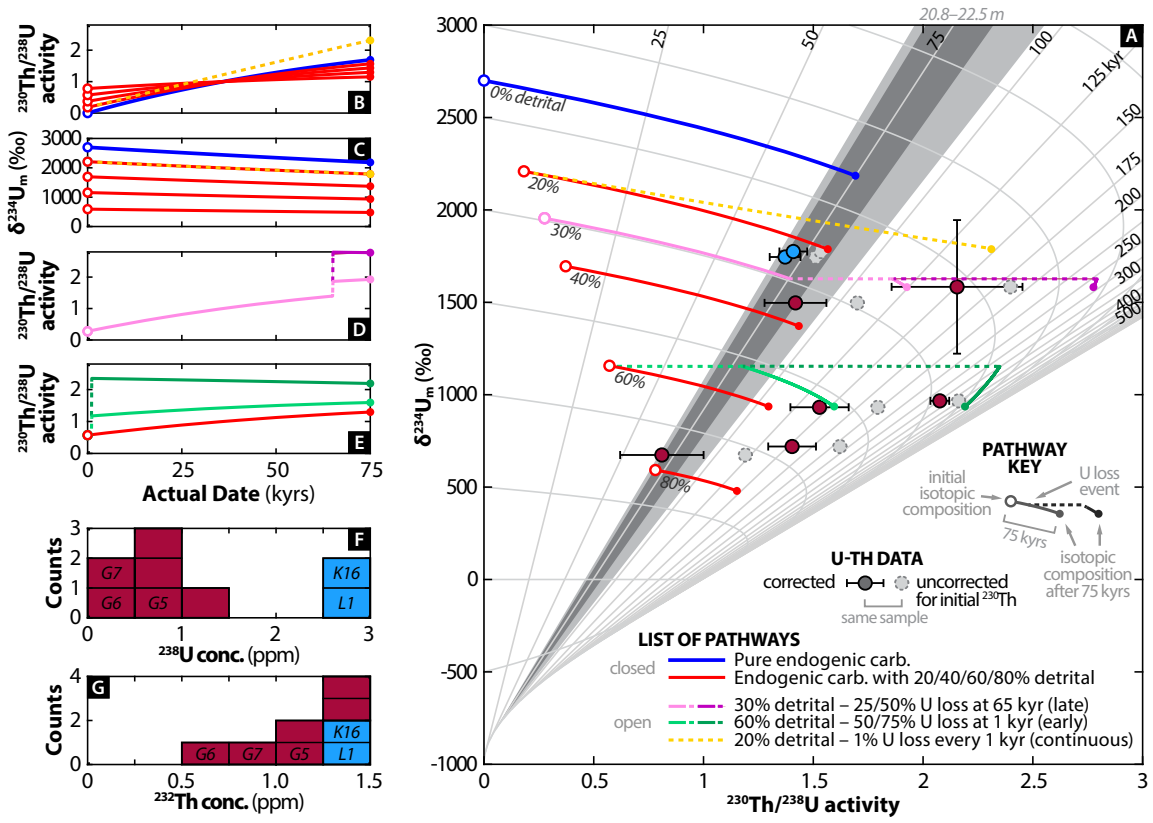

Figure 13: Possible pathways of uranium-thorium isotopic evolution that may explain the outlying data at ∼20–23 m. [**A**] Comparison of U-Th data (circles with error bars) with possible pathways (colored lines) in $\delta^{234}U$–$^{230}Th/^{238}U$ activity space, following Fig. 1C. Corrected U-Th ratios (color-coded by threshold criteria result) are each paired with their corresponding uncorrected ratios (gray circles with dashed outlines). The gray triangular wedges represent the expected age range of samples from this depth range based on the age-depth model, where the dark gray area is the range of model means (red line in Fig. 16A) and the light gray area is the maximum and minimum of the 95% confidence interval (shaded gray area in Fig. 16A). Colored lines represent the isotopic evolution of sample material of mixed composition and uranium loss histories over 75 kyrs (see list of pathways and pathway key for symbology). The simulated samples are mixtures of two isotopically homogeneous end-members: pure endogenic carbonate and detrital material made of 30% limestone and 70% aluminosilicate material. The starting composition of the pure endogenic carbonate is 2.8 ppm ^{238}U and 2700‰ for $\delta^{234}U_{iec}$. These calculations assume that the endogenic carbonate contains no initial ^{230}Th and that uranium loss occurs with no fractionation between ^{234}U and ^{238}U. [**B**] and [**C**] Change in the isotopic evolution as the proportion of detrital material increases (red lines). [**D**] and [**E**] Change in $^{230}Th/^{238}U$ activity after uranium loss. $\delta^{234}U$ is not shown because its evolution is no different from that without uranium loss (compare dashed yellow line with red line of same starting composition in Panel C). [**F**] and [**G**] ^{238}U and ^{232}Th concentrations of U-Th samples in this depth range. K16 and L1 are of the CP1 facies; all other U-Th data featured are of the CMC facies (see Fig. 16B).

7.2. Modeling results for ∼550 ka-aged samples (70–75 m)

Fig. 14 features the U-Th samples from ∼550 ka. At this age, the close spacing of the age isolines in this regime causes the area defining the "true" age range of these samples to occupy a much narrower area in $^{230}Th/^{238}U$ activity-$\delta^{234}U$ space (shaded gray area in Fig. 14B). Here, applying the same reverse engeineering steps described in Section 7.1 using passing samples in this

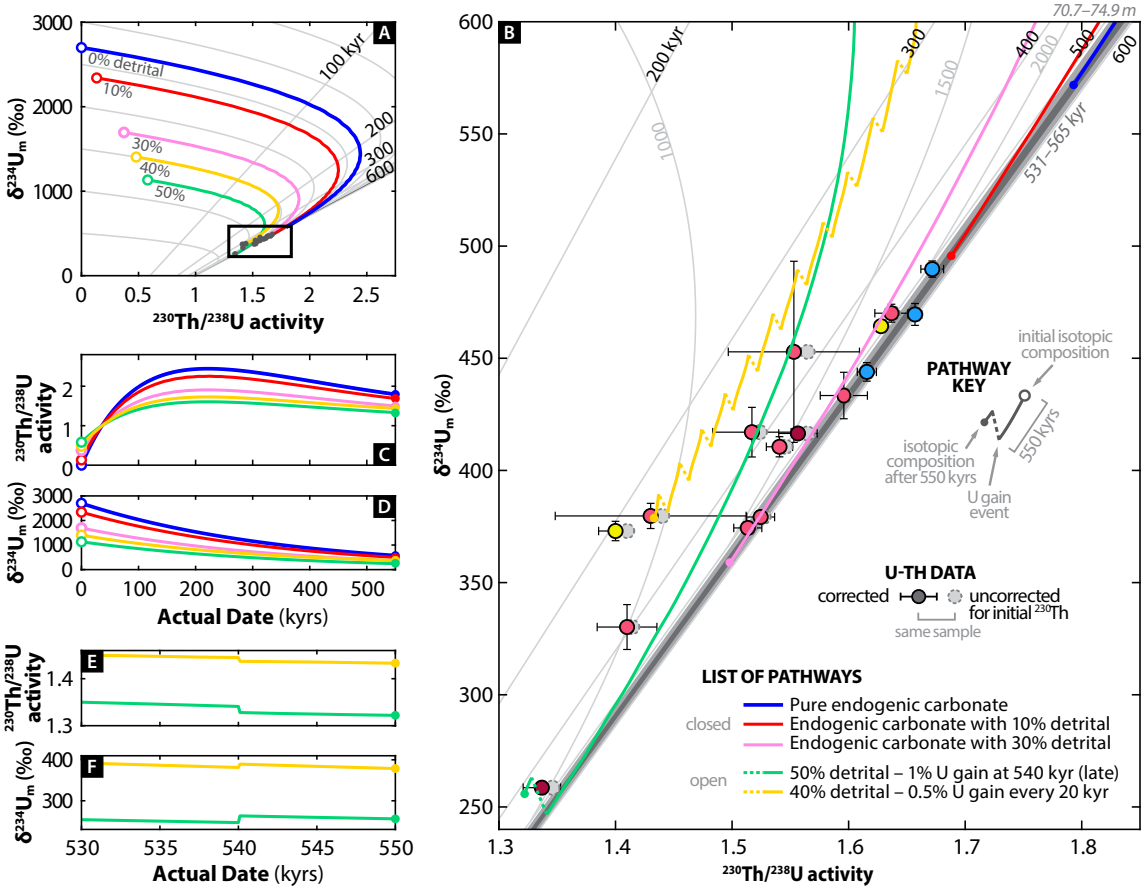

Figure 14: Possible pathways of uranium-thorium isotopic evolution that may explain the outlying data at ∼70–75 m. See caption in Fig. 13 for explanation of symbology. [**A**] Initial isotopic composition and evolution of pathways over 550 kyrs. [**B**] View of the isotopic evolution of samples within the extent represented by rectangular inset in Panel A. The gray triangular wedges represent the expected age range of samples from this depth range. The starting composition of the pure endogenic carbonate is 1.8 ppm ^{238}U and 2700‰ for $\delta^{234}U_{initial}$. The detrital component has the same composition as that from Fig. 13, 30% limestone and 70% aluminosilicate material. These simulations assume that uranium gain occurs with a δ^{234}U ratio equal to the $\delta^{234}U_{initial}$ of the sample. [**C**] and [**D**] Change in isotopic evolution as the proportion of detrital material increases. [**E**] and [**F**] Change in isotopic evolution after uranium gain.

depth interval, we start with a pure endogenic carbonate with a composition of $\delta^{234}U_{initial} = 2700‰$ and $^{238}U = 1.8$ ppm. Taking this endogenic carbonate and mixing it with detritus, we find that detrital contamination has much less impact on the accuracy of the dates at this age, demonstrated by the fact that all the modeled pathways of samples with varied percentages of detrital material still ultimately end in the region defining the true age of the sediments (gray shaded region in Fig. 14B; see Section 2.2 for explanation). In order to produce samples with isotopic compositions that bias dates to be younger, we simulate the impacts of uranium gain.

Similar to detrital contamination, at this age, early uranium loss (or gain) has no effect on the

final sample date. Thus, in Fig. 14B, we only illustrate the impacts of late or continuous uranium gain (green and yellow pathways). In contrast to the pathways observed for ∼75 ka-aged sediments, here very small percent gains in uranium can have measurable impacts. For example, a late 1% gain at 540 kyrs (10 kyrs before measurement) can cause the sample date to be ∼100 kyrs younger (green pathway in Fig. 14B). Thus, the sensitivity of the apparent dates in this regime to small alterations in uranium, in combination with narrowly spaced age isolines, is likely the cause for the large spread of dates at this depth (Fig. 8D). Because early uranium gain cannot explain the young bias of these samples, the hypothesis for post-depositional uranium uptake by gastropod shells seems less convincing; gains would have to be continuous and gradual, and it is unclear from where the continuous supply of uranium would come.

Note that although Figs. 13–14 do not explore compound gain/loss pathways, such scenarios are not outside the realm of possibility. Furthermore, although some studies on open system behavior in corals and caves use models to correct U-Th data (e.g., Thompson et al., 2003, Scholz et al., 2014), we make no attempts to apply such corrections to our data.

8. Conclusions: the age-depth model for the PLJ-1 splice

Through the use of threshold criteria that evaluate samples on the basis of their $^{238}U/^{232}Th$ ratio, reproducibility, and $\delta^{234}U_{iec}$, we have conducted a methodical curation of the U-Th data that is justified by comparisons to other sedimentological, geochemical, and paleoecological datasets, as well as modeling of the isotopic evolution of simulated samples. As a result, we deem 18 of the 55 sample dates as satisfactory for use as age constraints. These passing samples generally come from sediments of the CP facies, which we hypothesize have experienced relatively less uranium remobilization because of the thick overlying peat beds that act as physical and reductive barriers to post-depositional fluid flow. Fig. 15 summarizes our provisional explanation for the sources and post-depositional behavior of uranium and thorium for each facies and the evidence supporting our interpretation. Given that Lake Junín has likely experienced dramatic changes in water level and redox conditions over time (Woods et al., 2019), the strong evidence for uranium remobilization reflected by the U-Th data is unsurprising.

Fig. 16A shows the age-depth model for the PLJ-1 splice using these U-Th ages and radiocarbon data. The model was generated using the R-based Bayesian age-depth modeling software program called Bacon (v2.3; Blaauw and Christen, 2011). On average, the 95% confidence range of this model is ∼30 kyrs. Trachsel and Telford (2017) tested Bacon and other age-depth modeling routines (CLAM, OxCal, BChron) on a varved sediment sequence and found that they all produced mean age-depth models close to the truth, but each program has its own advantages and disadvantages. In the case of Bacon, the application of an accumulation rate prior forces sedimentation rates to be more smooth and linear than might be justified. Thus, while the alternating packages of carbonate and glaciogenic silt in the core hint at variability in sedimentation rates, this information is not utilized in the generation of the age-depth model. See Section S5 for details regarding the sensitivity of the age-depth model to chosen parameters and priors used for the model run.

Fig. 16A also compares the radiometric age-depth model to geomagnetic relative paleointensity (RPI) tie points made between the PLJ-1 normalized remanence record and well-dated RPI stacks (Hatfield et al., 2020a). Broadly, these data are consistent with the age-depth model and provide further support for the validity of our passing U-Th ages.

As a result of our work, the PLJ-1 record of Lake Junín is now poised to offer new insights on past climate and environmental changes in the tropical Andes, complementing and testing the long

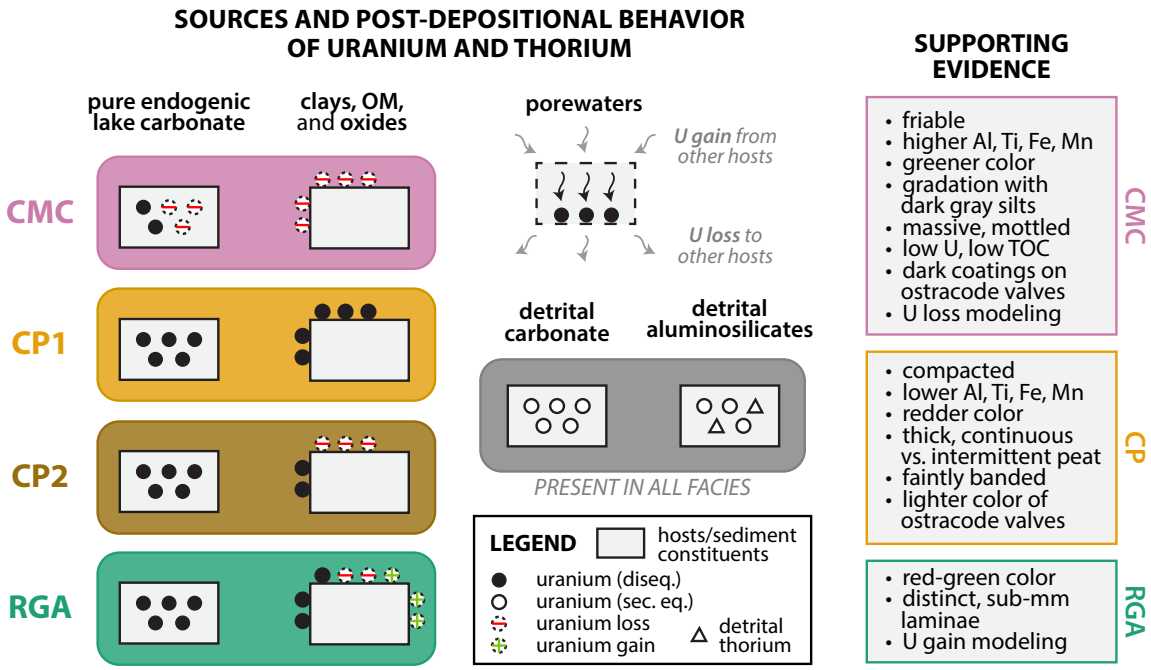

Figure 15: Summary of hypothesized sources and post-depositional behavior of uranium and thorium in different carbonate facies of the PLJ-1 lake sediments, based on observations and modeling presented in this paper. Gray boxes with circles and triangles follow the same representation as those in Fig. 1D, in which shapes within boxes represent uranium or thorium bound within the crystal lattice, and shapes around boxes represent elements adsorbed to the substrate surface. Post-depositional uranium loss (dashed circle with red minus sign) and gain (dashed circle with green plus sign) is facilitated by porewaters (gray box with dashed outline). All facies contain some amount of detritus containing detrital bedrock limestone and aluminosilicates. Supporting evidence for these interpretations is listed in boxes on the right for each facies.

but tuned sediment records from Sabana de Bogotá to the north (∼5°S; Groot et al., 2011) and Lake Titicaca to the south (∼16°S; Fritz et al., 2004, 2007).

9. Considerations for future U-Th dating of lake sediments

When it comes to U-Th dating of lake sediments, there are no "silver bullets" or easy answers: no singular facies, carbonate content threshold, color, or any other sedimentological or geochemical data could predict the viability of a U-Th date with certainty in these sediments. In fact, samples that conventionally would be considered ideal were some of the most poorly behaved samples. One wonders what the outcomes might have been if only the nominally choicest samples had been processed, and the dateability of the entire core assessed from those results. Such decision making processes are the norm when less time and fewer resources are available.

Our concern for overlooked but dateable sediments in other records also extends in the opposite direction: other studies may be overly reliant on single-analysis U-Th dates that seem credible but have not been reproduced or tested with stratigraphic coevality constraints. The most glaring example can be shown through the results from sample L7, which had the highest uranium

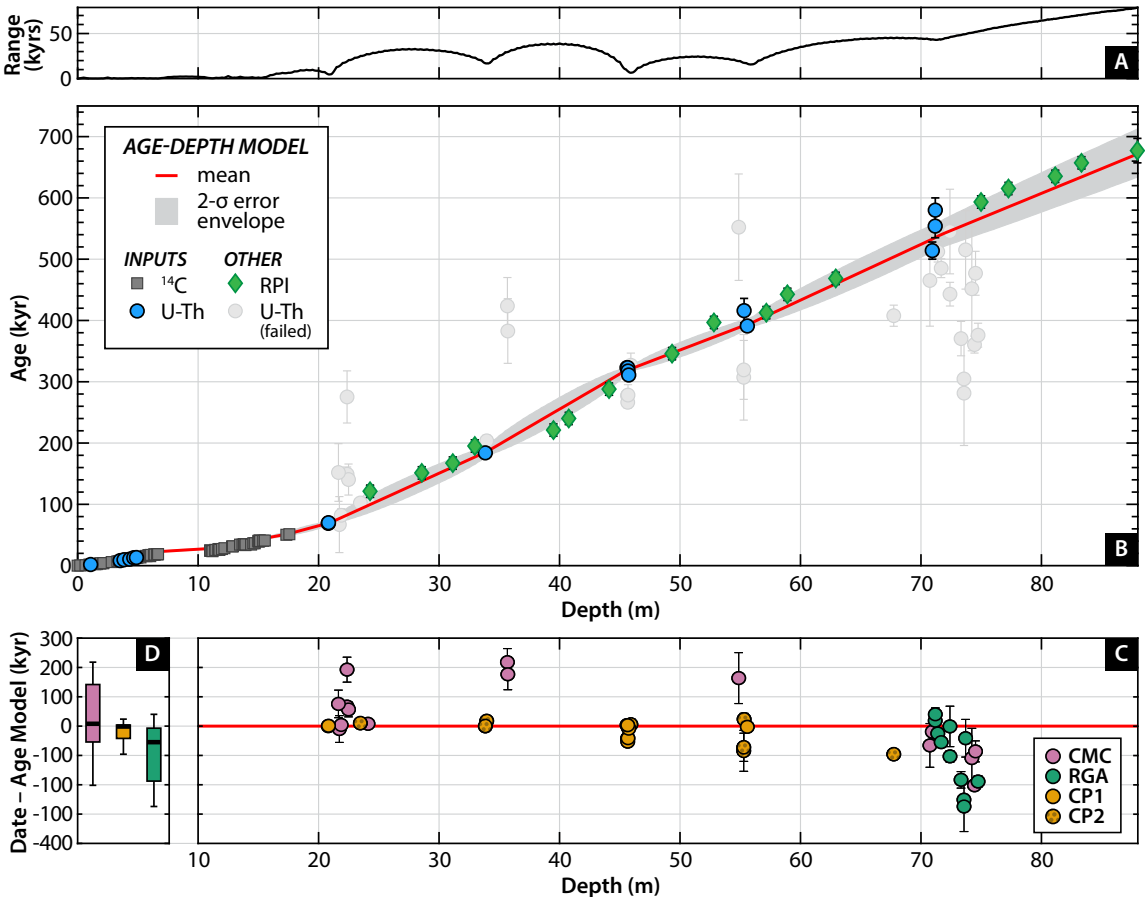

Figure 16: [**A**] and [**B**] Age-depth model for the PLJ-1 splice generated by Bacon (Blaauw and Christen, 2011) using radiocarbon (gray squares; Woods et al., 2019) and U-Th (blue circles; this study) data. Red line represents the mean and gray shaded area is the 2-σ range error envelope. Panel A shows the range of the 95% confidence interval with depth. U-Th data that did not meet threshold criteria (light gray circles) and relative paleointensity (RPI) tie points (green diamonds; Hatfield et al., 2020a) were not used as inputs for the age-depth model and are plotted as an overlay. Section S5 for additional information on the priors and posteriors of the model. [**C**] Comparison of all U-Th dates and their departure from the age-depth model mean (thick red line at zero), color-coded by facies. See Fig. 8D to compare with data color-coded by threshold criteria result. [**D**] Box-and-whisker plots showing the distribution by facies of the difference between U-Th dates and the age-depth model mean; see caption of Fig. 11 for description of box-and-whisker plot symbology. All error bars shown are of 2-σ range. Analyses that yielded indeterminant U-Th dates or were infinite are not included in this figure.

concentration (7 ppm, 2 times higher than the next highest) and highest $^{230}Th/^{232}Th$ out of all samples (Table A3), two metrics traditionally used to evaluate sample dateability. Because of these characteristics, individual analyses were rather precise, with 400–700 year uncertainties (2-σ) on ∼100 ka dates. On their own, these dates would be considered excellent, but only after replication is it revealed that none of the precise dates overlap with one another at the 95% confidence level.

Although a labor intensive strategy, there is no substitute for replication and reproducibility in assessing the quality of U-Th geochronological data.

Furthermore, while the threshold criteria ultimately decided which data would form the foundation of the age-depth model, it was the placement of geochronological data in context of other sedimentological and geochemical information that provided justification for these thresholds. These data comparisons also provide practical insights on what other characteristics to consider for future U-Th dating attempts on lake sediments: for instance, the aforementioned L7 sample contained some of the darkest ostracode shells categorized (see image of ostracode shell with color = 7 in Fig. 12).

Embracing the noise in our data has led to a richer understanding of the controls on uranium in these lake sediments. As our ability to resolve this noise increases as the analytical precision of measurements improves, subtle differences in the noise will become interpretable as information on paleoenvironmental processes themselves. This work demonstrates the beginnings of what is possible on this front. Although >150 analyses went into this work, we hope that this number does not intimidate those seeking to apply U-Th dating to their own lake sediment samples. Rather, we seek to showcase strategies for interpreting scattered geochronologic data of any size and encourage similar efforts where better geochronological control would have the most impact. As more high resolution datasets become paired with drill cores by default (e.g., scanning XRF, color reflectance, magnetic susceptibility), there will be more opportunities to use such additional data to test underlying working assumptions for geochronologic tools.

Of all the lessons learned, we hold the following as most important: for the determination of the age of lake sediments, geologic context—in the form of sedimentological observations, geochemical data, and paleoecological descriptions—is of equal importance to the numerical accuracy and precision of geochronological measurements.

10. Datasets and Tools

Datasets and tools related to this article can be found in the Appendix and the following open-access data repository hosted at Zenodo (operated by CERN): http://dx.doi.org/10.5281/zenodo.3788100. Products available for use include

- U-Th data tables for the PLJ-1 and 1996 core (with all digits preserved where possible, for reproducibility and data longevity);
- sample locations and corresponding elemental concentrations, carbon coulometry, color reflectance, and ostracod paleoecological data;
- the radiometric-based age-depth model; and
- a spreadsheet for simulating the uranium isotopic evolution of a sample that has undergone open system behavior with respect to uranium and/or a sample of mixed composition (impure carbonate).

11. Author Contributions

Following the Contributor Roles Taxonomy (CRediT; Brand et al., 2015), we provide a statement of the diverse contributions to this published work. **Christine Y. Chen**: Conceptualization, Methodology, Software, Validation, Formal Analysis, Investigation, Writing - Original Draft Preparation, Writing - Review and Editing, Visualization, Project Administration. **David McGee**: Conceptualization, Methodology, Resources, Writing - Review & Editing, Supervision, Funding Acquisition. **Arielle Woods**: Methodology, Writing - Review & Editing. **Liseth Pérez**: Methodology, Investigation, Writing - Review & Editing. **Robert G. Hatfield**: Writing - Review & Editing. **R. Lawrence Edwards**: Conceptualization, Resources, Writing - Review & Editing. **Hai Cheng**: Investigation. **Blas L. Valero-Garcés**: Investigation, Writing - Review & Editing. **Sophie B. Lehmann**: Writing - Review & Editing. **Joseph S. Stoner**: Writing - Review & Editing. **Antje Schwalb**: Methodology, Resources, Writing - Review & Editing. **Irit Tal**: Investigation. **Geoffrey O. Seltzer**: Conceptualization. **Pedro Miguel Tapia**: Project Administration. **Mark B. Abbott**: Conceptualization, Writing - Review & Editing, Supervision, Project Administration, Funding Acquisition. **Donald T. Rodbell**: Conceptualization, Writing - Review & Editing, Supervision, Project Administration, Funding Acquisition.

A more specific description of contributions is as follows: GOS laid the foundation for this work in the 1990s (Siegel et al., 2005). MBA, DTR, and DM conceived of the project and secured funding. CYC and DM formulated the research goals and methodology. CYC collected, processed, and analyzed the U-Th samples from the PLJ-1 splice; made comparisons to the other datasets; designed and implemented the model for uranium isotopic evolution; and prepared the original draft and figures, all with supervision from DM. IT assisted with processing of U-Th analyses. RLE oversaw U-Th dating of the 1996 piston core, which was conducted by HC. BLVG provided the stratigraphic core description. DM collected the elemental ICPMS concentration data. CYC initiated the ostracode work with LP, who analyzed the ostracodes with input from AS. DTR analyzed carbon coulometry and mineralogy XRD data. RH and JS analyzed paleomagnetic data. CYC made the age-depth model, with input from AW, SL, RGH, DM, JSS, MBA, and DTR. CYC, AW, RGH, JSS, PMT, MBA, and DTR contributed to the fieldwork campaign. DM, AW, LP, RGH, RLE, BLVG, SL, AS, MBA, and DTR provided manuscript feedback. All authors provided expertise.

12. Acknowledgments

This research was supported by a grant from the International Continental Drilling Program (ICDP) and grants from the U.S. National Science Foundation (McGee, EAR-1404414; Rodbell, EAR-1402076; Abbott, EAR-1404113; Stoner, EAR-1400903) and the National Science Foundation of China (Cheng, #41888101). CYC was supported by an NSF Graduate Research Fellowship during the execution of this research. We are grateful to Lake Junín Drilling Project members for their contributions to fieldwork and data collection, the ICDP for financial and logistical support, the authorities of the Reserva Nacional Junín for their assistance, and DOSECC Exploration Services (USA) and GEOTEC (Peru) for drilling expertise. We thank LacCore for access to facilities, core curation, color reflectance data, and data management. We thank Doug Schnurrenberger, Amy Myrbo, Shane Loeffler, Darren Larsen, Mark Shapley, Bryan G. Valencia, Angela Rozas Davila, James Bartle, and Cecilia Oballe for their logistical assistance during drilling; Kristina Brady and Anders Noren for their work managing and coordinating this project; Liam Glennon for assisting

with XRD analyses; Ben Hardt for providing lab assistance at MIT; and Sarah Katz and Naomi Levin for collecting modern water samples used for uranium isotope analysis. CYC also thanks resources for making graphics accessible to those with color vision deficiencies by Wong (2011) and Martin Krzywinski (http://mkweb.bcgsc.ca/colorblind); and P. Donut for companionship and support with revisions. We also gratefully acknowledge Jay Quade, Tim Lowenstein, Kristin Bergmann, C. Brenhin Keller, Adam Maloof, Noah Anderson, Marjorie Cantine, Adam Jost, Christopher Kinsley, Gabi Serrato Marks, Josh Murray, and Ruth Tweedy for reading the initial draft and providing helpful comments. We also gratefully acknowledge two anonymous reviewers for their constructive feedback, Ana Moreno for refereeing our manuscript, and Antje Voelker for the invitation to submit this paper to Quaternary Science Reviews.

Table A1: U-Th data for replicate analyses of each sample from the 1996 piston core. All uncertainties listed are 2-σ. **Replicate ID** refers to a unique identifier for each replicate analysis. **Depth** is the depth below the sediment-water interface. For depths marked with an asterisk (*), the true depth of these samples was lost; depths listed are estimated and represent the midpoint depth of the drive corresponding to each sample. The midpoint depth was selected because most other samples appeared to be sampled from the midpoints of their respective drives. An uncertainty of ±0.5 m is assigned to these samples and shown as errorbars when data are plotted versus depth (the length of drives is generally 1.0 m). Reported errors for ^{238}U and ^{232}Th concentrations are estimated to be ±2% due to uncertainties in spike concentration; analytical uncertainties are smaller. **Date Uncorr.** indicates that no correction has been made for initial ^{230}Th. **Date Corr.** are corrected for initial detrital ^{230}Th assuming an initial atomic ^{230}Th/^{232}Th of 8.0±4.0×10^{-6} (Section 4), and are reported relative to Before Present (BP), in which the present is defined as January 1, 1950. Decay constants for ^{230}Th and ^{234}U are from Cheng et al. (2013); decay constant for ^{238}U is 1.55125×10^{-10} yr^{-1} (Jaffey et al., 1971). See Eqs. 1–3 for equations for the calculation of dates. See Eq. 2 for the calculation of $\delta^{234}U_{initial}$ and Section S3 for the calculation of $\delta^{234}U_{iec}$. See Supplemental Materials for additional information about samples.

Replicate ID	Depth (m)	^{238}U (ng/g)	^{232}Th (ng/g)	$\delta^{234}U_m$ (‰)	[^{230}Th/^{238}U] (activity)	^{230}Th/^{232}Th (atomic ppm)	Date Uncorr. (yrs BP)	Date Corr. (yrs BP)	$\delta^{234}U_{initial}$ (‰)	$\delta^{234}U_{iec}$ (‰)
Replicate analyses consistent with the radiocarbon chronology										
DR3-0	0.9	319.50±0.60	48.60±0.10	2540.0±7.0	0.1034±0.0026	11.20±0.30	3101±82	800±1200	2547±11	2657±66
DR3-1	0.9	816.0±1.0	23.360±0.070	2693.0±4.0	0.05573±0.00077	32.10±0.40	1535±23	1130±210	2702.5±4.3	2724±14
DR3-2	0.9	1029.0±2.0	35.40±0.10	2688.0±6.0	0.05333±0.00080	25.60±0.40	1465±24	970±250	2696.3±6.3	2722±19
DR3-3	0.9	941.0±2.0	28.70±0.10	2697.0±5.0	0.05227±0.00075	28.20±0.40	1430±22	990±220	2705.5±5.3	2728±16
DR5-1	2.53	464.0±1.0	11.070±0.060	3330.0±5.0	0.1246±0.0010	86.10±0.80	3052±26	2760±150	3357.2±5.2	3379±16
DR5-2	2.53	587.0±1.0	13.340±0.060	3345.0±7.0	0.1252±0.0012	91.0±1.0	3057±31	2780±140	3372.5±7.2	3394±18
DR5-3	2.53	484.0±1.0	18.000±0.080	3267.0±8.0	0.1330±0.0018	59.10±0.80	3320±48	2860±230	3294.6±8.4	3328±25
DR6-1	3.5*	409.80±0.70	14.900±0.040	3069.0±6.0	0.1542±0.0015	70.10±0.70	4073±42	3600±240	3101.4±6.4	3132±21
DR6-2	3.5*	283.50±0.40	9.700±0.040	3216.0±7.0	0.1545±0.0017	74.50±0.80	3933±46	3510±220	3249.1±7.4	3280±22
DR8-0	5.53	365.0±1.0	30.30±0.10	2846±14	0.2359±0.0021	46.90±0.40	6732±68	5600±570	2892±15	2959±47
DR8-1	5.53	544.0±1.0	55.20±0.20	2865.0±5.0	0.2450±0.0028	39.90±0.50	6967±84	5590±700	2911.5±7.7	2994±48
DR8-2	5.53	993.0±2.0	78.00±0.30	2870.0±7.0	0.2443±0.0018	51.30±0.50	6936±55	5870±540	2919.0±8.4	2983±38
DR8-3	5.53	526.0±1.0	43.20±0.20	2842.0±9.0	0.2390±0.0020	48.00±0.40	6832±62	5710±570	2889±10	2955±41
DR10-22-D	7.39	374.12±0.67	17.09±0.34	2555.8±7.9	0.2844±0.0052	102.7±2.8	8890±170	8220±380	2616.7±8.6	2650±25
DR10-0	7.585*	993.0±2.0	95.20±0.20	2598.0±5.0	0.2872±0.0024	49.40±0.40	8866±79	7470±710	2654.3±7.4	2726±42
DR11-02-E	8.02	559.1±1.0	43.46±0.87	2614.8±5.6	0.3558±0.0049	75.5±1.8	11040±160	9920±590	2689.9±7.3	2748±35
DR11-1	8.538	1916.0±3.0	95.80±0.30	2739.0±3.0	0.3576±0.0027	118.0±1.0	10715±86	10020±360	2818.5±4.2	2857±23
DR11-2	8.538	1546.0±4.0	81.50±0.30	2747.0±7.0	0.3444±0.0022	107.90±0.80	10277±72	9550±370	2823.0±7.8	2864±27
DR11-3	8.538	2270.0±4.0	137.90±0.70	2734.0±5.0	0.3547±0.0025	96.40±0.80	10639±80	9790±430	2811.6±6.2	2859±28
DR11-82-F	8.82	1948.9±3.8	42.60±0.86	2786.5±5.2	0.4610±0.0023	347.8±7.2	13824±75	13530±170	2895.9±5.5	2913±14
Replicate analyses inconsistent with the radiocarbon chronology or indeterminate U-Th dates										
DR10-22-A	7.39	366±1	46.40±0.93	2513.0±5.2	0.4299±0.0023	56.0±1.0	13904±82	12030±950	2600.7±8.8	2694±55
DR10-22-B	7.39	265.54±0.29	25.30±0.51	2554.8±4.6	0.4534±0.0038	78.5±1.7	14530±130	13140±710	2652.2±7.2	2723±41
DR10-22-C	7.39	256.81±0.37	22.01±0.44	2557.7±6.2	0.4508±0.0063	86.7±2.1	14420±220	13180±660	2655.6±8.1	2719±38
DR21-10-G	17.26	1989.8±9.3	6910±140	-4.4±2.4	1.364±0.012	6.48±0.14	–	–	–	–

Table A1 continued from previous page

Replicate ID	Depth (m)	^{238}U (ng/g)	^{232}Th (ng/g)	$\delta^{234}U_m$ (‰)	[^{230}Th/^{238}U] (activity)	^{230}Th/^{232}Th (atomic ppm)	Date Uncorr. (yrs BP)	Date Corr. (yrs BP)	$\delta^{234}U_{initial}$ (‰)	$\delta^{234}U_{iec}$ (‰)
DR21-46-H	17.62	2815.9±6.7	6560±130	-54.4±2.5	1.1910±0.0058	8.43±0.17	–	–	–	–
DR21-50-I	17.66	2344.7±4.6	6080±120	-119.9±1.9	1.1508±0.0061	7.32±0.15	–	–	–	–
DR21-54-J	17.7	996.8±1.5	2692±54	136.8±2.5	1.3561±0.0061	8.28±0.17	–	–	–	–
DR21-58-K	17.74	767.4±1.2	2148±43	386.2±3.1	1.5523±0.0070	9.14±0.19	–	–	–	–
DR21-58-O	17.74	1365.8±2.4	2342±47	925.8±3.6	0.8960±0.0044	8.62±0.18	–	–	–	–
DR22-02-L	17.92	948.7±1.5	3073±62	398.4±2.9	1.5288±0.0067	7.78±0.16	–	–	–	–
DR22-26-M	18.16	1579.7±2.7	4717±95	66.6±2.3	1.1992±0.0059	6.62±0.14	–	–	–	–
DR22-30-N	18.2	1256.0±2.1	3053±61	74.8±2.6	1.2821±0.0053	8.70±0.18	–	–	–	–
DR22-30-P	18.2	1254.4±5.7	3455±71	406.8±5.4	1.312±0.011	7.85±0.17	–	–	–	–

Table A2: U-Th data for replicate analyses of each sample from the PLJ-1 core. All uncertainties listed are 2-σ. **Rep. ID** refers to a unique identifier for each replicate analysis. Note that sample 'F14(s)' refers to an analysis of gastropod shells from the same horizon as F14. Reported errors for ^{238}U and ^{232}Th concentrations are estimated to be ±2% due to uncertainties in spike concentration; analytical uncertainties are smaller. **Date Uncorr.** indicates that no correction has been made for initial ^{230}Th. **Date Corr.** are corrected for initial detrital ^{230}Th assuming an initial ^{230}Th/^{232}Th of $8.0\pm4.0\times10^{-6}$ (Section 4), and are reported relative to Before Present (BP), in which the present is defined as January 1, 1950. Decay constants for ^{230}Th and ^{234}U are from Cheng et al. (2013); decay constant for ^{238}U is 1.55125×10^{-10} yr^{-1} (Jaffey et al., 1971). See Eqs. 1–3 for equations for the calculation of dates. See Eq. 2 for the calculation of $\delta^{234}U_{initial}$ and Section S3 for the calculation of $\delta^{234}U_{iac}$.

Samp. ID	Rep. ID	^{238}U (ng/g)	^{232}Th (ng/g)	$\delta^{234}U_m$ (‰)	[^{230}Th/^{238}U] (activity)	^{230}Th/^{232}Th (atomic ppm)	Date Uncorr. (years BP)	Date Corr. (years BP)	$\delta^{234}U_{initial}$ (‰)	$\delta^{234}U_{iec}$ (‰)
Replicates of Threshold Passing Samples										
F9	F9(1)	2831±57	97.5±2.0	2356.7±1.1	0.07300±0.00060	33.67±0.29	2272±20	1710±280	2368.9±2.2	2391±13
	F9(2)	2940±59	147.4±3.0	2354.87±0.95	0.07805±0.00082	24.71±0.26	2440±27	1620±410	2366.5±2.9	2399±19
	F9(3)	2962±59	127.8±2.6	2353.5±1.1	0.07708±0.00082	28.36±0.30	2409±27	1700±360	2365.6±2.6	2394±16
F14	F14(1)	737±15	26.29±0.53	2635.37±0.68	0.28880±0.00099	128.59±0.49	8821±32	8290±270	2698.7±2.2	2725±15
	F14(2)	715±14	29.16±0.59	2640.01±0.82	0.2838±0.0016	110.42±0.62	8649±50	8040±310	2701.5±2.5	2732±17
	F14(3)	725±15	28.26±0.57	2652.8±6.3	0.2823±0.0014	114.98±0.57	8569±46	7990±290	2714.3±6.8	2743±21
	F14(4)	611±12	17.08±0.34	2625.96±0.69	0.27407±0.00084	155.78±0.42	8374±27	7960±210	2686.5±1.7	2707±12
	F14(s)	291.9±5.8	5.48±0.11	2636.3±3.6	0.1765±0.0012	149.3±1.3	5275±39	4990±150	2674.6±3.8	2688±11
F15	F15(1)	1000±20	119.7±2.4	2694.2±2.2	0.3748±0.0019	49.72±0.23	11404±61	9650±890	2769.5±7.3	2863±53
	F15(2)	997±20	99.0±2.0	2741.1±1.0	0.3624±0.0019	57.96±0.30	10860±61	9420±730	2815.9±5.9	2894±44
	F15(3)	944±19	96.9±1.9	2728.17±0.97	0.3621±0.0022	55.96±0.33	10890±70	9400±760	2802.4±6.1	2883±46
F16	F16(1)	1259±25	353.7±7.1	2546.1±1.6	0.4304±0.0049	24.33±0.28	13780±170	9400±2200	2616±17	2830±130
	F16(2)	1048±21	155.4±3.1	2717.5±6.4	0.4197±0.0025	44.96±0.22	12764±83	10600±1100	2801±11	2919±69
C16	C16(1)	1305±26	205.5±4.1	2084.2±2.5	0.4278±0.0024	43.12±0.23	15901±96	13100±1400	2163.6±9.0	2261±59
	C16(2)	1673±33	258.2±5.2	2088.26±0.47	0.4159±0.0023	42.78±0.22	15409±90	12700±1400	2165.2±8.4	2260±57
	C16(3)	1773±35	264.5±5.3	2083.6±3.8	0.4105±0.0023	43.69±0.23	15218±95	12600±1300	2159.8±9.0	2251±56
D4	D4(1)	1946±39	500±10	1930.39±0.61	0.4514±0.0034	27.87±0.20	17800±140	13000±2500	2003±14	2154±95
	D4(2)	2073±41	520±10	1929.5±2.5	0.4549±0.0033	28.78±0.21	17950±140	13300±2400	2004±14	2151±92
	D4(3)	1943±39	489.1±9.8	1935.47±0.82	0.4508±0.0038	28.44±0.24	17740±160	13100±2400	2009±14	2157±92
	D4(4)	1916±38	477.4±9.6	1942.0±1.2	0.4438±0.0040	28.28±0.25	17400±170	12800±2400	2014±14	2161±92
K16	K16(1)	3861±77	2049±41	1768.0±1.0	1.5022±0.0068	44.95±0.19	77450±470	67800±5100	2142±31	2500±240
	K16(4)	2258±45	1257±25	1750.7±2.2	1.520±0.017	43.35±0.48	79400±1200	69300±5500	2129±33	2510±250
	K16(5)	2357±47	1267±25	1713.3±1.9	1.506±0.016	44.48±0.48	79900±1200	70000±5400	2088±32	2450±240
	K16(6)	2293±46	1266±25	1746.5±1.9	1.524±0.017	43.81±0.48	79800±1200	69800±5500	2127±33	2500±250
	K16(7)	2290±46	1294±26	1746.9±1.8	1.509±0.017	42.39±0.48	78800±1200	68400±5600	2120±34	2510±260
L1	L1(2)	3570±71	1984±40	1780.6±1.1	1.6487±0.0075	47.09±0.21	87430±560	77600±5200	2217±33	2610±260
	L1(5)	2358±47	1113±22	1772.4±2.0	1.528±0.015	51.40±0.49	79100±1000	70600±4600	2164±28	2480±210
	L1(6)	2314±46	1106±22	1774.2±1.9	1.529±0.015	50.79±0.51	79100±1100	70500±4600	2166±28	2490±210
	L1(7)	2381±48	1115±22	1772.8±1.8	1.473±0.015	49.91±0.50	75230±1000	66800±4500	2141±28	2450±200
	L1(8)	2403±48	1171±24	1773.6±2.3	1.499±0.015	48.83±0.50	77000±1100	68200±4700	2151±29	2480±220
D6	D6(1)	1091±22	841±17	1347.5±1.2	2.209±0.013	45.48±0.27	193700±2600	179900±7900	2240±50	2840±420
	D6(2)	1070±21	806±16	1385.4±1.7	2.291±0.013	48.28±0.26	202200±2700	189300±7500	2364±50	2980±430
	D6(3)	1259±25	1141±23	1212.9±2.7	2.151±0.027	37.69±0.47	211500±6500	194000±12000	2100±69	2790±520

Table A2 continued from previous page

Samp. ID	Rep. ID	^{238}U (ng/g)	^{232}Th (ng/g)	$\delta^{234}U_m$ (‰)	[^{230}Th/^{238}U] (activity)	^{230}Th/^{232}Th (atomic ppm)	Date Uncorr. (years BP)	Date Corr. (years BP)	$\delta^{234}U_{initial}$ (‰)	$\delta^{234}U_{iec}$ (‰)
	D6(4)	1283±26	1104±22	1241.5±2.0	2.111±0.026	38.94±0.47	195900±5400	180000±11000	2061±62	2690±470
	D6(5)	1288±26	1103±22	1252.2±1.8	2.117±0.018	39.23±0.33	194800±3800	178600±9800	2074±58	2710±470
M1	M1(1)	2505±50	427.0±8.5	935.7±2.0	2.1324±0.0049	198.65±0.37	327000±3600	324200±3900	2337±26	2451±85
	M1(2)	2497±50	411.7±8.2	938.4±1.1	2.1321±0.0046	205.34±0.34	324600±3100	321900±3400	2328±23	2438±78
	M1(3)	2496±50	417.4±8.4	936.29±0.64	2.1351±0.0044	202.73±0.29	328300±2900	325500±3300	2347±22	2459±78
	M1(4)	2582±52	462.2±9.2	933.7±1.0	2.1213±0.0050	188.15±0.35	321500±3300	318500±3600	2295±24	2412±84
M3	M3(1)	1828±37	373.8±7.5	1004.66±0.81	2.2154±0.0051	172.03±0.31	324400±3200	321200±3600	2488±25	2635±99
	M3(2)	1820±36	384.4±7.7	1010.6±2.2	2.2234±0.0051	167.10±0.27	324800±3500	321400±4000	2504±29	2660±110
	M3(3)	1854±37	410.1±8.2	991.3±1.2	2.2034±0.0051	158.19±0.28	327500±3300	323900±3800	2474±27	2630±110
	M3(4)	1599±32	342.6±6.9	993.9±5.6	2.207±0.011	163.54±0.69	327900±8300	324500±8500	2484±61	2640±160
	M3(5)	1596±32	366.7±7.4	997.2±4.0	2.213±0.011	152.93±0.70	328600±7700	324900±8000	2496±58	2660±160
J8	J8(1)	2590±52	315.1±6.3	987.7±1.6	2.1837±0.0041	285.00±0.34	318200±2700	316200±2900	2412±20	2494±62
	J8(2)	2607±52	328.0±6.6	988.5±1.6	2.1862±0.0046	275.81±0.43	319200±3000	317100±3100	2420±22	2506±66
	J8(3)	2782±56	379.5±7.6	979.8±1.3	2.1785±0.0043	253.53±0.34	321000±2800	318800±3000	2410±21	2503±68
J9	J9(1)	3055±61	1156±23	810.79±0.64	1.9655±0.0064	82.48±0.25	320600±4500	313400±5900	1964±33	2190±160
	J9(2)	3058±61	1191±24	804.54±0.79	1.9548±0.0060	79.71±0.22	318600±4100	311100±5700	1936±31	2170±160
	J9(3)	3064±61	1192±24	807.1±1.3	1.9547±0.0058	79.79±0.20	316400±4000	308900±5700	1931±31	2160±160
E12	E12(1)	907±18	845±17	664.1±2.8	1.890±0.014	32.23±0.27	454000±31000	437000±34000	2280±220	3060±810
	E12(2)	913±18	821±16	663.9±2.8	1.880±0.012	33.20±0.21	436000±23000	419000±26000	2170±160	2870±650
	E12(3)	977±20	1053±21	606.4±3.5	1.779±0.035	26.22±0.52	397000±54000	373000±59000	1740±300	2500±1000
	E12(4)	991±20	1024±21	599.3±4.5	1.780±0.034	27.34±0.52	412000±60000	390000±64000	1800±340	2500±1100
	E12(5)	976±20	975±20	620.7±3.5	1.809±0.033	28.74±0.52	413000±56000	393000±60000	1880±330	2600±1100
F4	F4(1)	1006±20	116.2±2.3	818.5±2.1	2.0592±0.0054	283.16±0.61	394700±7100	392900±7200	2482±51	2560±110
	F4(2)	1003±20	115.9±2.3	811.9±2.2	2.0516±0.0049	281.86±0.51	396100±6800	394300±6900	2471±49	2550±110
	F4(3)	1140±23	122.3±2.4	822.0±1.1	2.0557±0.0044	304.29±0.52	385600±5000	383900±5100	2430±35	2503±83
	F4(4)	1157±23	122.1±2.4	813.5±1.8	2.0545±0.0057	309.03±0.78	397100±7400	395400±7400	2484±53	2560±120
	F4(5)	1154±23	123.2±2.5	818.6±1.9	2.0638±0.0064	306.99±0.87	400000±8300	398400±8400	2520±60	2600±130
B5	B5(1)	1693±34	352.7±7.1	494.4±2.1	1.6751±0.0050	127.68±0.30	503000±21000	499000±21000	2020±120	2150±270
	B5(2)	1702±34	393.9±7.9	488.2±1.1	1.6745±0.0052	114.89±0.33	536000±25000	532000±26000	2190±160	2340±360
	B5(3)	1687±34	355.4±7.1	488.7±2.5	1.6726±0.0087	126.04±0.63	524000±41000	521000±41000	2130±250	2250±540
	B5(4)	1690±34	354.2±7.1	490.6±2.2	1.6727±0.0088	126.71±0.65	514000±37000	510000±38000	2070±230	2200±480
	B5(5)	1721±34	362.0±7.3	486.7±3.6	1.6686±0.0098	125.93±0.69	519000±46000	515000±47000	2090±280	2210±610
B11	B11(1)	2501±50	331.3±6.6	447.3±1.2	1.6230±0.0041	194.52±0.37	567000±28000	565000±28000	2200±180	2290±370
	B11(2)	2501±50	318.5±6.4	445.21±0.84	1.6214±0.0043	202.18±0.46	576000±30000	574000±30000	2250±190	2330±400
	B11(3)	2787±56	389.2±7.8	445.3±2.8	1.6149±0.0048	183.58±0.47	537000±31000	535000±31000	2020±180	2100±380
	B11(4)	2819±56	374.2±7.5	437.9±1.9	1.6049±0.0053	191.98±0.59	540000±30000	537000±30000	1990±180	2070±370
B13	B13(1)	1280±26	131.9±2.6	468.4±1.1	1.6559±0.0041	255.10±0.46	588000±31000	587000±31000	2450±220	2520±450
	B13(2)	1218±24	116.1±2.3	471.6±4.9	1.6556±0.0059	275.87±0.65	558000±51000	556000±52000	2270±340	2330±710
	B13(3)	1401±28	145.5±2.9	471.25±0.86	1.6568±0.0036	253.31±0.46	568000±23000	566000±23000	2330±150	2400±320
	B13(5)	1372±27	141.3±2.8	466.9±3.0	1.6605±0.0053	256.07±0.72	645000±74000	644000±74000	2870±630	3000±1300

Table A2 continued from previous page

Samp. ID	Rep. ID	^{238}U (ng/g)	^{232}Th (ng/g)	$\delta^{234}U_m$ (‰)	[^{230}Th/^{238}U] (activity)	^{230}Th/^{232}Th (atomic ppm)	Date Uncorr. (years BP)	Date Corr. (years BP)	$\delta^{234}U_{initial}$ (‰)	$\delta^{234}U_{iec}$ (‰)
Replicates of Threshold Failing Samples										
P10	P10(1)	726±15	800±16	794.4±1.5	0.543±0.013	7.83±0.18	38100±1000	–	792±57	1130±360
	P10(2)	772±15	874±18	791.2±1.0	0.536±0.013	7.52±0.18	37600±1100	–	785±59	1130±380
L3	L3(1)	619±12	1118±23	719.6±3.0	1.621±0.025	14.25±0.22	210300±8200	152000±47000	1100±150	2200±1300
G1	G1(1)	851±17	1230±130	673.8±2.0	1.19±0.12	13.1±1.9	121000±21000	67000±46000	810±110	1340±660
G2	G2(1)	1167±23	1485±30	1504.84±0.76	1.720±0.020	21.46±0.25	109100±2000	83000±16000	1900±86	2910±860
	G2(2)	1161±23	1386±28	1488.7±2.8	1.681±0.020	22.37±0.26	106500±1900	82000±15000	1875±79	2780±750
G5	G5(1)	635±13	1395±28	966.7±1.7	2.162±0.040	15.61±0.29	321000±25000	275000±43000	2100±260	5200±4200
G6	G6(1)	435.9±8.7	792±16	1041.8±2.3	1.902±0.025	16.62±0.22	195000±5800	150000±32000	1590±150	3200±1700
	G6(2)	315.3±6.3	614±12	1772.4±6.1	2.567±0.029	20.93±0.23	182100±4300	150000±21000	2710±160	5800±3400
	G6(3)	316.0±6.3	639±13	1777.8±1.8	2.586±0.031	20.30±0.24	184100±4600	151000±22000	2720±170	6100±3900
	G6(4)	336.2±6.7	721±14	1741.8±4.0	2.539±0.033	18.79±0.24	182400±4900	145000±24000	2630±180	6300±4600
G7	G7(1)	414.1±8.3	831±17	955.3±5.9	1.831±0.025	14.48±0.19	199400±6400	144000±43000	1440±180	3200±2200
	G7(2)	426.5±8.5	839±17	925.6±3.7	1.768±0.024	14.27±0.19	191300±5800	135000±44000	1360±170	2900±1900
	G7(3)	413.7±8.3	818±16	915.1±6.0	1.784±0.024	14.32±0.19	198000±6300	142000±44000	1370±180	3000±2000
G8	G8(1)	861±17	2362±48	621.9±3.9	1.986±0.035	11.50±0.20	–	–	–	–
M15	M15(1)	327.4±6.5	38.91±0.78	2306.98±0.78	2.2407±0.0058	299.35±0.64	104960±410	103350±910	3089.3±8.0	3193±58
	M15(2)	313.5±6.3	35.45±0.71	2310.06±0.98	2.2675±0.0057	318.39±0.64	106680±400	105160±870	3109.2±7.7	3208±56
	M15(3)	322.6±6.5	42.20±0.85	2300.3±1.5	2.1937±0.0065	266.23±0.65	102030±450	100300±1000	3053.5±8.9	3166±64
	M15(4)	327.3±6.5	36.66±0.73	2294.4±1.5	2.1731±0.0055	308.04±0.61	100910±380	99370±860	3038.2±7.6	3134±54
L7	L7(1)	6960±140	383.1±7.8	1690.0±1.4	1.8670±0.0044	538.4±2.5	110310±410	109390±620	2302.0±4.4	2337±21
	L7(2)	6430±130	372.4±7.6	1686.3±1.5	1.7499±0.0042	479.5±2.0	100290±370	99300±620	2232.4±4.4	2268±22
	L7(3)	7340±150	451.5±9.2	1691.47±0.64	1.9770±0.0046	510.6±1.9	120560±450	119550±680	2371.0±4.6	2411±24
	L7(4)	6460±130	392.9±8.0	1687.04±0.74	1.8028±0.0041	470.4±1.9	104780±360	103750±630	2261.7±4.2	2300±23
	L7(5)	6920±140	417.7±8.4	1692.2±1.5	1.8034±0.0041	474.2±1.3	104520±370	103500±630	2267.1±4.5	2305±23
	L7(6)	6590±130	388.6±7.8	1682.24±0.70	1.8101±0.0040	487.5±1.2	105720±350	104730±610	2261.5±4.0	2298±22
	L7(7)	6900±140	393.6±7.9	1684.15±0.78	1.7943±0.0047	499.6±1.4	104220±420	103250±640	2254.6±4.2	2290±22
D7	D7(1)	850±17	1029±21	1310.5±1.5	2.322±0.020	30.45±0.26	227400±5100	206000±13000	2344±89	3500±940
	D7(2)	825±17	965±19	1346.2±1.7	2.339±0.019	31.76±0.25	221900±4600	201000±13000	2378±85	3490±890
D11	D11(1)	365.0±7.3	725±64	289.1±1.1	1.33±0.11	10.7±1.3	–	–	–	–
	D11(2)	419.7±8.4	1025±21	278.7±2.1	1.493±0.039	9.71±0.26	–	–	–	–
D12	D12(1)	228.8±4.6	456.0±9.2	596.8±1.8	1.829±0.036	14.57±0.29	–	–	–	–
	D12(2)	294.8±5.9	424.9±8.5	806.1±1.5	2.080±0.024	22.91±0.26	447000±42000	424000±46000	2670±360	4400±1900
D13	D13(1)	161.4±3.2	204.2±4.1	862.8±2.5	2.168±0.018	27.20±0.22	467000±35000	448000±38000	3060±340	4700±1600
	D13(2)	161.8±3.2	210.5±4.2	851.3±1.8	2.087±0.022	25.46±0.27	377000±23000	354000±28000	2310±180	3600±1200
D13	D13(3)	180.4±3.6	233.1±4.7	755.1±2.2	1.979±0.021	24.31±0.26	399000±28000	375000±33000	2180±210	3400±1100
D14	D14(1)	291.2±5.8	299.1±6.0	1022.3±1.6	2.691±0.014	41.60±0.21	–	–	–	–
	D14(2)	282.0±5.6	282.1±5.7	1016.1±2.3	2.634±0.014	41.82±0.21	–	–	–	–
J5	J5(1)	1310±26	411.7±8.2	946.8±1.7	2.0688±0.0067	104.48±0.27	284100±3300	278400±4500	2078±27	2270±130
	J5(2)	1383±28	336.9±6.8	1031.87±0.62	2.1567±0.0078	140.58±0.54	277700±3300	273500±4000	2233±25	2390±110
	J5(3)	1238±25	285.7±5.7	1032.3±1.5	2.1597±0.0059	148.57±0.32	278700±2600	274700±3300	2242±21	2393±99

Table A2 continued from previous page

Samp. ID	Rep. ID	^{238}U (ng/g)	^{232}Th (ng/g)	$\delta^{234}U_m$ (‰)	[^{230}Th/^{238}U] (activity)	^{230}Th/^{232}Th (atomic ppm)	Date Uncorr. (years BP)	Date Corr. (years BP)	$\delta^{234}U_{initial}$ (‰)	$\delta^{234}U_{iec}$ (‰)
	J5(4)	1518±30	473.5±9.5	997.5±1.4	2.1404±0.0054	108.97±0.22	289000±2700	283500±3900	2221±25	2430±130
J6	J6(1)	1110±22	348.2±7.0	1019.0±1.9	2.1544±0.0089	109.03±0.40	283400±4100	278000±5000	2234±32	2440±140
	J6(2)	1247±25	402.2±8.0	1021.0±1.2	2.1230±0.0057	104.53±0.24	269000±2400	263300±3800	2147±23	2350±130
	J6(3)	1248±25	416.3±8.3	1010.8±1.6	2.1089±0.0061	100.38±0.25	268200±2600	262200±4100	2119±25	2330±140
J7	J7(1)	2526±51	383.5±7.7	1027.16±0.86	2.1421±0.0041	224.01±0.27	273900±1800	271200±2200	2209±14	2305±62
	J7(2)	2408±48	396.1±7.9	1027.4±1.1	2.1816±0.0047	210.61±0.33	291300±2300	288500±2700	2320±18	2429±72
J10	J10(2)	1798±36	2117±42	789.80±0.77	1.977±0.016	26.66±0.21	350000±14000	327000±20000	1990±110	2930±800
K1	K1(1)	659±13	654±13	571.8±1.4	1.798±0.014	28.76±0.23	568000±84000	552000±87000	2720±710	3700±2100
A5	A5(1)	2260±45	1479±30	737.1±1.3	1.938±0.013	47.01±0.31	379000±14000	366000±16000	2073±96	2520±380
	A5(2)	2464±49	1513±30	764.48±0.95	1.876±0.010	48.50±0.25	299600±6300	286600±9500	1717±46	2060±260
A6	A6(2)	2442±49	1117±22	812.2±1.9	1.9609±0.0081	68.09±0.28	316300±5600	307400±7400	1935±41	2210±200
	A6(3)	2376±48	1086±22	825.1±1.3	2.0697±0.0083	71.91±0.27	396800±9900	389000±11000	2477±76	2830±280
	A6(4)	2737±55	1227±25	820.6±2.2	1.9575±0.0087	69.31±0.28	307400±5600	298600±7300	1907±40	2170±190
F13	F13(1)	339.3±6.8	308.3±6.2	380.6±2.0	1.499±0.013	26.20±0.22	442000±36000	417000±40000	1240±150	1640±500
	F13(2)	339.2±6.8	265.6±5.3	467.8±2.6	1.606±0.015	32.57±0.30	417000±31000	398000±34000	1440±140	1830±460
	F13(3)	342.1±6.8	278.5±5.6	469.4±1.7	1.611±0.014	31.41±0.26	422000±29000	403000±32000	1460±140	1880±460
	F13(4)	330.7±6.6	260.6±5.2	472.6±1.8	1.621±0.013	32.66±0.27	434000±30000	415000±33000	1530±150	1940±480
B2	B2(1)	516±10	615±12	416.5±2.1	1.565±0.017	20.84±0.22	494000±68000	465000±75000	1550±340	2300±1200
G13	G13(1)	728±15	166.4±3.3	428.3±1.8	1.5828±0.0049	109.95±0.31	501000±22000	496000±22000	1740±110	1850±240
	G13(2)	727±15	163.0±3.3	426.5±2.1	1.5877±0.0052	112.52±0.32	533000±30000	528000±30000	1900±160	2020±360
	G13(3)	742±15	155.6±3.1	445.6±5.7	1.640±0.010	124.22±0.68	–	–	–	–
	G13(4)	737±15	153.6±3.1	445.3±2.1	1.6200±0.0082	123.40±0.60	566000±56000	563000±56000	2180±360	2310±770
G14	G14(1)	3066±61	211.1±4.2	465.4±1.8	1.6273±0.0046	375.25±0.92	477000±16000	476000±16000	1784±84	1820±170
	G14(2)	3101±62	201.0±4.0	463.2±1.0	1.6290±0.0037	399.07±0.58	493000±14000	492000±14000	1855±73	1890±150
H6	H6(1)	1115±22	918±18	364.6±1.7	1.648±0.016	31.79±0.30	–	–	–	–
	H6(2)	1288±26	891±18	378.4±2.9	1.523±0.012	34.95±0.27	547000±82000	532000±85000	1700±430	2100±1100
	H6(3)	1161±23	852±17	380.1±1.6	1.531±0.012	33.11±0.25	580000±110000	570000±120000	1900±690	2400±1700
H7	H7(1)	893±18	565±11	404.74±0.75	1.607±0.012	40.31±0.30	–	–	–	–
	H7(2)	1003±20	597±12	413.5±1.5	1.551±0.010	41.34±0.26	463000±31000	449000±33000	1470±140	1750±390
	H7(3)	988±20	675±14	405.4±1.7	1.541±0.011	35.85±0.26	466000±37000	449000±39000	1440±160	1770±460
	H7(4)	989±20	589±12	412.8±2.2	1.5452±0.0099	41.20±0.26	448000±28000	434000±30000	1400±120	1680±350
B14	B14(1)	1676±34	739±15	410.00±0.93	1.5156±0.0067	54.60±0.24	392000±12000	380000±14000	1200±47	1360±160
	B14(2)	1664±33	614±12	433.5±1.1	1.5425±0.0064	66.35±0.26	385000±11000	375000±12000	1251±43	1390±130
	B14(3)	1669±33	727±15	413.2±2.8	1.557±0.015	56.78±0.54	482000±57000	472000±58000	1570±270	1780±620
	B14(4)	1730±35	712±14	411.5±4.2	1.480±0.014	57.15±0.53	338000±18000	327000±19000	1035±58	1170±160
B15	B15(1)	476.9±9.5	155.4±3.1	373.5±1.9	1.4102±0.0058	68.70±0.30	314300±6400	304400±8300	882±21	968±82
	B15(2)	481.5±9.6	171.7±3.4	375.8±2.1	1.4136±0.0061	62.94±0.27	314700±6900	303900±9000	886±23	982±91
	B15(3)	471.0±9.4	149.8±3.0	375.3±3.6	1.416±0.011	70.72±0.55	318000±13000	309000±14000	897±37	980±100
	B15(4)	488.2±9.8	167.1±3.4	367.4±4.3	1.400±0.015	64.94±0.62	311000±16000	301000±17000	859±43	950±120
C1	C1(1)	1628±33	442.8±8.9	375.2±3.3	1.5121±0.0058	88.27±0.30	513000±35000	507000±35000	1570±160	1700±360
	C1(2)	1582±32	431.3±8.6	374.6±1.4	1.5083±0.0048	87.83±0.25	500000±22000	494000±23000	1509±98	1630±230

Table A2 continued from previous page

Samp. ID	Rep. ID	^{238}U (ng/g)	^{232}Th (ng/g)	$\delta^{234}U_m$ (‰)	[^{230}Th/^{238}U] (activity)	^{230}Th/^{232}Th (atomic ppm)	Date Uncorr. (years BP)	Date Corr. (years BP)	$\delta^{234}U_{initial}$ (‰)	$\delta^{234}U_{iec}$ (‰)
	C1(3)	865±17	276.2±5.5	385.3±5.4	1.389±0.012	69.06±0.55	282000±11000	272000±12000	831±31	911±93
	C1(4)	839±17	177.9±3.6	383.8±4.9	1.3509±0.0089	101.12±0.62	256700±6800	249900±7700	777±20	825±58
C3	C3(2)	3557±71	687±14	372.94±0.95	1.5058±0.0059	123.71±0.48	499000±26000	495000±26000	1510±110	1590±240
	C3(3)	3460±69	659±13	375.8±2.5	1.5228±0.0045	126.96±0.27	569000±40000	566000±41000	1850±220	1960±470
C6	C6(1)	361.3±7.2	422.6±8.5	258.6±2.8	1.346±0.016	18.27±0.22	490000±92000	450000±100000	930±280	1360±920
C10	C10(1)	381.9±7.6	267.9±5.4	414.3±1.6	1.525±0.010	34.51±0.22	398000±19000	379000±23000	1208±79	1490±290
	C10(2)	382.6±7.7	256.7±5.2	518.2±3.8	1.659±0.012	39.25±0.29	391000±21000	376000±23000	1497±100	1830±340
	C10(3)	379.9±7.6	218.5±4.4	515.5±1.9	1.6498±0.0099	45.53±0.27	384000±15000	370000±17000	1465±71	1740±250
	C10(4)	404.4±8.1	271.5±5.5	443.1±1.5	1.552±0.011	36.70±0.27	380000±18000	362000±21000	1232±74	1510±270
	C10(5)	431.3±8.6	277.9±5.6	427.2±1.6	1.530±0.011	37.71±0.27	378000±18000	361000±21000	1184±70	1440±250
	C10(6)	431.7±8.6	295.1±5.9	434.9±1.9	1.555±0.012	36.13±0.27	404000±23000	387000±25000	1296±94	1590±320
	C10(7)	482.6±9.7	325.0±6.5	433.1±2.6	1.528±0.012	36.02±0.28	363000±17000	345000±20000	1147±67	1400±250
	C10(8)	443.3±8.9	290.6±5.8	436.4±1.4	1.519±0.011	36.80±0.27	347000±14000	329000±17000	1104±55	1340±230
C11	C11(1)	1781±36	346.6±6.9	467.3±1.1	1.6278±0.0045	132.84±0.32	471000±14000	467000±14000	1747±71	1850±160
	C11(2)	1746±35	331.6±6.7	472.91±0.98	1.6480±0.0063	137.73±0.54	514000±26000	510000±26000	2000±150	2110±330
C13	C13(1)	1229±25	387.3±7.8	321.3±1.9	1.3946±0.0052	70.28±0.24	385000±11000	376000±12000	928±33	1015±98
	C13(2)	1281±26	378.0±7.6	322.1±1.5	1.3899±0.0048	74.77±0.22	374300±9000	366000±10000	904±27	983±84
	C13(3)	1214±24	322.1±6.5	341.3±2.6	1.4390±0.0098	86.11±0.58	424000±26000	417000±27000	1106±86	1190±190
	C13(4)	1180±24	334.8±6.7	336.1±3.6	1.434±0.011	80.24±0.59	429000±31000	421000±32000	1100±100	1200±230
C14	C14(1)	2133±43	516±10	367.09±0.91	1.5908±0.0047	104.35±0.25	–	–	–	–
	C14(2)	2136±43	533±11	361.7±1.2	1.5855±0.0049	100.87±0.26	–	–	–	–

Table A3: Average values of various U-Th data for each sample from the PLJ-1 core, calculated from replicate analyses. Samples that passed all threshold criteria (Section 5) are listed first; then all samples are sorted by depth (**CCLF**). All uncertainties listed are 2-σ. **N** is the total number of replicate analyses made for each sample. **MSWD** and **Prob. of Fit** fields are left blank if there is only 1 replicate analysis or marked with an asterisk (*) if any replicate analyses yielded infinite dates; samples marked with an * are considered to have failed the reproducibility criterion. **Weighted Mean Date** is reported relative to Before Present (BP), in which the present is defined as January 1, 1950. $\boldsymbol{\delta^{234}U_m}$ is the measured $\delta^{234}U$. Meaning of the abbreviations used for **facies** can be found in Section 3. For **Threshold Criteria Result**, numbers indicate which threshold criterion each sample failed: 1 = $^{238}U/^{232}Th$; 2 = reproducibility; and 3 = $\delta^{234}U_{iec}$. See Table A2 for data associated with replicate analyses and Supplementary Materials for raw unrounded data.

Samp. ID	CCLF (m)	N	^{238}U (ng/g)	^{232}Th (ng/g)	MSWD	Prob. of Fit	Weighted Mean Date (yrs BP)	$[^{230}Th/^{238}U]$ (activity)	$\delta^{234}U_m$ (‰)	$\delta^{234}U_{iec}$ (‰)	$^{238}U/^{232}Th$ (atomic)	$^{230}Th/^{232}Th$ (atomic ppm)	Facies	Threshold Crit. Result
Samples Passing Threshold Criteria														
F9	1.080	3	2910±140	124±50	0.07	0.93	1810±200	0.0760±0.0054	2355.0±3.3	2395±19	24.1±9.2	28.9±9.0	–	pass
F14	3.530	4	700±120	25±11	1.38	0.25	8180±150	0.282±0.012	2639±22	2727±30	29±10	127±41	–	pass
F15	3.850	3	980±63	105±25	0.11	0.90	9590±450	0.366±0.015	2721±49	2880±53	9.4±1.8	54.5±8.6	–	pass
F16	4.330	2	1150±300	250±280	0.87	0.35	10500±980	0.425±0.015	2630±240	2880±130	5.2±4.5	35±29	–	pass
C16	4.660	3	1580±490	243±65	0.17	0.84	12920±790	0.418±0.018	2085.3±5.1	2257±59	6.51±0.36	43.20±0.92	–	pass
D4	4.880	4	1970±140	497±36	0.03	0.99	13200±1200	0.4502±0.0092	1934±12	2156±95	3.97±0.11	28.34±0.76	–	pass
K16	20.806	5	2600±1400	1430±700	0.11	0.98	69100±2400	1.512±0.018	1745±40	2490±260	1.824±0.094	43.8±2.0	CP1	pass
L1	20.823	5	2600±1100	1300±770	2.77	0.03	70500±3500	1.54±0.13	1774.7±6.7	2500±260	2.04±0.28	49.6±3.4	CP1	pass
D6	33.839	5	1200±220	1000±320	2.06	0.08	184300±5800	2.18±0.15	1290±150	2800±520	1.21±0.19	41.9±9.3	CP2	pass
M1	45.599	4	2520±83	430±45	3.05	0.03	322700±3100	2.130±0.012	936.0±3.8	2440±85	5.87±0.42	199±15	CP1	pass
M3	45.660	5	1740±260	376±49	0.49	0.75	322600±2000	2.212±0.015	1000±16	2650±160	4.63±0.41	163±15	CP1	pass
J8	45.686	3	2660±210	341±68	0.79	0.46	317500±1700	2.1828±0.0079	985.3±9.6	2501±68	7.83±0.91	271±32	CP1	pass
J9	45.741	3	3059±61	1179±41	0.59	0.56	311200±3300	1.958±0.012	807.5±6.3	2170±160	2.594±0.085	80.7±3.2	CP1	pass
E12	55.318	5	953±79	940±210	1.26	0.28	416000±20000	1.83±0.11	631±62	2700±1100	1.02±0.15	29.5±6.1	CP2	pass
F4	55.587	5	1090±160	120.0±7.2	3.32	0.01	391300±5500	2.0570±0.0094	816.9±8.3	2550±130	9.10±0.81	297±27	CP2	pass
B5	70.941	5	1699±34	364±35	1.00	0.41	514000±14000	1.6727±0.0098	489.7±5.9	2230±610	4.68±0.40	124±11	CMC	pass
B11	71.182	4	2650±350	353±67	1.70	0.16	554000±19000	1.616±0.016	443.9±8.3	2190±400	7.52±0.57	193±15	RGA	pass
B13	71.190	4	1320±170	134±26	1.69	0.17	575000±22000	1.6572±0.0059	469.5±4.9	2600±1300	9.88±0.82	260±21	RGA	pass
Samples Failing Threshold Criteria														
P10	6.505	2	749±66	840±100	*	*	–	0.540±0.013	792.8±4.5	–	0.896±0.033	7.68±0.44	CP2	1,2
L3	21.649	1	619±12	1118±23	–	–	152000±47000	1.621±0.025	719.6±3.0	2200±1300	0.553±0.028	14.25±0.22	CMC	1
G1	21.725	1	851±17	1230±130	–	–	67000±46000	1.19±0.12	673.8±2.0	1340±660	0.69±0.11	13.1±1.9	CMC	1
G2	21.878	2	1164±23	1440±140	0.01	0.92	82000±11000	1.700±0.054	1497±23	2840±860	0.812±0.074	21.9±1.3	CMC	1
G5	22.364	1	635±13	1395±28	–	–	275000±43000	2.162±0.040	966.7±1.7	5200±4200	0.455±0.028	15.61±0.29	CMC	1
G6	22.367	4	350±120	690±160	0.04	0.99	149000±12000	2.40±0.66	1580±720	5300±4600	0.506±0.071	19.2±3.8	CMC	1
G7	22.486	3	418±15	829±21	0.05	0.96	140000±25000	1.794±0.066	932±42	3000±2200	0.504±0.028	14.36±0.22	CMC	1
G8	22.537	1	861±17	2362±48	–	–	–	1.986±0.035	621.9±3.9	–	0.365±0.028	11.50±0.20	CMC	1
M15	23.467	4	323±13	38.3±5.9	36.97	0.00	102200±2800	2.219±0.086	2303±14	3175±65	8.5±1.2	298±45	CP2	2
L7	24.105	7	6800±660	400±53	399.36	0.00	106100±4800	1.83±0.15	1687.6±7.5	2316±94	17.0±1.4	494±48	CMC	2
D7	33.954	2	838±36	997±91	0.24	0.63	203700±9100	2.331±0.024	1328±50	3500±940	0.840±0.041	31.1±1.8	CP2	1
D11	35.671	2	392±77	870±420	*	*	–	1.41±0.23	284±15	–	0.46±0.13	10.2±1.3	CMC	1,2
D12	35.673	2	262±93	440±44	*	*	424000±46000	2.080±0.024	806.1±1.5	4400±1900	0.60±0.27	19±12	CMC	1,2

Table A3 continued from previous page

Samp. ID	CCLF (m)	N	^{238}U (ng/g)	^{232}Th (ng/g)	MSWD	Prob. of Fit	Weighted Mean Date (yrs BP)	[^{230}Th/^{238}U] (activity)	$\delta^{234}U_m$ (‰)	$\delta^{234}U_{iec}$ (‰)	^{238}U/ ^{232}Th (atomic)	^{230}Th/^{232}Th (atomic ppm)	Facies	Threshold Crit. Result
D13	35.705	3	168±22	216±30	8.19	0.00	383000±53000	2.08±0.19	820±120	3900±1600	0.778±0.028	25.7±2.9	CMC	1,2
D14	35.733	2	287±13	291±24	0.00	0.00	–	2.663±0.080	1019.2±8.9	–	0.987±0.037	41.71±0.31	CMC	1,2
J5	45.640	4	1360±240	380±170	5.51	0.00	277400±4500	2.131±0.085	1002±81	2370±140	3.7±1.2	126±44	CP1	2
J6	45.661	3	1200±160	389±72	14.04	0.00	266500±9100	2.129±0.047	1017±11	2380±140	3.10±0.19	104.6±8.7	CP1	2
J7	45.683	2	2470±170	390±18	97.16	0.00	278000±17000	2.162±0.056	1027.3±1.1	2370±180	6.33±0.72	217±19	CP1	2
J10	45.921	1	1798±36	2117±42	–	–	327000±20000	1.977±0.016	789.80±0.77	2930±800	0.849±0.028	26.66±0.21	CP2	1
K1	54.873	1	659±13	654±13	–	–	552000±87000	1.798±0.014	571.8±1.4	3700±2100	1.000±0.028	28.76±0.23	CMC	1
A5	55.288	2	2360±290	1496±49	72.60	0.00	307000±70000	1.907±0.088	751±39	2290±650	1.58±0.14	47.8±2.1	CP2	2
A6	55.292	3	2520±390	1140±150	105.25	0.00	319000±48000	2.00±0.13	819±13	2400±740	2.202±0.049	69.8±3.9	CP2	2
F13	67.741	4	337.8±9.8	278±43	0.29	0.84	408000±17000	1.58±0.11	448±89	1820±500	1.22±0.16	30.7±6.1	CP2	3
B2	70.741	1	516±10	615±12	–	–	465000±75000	1.565±0.017	416.5±2.1	2300±1200	0.839±0.028	20.84±0.22	CMC	1
G13	71.394	4	734±15	160±12	*	*	512000±17000	1.597±0.040	433±21	2060±770	4.60±0.43	118±15	RGA	2
G14	71.679	2	3084±62	206±14	2.11	0.15	485000±15000	1.6282±0.0046	464.3±3.1	1850±170	15.0±1.3	387±34	RGA	3
H6	72.406	3	1190±180	887±66	*	*	545000±69000	1.527±0.012	379.2±2.9	2200±1700	1.34±0.23	33.3±3.2	RGA	2
H7	72.409	4	970±100	607±95	*	*	443000±19000	1.546±0.011	410.5±9.0	1730±460	1.60±0.20	39.7±5.2	RGA	2
B14	73.327	4	1685±61	700±110	12.05	0.00	370000±28000	1.524±0.068	417±22	1420±620	2.43±0.40	59±10	RGA	2
B15	73.566	4	479±15	161±20	0.19	0.90	304600±5300	1.410±0.015	373.0±7.7	970±120	2.98±0.30	66.8±7.1	RGA	3
C1	73.573	4	1230±870	330±260	195.37	0.00	281000±85000	1.44±0.16	380±11	1270±920	3.8±1.3	87±26	RGA	2
C3	73.704	2	3510±140	673±40	8.62	0.00	515000±64000	1.514±0.024	374.4±4.0	1770±520	5.21±0.11	125.3±4.6	RGA	2
C6	74.222	1	361.3±7.2	422.6±8.5	–	–	450000±100000	1.346±0.016	258.6±2.8	1360±920	0.855±0.028	18.27±0.22	CMC	1
C10	74.444	8	417±73	275±62	3.69	0.00	361000±14000	1.56±0.11	453±81	1540±340	1.52±0.19	37.8±6.8	CMC	2
C11	74.529	2	1763±50	339±21	8.18	0.00	477000±36000	1.638±0.028	470.1±8.0	1980±370	5.20±0.18	135.3±6.9	CMC	2
C13	74.739	4	1226±84	356±64	7.11	0.00	376000±20000	1.414±0.051	330±20	1100±230	3.46±0.50	78±14	RGA	2
C14	74.851	2	2135±43	525±24	*	*	–	1.5881±0.0075	364.4±7.6	–	4.07±0.18	102.6±4.9	RGA	2

References

Ainsworth, N.R., Burnett, R.D., Kontrovitz, M., 1990. Ostracod colour change by thermal alteration, offshore Ireland and Western UK. Marine and Petroleum Geology 7, 288–297. doi:10.1016/0264-8172(90)90006-3.

Alam, M.S., Cheng, T., 2014. Uranium release from sediment to groundwater: Influence of water chemistry and insights into release mechanisms. Journal of Contaminant Hydrology 164, 72–87. doi:10.1016/j.jconhyd.2014.06.001.

Ames, L.L., McGarrah, J.E., Walker, B.A., 1983a. Sorption of trace constituents from aqueous solutions onto secondary minerals. I. Uranium. Clays and Clay Minerals 31, 321–334. doi:10.1346/CCMN.1983.0310501.

Ames, L.L., McGarrah, J.E., Walker, B.A., 1983b. Sorption of Uranium and Radium by Biotite, Muscovite, and Phlogopite. Clays and Clay Minerals 31, 343–351. doi:10.1346/CCMN.1983.0310503.

Ames, L.L., McGarrah, J.E., Walker, B.A., Salter, P.F., 1983c. Uranium and radium sorption on amorphous ferric oxyhydroxide. Chemical Geology 40, 135–148. doi:10.1016/0009-2541(83)90095-5.

Balch, D.P., Cohen, A.S., Schnurrenberger, D.W., Haskell, B.J., Valero-Garcés, B.L., Beck, J.W., Cheng, H., Edwards, R.L., 2005. Ecosystem and paleohydrological response to Quaternary climate change in the Bonneville Basin, Utah. Palaeogeography, Palaeoclimatology, Palaeoecology 221, 99–122. doi:10.1016/j.palaeo.2005.01.013.

Balsam, W.L., Deaton, B.C., Damuth, J.E., 1999. Evaluating optical lightness as a proxy for carbonate content in marine sediment cores. Marine Geology 161, 141–153. doi:10.1016/S0025-3227(99)00037-7.

Bar-Matthews, M., Ayalon, A., Gilmour, M., Matthews, A., Hawkesworth, C.J., 2003. Sea-land oxygen isotope relationships from planktonic foraminifera and speleothems in the Eastern Mediterranean region and their implication for paleorainfall during interglacial intervals. Geochimica et Cosmochimica Acta 67, 3181–3199. doi:10.1016/S0016-7037(02)01031-1.

Bard, E., Fairbanks, R.G., Hamelin, B., Zindler, A., Chi Track Hoang, 1991. Uranium-234 anomalies in corals older than 150,000 years. Geochimica et Cosmochimica Acta 55, 2385–2390. doi:10.1016/0016-7037(91)90115-L.

Bateman, H., 1910. The solution of a system of differential equations occurring in the theory of radio-active transformations. Proc. Cambridge Phil. Soc. 15, 423–427. doi:10.1112/plms/s2-8.1.469.

Bischoff, J.L., Fitzpatrick, J.a., 1991. U-series dating of impure carbonates: An isochron technique using total-sample dissolution. Geochimica et Cosmochimica Acta 55, 543–554. doi:10.1016/0016-7037(91)90011-S.

Bischoff, J.L., Rosenbauer, R.J., Smith, G.I., 1985. Uranium-Series Dating of Sediments from Searles Lake: Differences Between Continental and Marine Climate Records. Science 227, 1222–1224. doi:10.1126/science.227.4691.1222.

Blaauw, M., Christen, J.A., 2011. Flexible paleoclimate age-depth models using an autoregressive gamma process. Bayesian Analysis 6, 457–474. doi:10.1214/11-BA618.

Blanchard, R.L., Cheng, M.H., Potratz, H.A., 1967. Uranium and Thorium Series Disequilibria in Recent and Fossil Marine Molluscan Shells. Journal of Geophysical Research 72, 4745–4757.

Bobst, A.L., Lowenstein, T.K., Jordan, T.E., Godfrey, L.V., Ku, T.L., Luo, S., 2001. A 106 ka paleoclimate record from drill core of the Salar de Atacama, northern Chile. Palaeogeography, Palaeoclimatology, Palaeoecology 173, 21–42. doi:10.1016/S0031-0182(01)00308-X.

Bone, S.E., Dynes, J.J., Cliff, J., Bargar, J.R., 2017. Uranium(IV) adsorption by natural organic matter in anoxic sediments. Proceedings of the National Academy of Sciences 114, 201611918. doi:10.1073/pnas.1611918114.

Bourdon, B., Henderson, G.M., Lundstrom, C.C., Turner, S.P. (Eds.), 2003. Uranium-Series Geochemistry. volume 52. Mineralogical Society of America.

Brand, A., Allen, L., Altman, M., Hlava, M., Scott, J., 2015. Beyond authorship: attribution, contribution, collaboration, and credit. Learned Publishing 28, 151–155. doi:10.1087/20150211.

Broecker, W.S., 1963. A Preliminary Evaluation of Uranium Series Inequilibrium as a Tool for Absolute Age Measurement on Marine Carbonates. Journal of Geophysical Research 68, 2817–2834. doi:10.1029/JZ068i009p02817.

Carolin, S.A., Cobb, K.M., Adkins, J.F., Clark, B., Conroy, J.L., Lejau, S., Malang, J., Tuen, A.A., 2013. Varied response of western Pacific hydrology to climate forcings over the last glacial period. Science 340, 1564–1566. doi:10.1126/science.1233797.

Chabaux, F., Bourdon, B., Riotte, J., 2008. Chapter 3 U-Series Geochemistry in Weathering Profiles, River Waters and Lakes, in: Radioactivity in the Environment. volume 13, pp. 49–104. doi:10.1016/S1569-4860(07)00003-4.

Chabaux, F., Riotte, J., Dequincey, O., 2003. U-Th-Ra Fractionation During Weathering and River Transport. Reviews in Mineralogy and Geochemistry 52, 533–576. doi:10.2113/0520533.

Chappaz, A., Gobeil, C., Tessier, A., 2010. Controls on uranium distribution in lake sediments. Geochimica et Cosmochimica Acta 74, 203–214. doi:10.1016/j.gca.2009.09.026.

Cheng, H., Adkins, J., Edwards, R., Boyle, E.A., 2000. U-Th dating of deep-sea corals. Geochimica et Cosmochimica Acta 64, 2401–2416. doi:10.1016/S0016-7037(99)00422-6.

Cheng, H., Edwards, R.L., Sinha, A., Spötl, C., Yi, L., Chen, S., Kelly, M., Kathayat, G., Wang, X., Li, X., Kong, X., Wang, Y., Ning, Y., Zhang, H., 2016. The Asian monsoon over the past 640,000 years and ice age terminations. Nature 534, 640–646. doi:10.1038/nature18591.

Cheng, H., Lawrence Edwards, R., Shen, C.C., Polyak, V.J., Asmerom, Y., Woodhead, J., Hellstrom, J., Wang, Y., Kong, X., Spötl, C., Wang, X., Calvin Alexander, E., 2013. Improvements in 230Th dating, 230Th and 234U half-life values, and U-Th isotopic measurements by multi-collector inductively coupled plasma mass spectrometry. Earth and Planetary Science Letters 371-372, 82–91. doi:10.1016/j.epsl.2013.04.006.

Cobbing, E.J., Pitcher, W.S., WIlson, J.J., Baldock, J.W., Taylor, W.P., McCourt, W., Snelling, N.J., 1981. The geology of the Western Cordillera of northern Peru. volume 5. Great Britain Institute of Geological Sciences, Natural Environmental Research Council.

Colman, S., Kaufman, D., Bright, J., Heil, C., King, J., Dean, W., Rosenbaum, J., Forester, R., Bischoff, J., Perkins, M., McGeehin, J., 2006. Age model for a continuous, ca 250-ka Quaternary lacustrine record from Bear Lake, Utah–Idaho. Quaternary Science Reviews 25, 2271–2282. doi:10.1016/j.quascirev.2005.10.015.

Colman, S.M., 1996. Continental Drilling for Paleoclimatic Records: Recommendations from an International Workshop. Technical Report. GeoForschungsZentrum. Potsdam, Germany.

Durand, S., Chabaux, F., Rihs, S., Duringer, P., Elsass, P., 2005. U isotope ratios as tracers of groundwater inputs into surface waters: example of the Upper Rhine hydrosystem. Chemical Geology 220, 1–19.

Dutton, A., Rubin, K., McLean, N., Bowring, J., Bard, E., Edwards, R.L., Henderson, G.M., Reid, M.R., Richards, D.A., Sims, K., Walker, J.D., Yokoyama, Y., 2017. Data reporting standards for publication of U-series data for geochronology and timescale assessment in the earth sciences. Quaternary Geochronology 39, 142–149. doi:10.1016/j.quageo.2017.03.001.

Edwards, R., Gallup, C., Cheng, H., 2003. Uranium-series Dating of Marine and Lacustrine Carbonates. Reviews in Mineralogy and Geochemistry 52, 363–405. doi:10.2113/0520363.

Edwards, R.L., 1988. High Precition Thorium-230 Ages of Corals and the Timing of Sea Level Fluctuations in the Late Quaternary. Ph.D. thesis. California Insititute of Technology.

Edwards, R.L., Chen, J., Wasserburg, G., 1987. 238U-234U-230Th-232Th systematics and the precise measurement of time over the past 500,000 years. Earth and Planetary Science Letters 81, 175–192. doi:10.1016/0012-821X(87)90154-3.

Fleischer, R.L., 1982. Alpha-recoil damage and solution effects in minerals: uranium isotopic disequilibrium and radon release. Geochimica et Cosmochimica Acta 46, 2191–2201. doi:10.1016/0016-7037(82)90194-6.

Flusche, M.A., Seltzer, G., Rodbell, D., Siegel, D., Samson, S., 2005. Constraining water sources and hydrologic processes from the isotopic analysis of water and dissolved strontium, Lake Junin, Peru. Journal of Hydrology 312, 1–13. doi:10.1016/j.jhydrol.2005.02.021.

Francke, A., Wagner, B., Just, J., Leicher, N., Gromig, R., Baumgarten, H., Vogel, H., Lacey, J.H., Sadori, L., Wonik, T., Leng, M.J., Zanchetta, G., Sulpizio, R., Giaccio, B., 2016. Sedimentological processes and environmental variability at Lake Ohrid (Macedonia, Albania) between 637 ka and the present. Biogeosciences 13, 1179–1196. doi:10.5194/bg-13-1179-2016.

Frechen, M., Sierralta, M., Oezen, D., Urban, B., 2007. Uranium-series dating of peat from central and Northern Europe, in: Sirocko, F., Claussen, M., Goñi, M.F.S., Litt, T. (Eds.), Developments in Quaternary Science: The Climate of Past Interglacials. Elsevier. volume 7. chapter 8, pp. 83–117. doi:10.1016/S1571-0866(07)80033-9.

Fritz, S.C., Baker, P.a., Lowenstein, T.K., Seltzer, G.O., Rigsby, C.a., Dwyer, G.S., Tapia, P.M., Arnold, K.K., Ku, T.L., Luo, S., 2004. Hydrologic variation during the last 170,000 years in the southern hemisphere tropics of South America. Quaternary Research 61, 95–104. doi:10.1016/j.yqres.2003.08.007.

Fritz, S.C., Baker, P.A., Seltzer, G.O., Ballantyne, A., Tapia, P., Cheng, H., Edwards, R.L., 2007. Quaternary glaciation and hydrologic variation in the South American tropics as reconstructed from the Lake Titicaca drilling project. Quaternary Research 68, 410–420. doi:10.1016/j.yqres.2007.07.008.

Gallup, C.D., Edwards, R.L., Johnson, R.G., 1994. The timing of high sea levels over the past 200,000 years. Science 263, 796–800. doi:10.1126/science.263.5148.796.

Geyh, M.A., Mu, H., 2005. Numerical 230Th/U dating and a palynological review of the Holsteinian/Hoxnian Interglacial. Quaternary Science Reviews 24, 1861–1872. doi:10.1016/j.quascirev.2005.01.007.

Giosan, L., Flood, R.D., Aller, R.C., 2002. Paleoceanographic significance of sediment color on western North Atlantic drifts: I. Origin of color. Marine Geology 189, 25–41. doi:10.1016/S0025-3227(02)00321-3.

Groot, M.H.M., Bogotá, R.G., Lourens, L.J., Hooghiemstra, H., Vriend, M., Berrio, J.C., Tuenter, E., Van Der Plicht, J., Van Geel, B., Ziegler, M., Weber, S.L., Betancourt, A., Contreras, L., Gaviria, S., Giraldo, C., González, N., Jansen, J.H.F., Konert, M., Ortega, D., Rangel, O., Sarmiento, G., Vandenberghe, J., Van Der Hammen, T., Van Der Linden, M., Westerhoff, W., 2011. Ultra-high resolution pollen record from the northern Andes reveals rapid shifts in montane climates within the last two glacial cycles. Climate of the Past 7, 299–316. doi:10.5194/cp-7-299-2011.

Grzymko, T.J., Marcantonio, F., McKee, B.A., Mike Stewart, C., 2007. Temporal variability of uranium concentrations and 234U/238U activity ratios in the Mississippi river and its tributaries. Chemical Geology 243, 344–356. doi:10.1016/j.chemgeo.2007.05.024.

Haase-Schramm, A., Goldstein, S.L., Stein, M., 2004. U-Th dating of Lake Lisan (late Pleistocene dead sea) aragonite and implications for glacial east Mediterranean climate change. Geochimica et Cosmochimica Acta 68, 985–1005. doi:10.1016/j.gca.2003.07.016.

Hamelin, B., Bard, E., Zindler, A., Fairbanks, R.G., 1991. 234U/238U mass spectrometry of corals: How accurate is the UTh age of the last interglacial period? Earth and Planetary Science Letters 106, 169–180. doi:10.1016/0012-821X(91)90070-X.

Hansen, B.C.S., Wright, H.E., Bradbury, J.P., 1984. Pollen studies in the Junín area, central Peruvian Andes. Geological Society of America Bulletin 95, 1454. doi:10.1130/0016-7606(1984)95<1454:PSITJA>2.0.CO;2.

Hatfield, R., Stoner, J., Solada, K.E., Morey, A.E., Woods, A., Chen, C.Y., McGee, D., Abbott, M.B., Rodbell, D.T., 2020a. Paleomagnetic Constraint of the Brunhes Age Sedimentary Record from Lake Junín, Peru. Frontiers in Earth Science 8. doi:10.3389/feart.2020.00147.

Hatfield, R., Woods, A., Lehmann, S., Weidhaas, N., Chen, C., Kück, J., Pierdominici, S., Stoner, J., Abbott, M., Rodbell, D., 2020b. Stratigraphic correlation and splice generation for sediments recovered from a large-lake drilling project: an example from Lake Junín, Peru. Journal of Paleolimnology 63, 83–100. doi:10.1007/s10933-019-00098-w.

Helmke, J.P., Schulz, M., Bauch, H.A., 2002. Sediment-Color Record from the Northeast Atlantic Reveals Patterns of Millennial-Scale Climate Variability during the Past 500,000 Years. Quaternary Research 57, 49–57. doi:10.1006/qres.2001.2289.

Henderson, G.M., 2002. Seawater (234U/238U) during the last 800 thousand years. Earth and Planetary Science Letters 199, 97–110. doi:10.1016/S0012-821X(02)00556-3.

Henderson, G.M., Anderson, R.F., 2003. The U-series Toolbox for Paleoceanography. Reviews in Mineralogy and Geochemistry 52, 493–531. doi:10.2113/0520493.

Henderson, G.M., Robinson, L.F., Cox, K., Thomas, A.L., 2006. Recognition of non-Milankovitch sea-level highstands at 185 and 343 thousand years ago from U-Th dating of Bahamas sediment. Quaternary Science Reviews 25, 3346–3358. doi:10.1016/j.quascirev.2006.03.003.

Holmes, J., 1998. The palaeoenvironmental significance of iron and manganese in non-marine ostracod shells: a preliminary analysis. Kingston University School of Geography. chapter 10. pp. 198–212.

Holmes, J.A., Chivas, A.R., 2002. Ostracod shell chemistry - overview. Geophysical Monograph Series 131, 185–204. doi:10.1029/131GM10.

Israelson, C., Björck, S., Hawkesworth, C.J., Possnert, G., 1997. Direct U-Th dating of organic- and carbonate-rich lake sediments from southern Scandinavia. Earth and Planetary Science Letters 153, 251–263. doi:10.1016/S0012-821X(97)00184-2.

Ivanovich, M., Harmon, R., 1992. Uranium-series Disequilibrium: Applications to Earth, Marine, and Environmental Sciences. Oxford University Press, New York.

Jaffey, A.H., Flynn, K.F., Glendenin, L.E., Bentley, W.C., Essling, A.M., 1971. Precision measurement of half-lives and specific activities of U235 and U238. Physical Review C 4, 1889–1906. doi:10.1103/PhysRevC.4.1889.

Ji, J., Shen, J., Balsam, W.L., Chen, J., Liu, L., Liu, X., 2005. Asian monsoon oscillations in the northeastern Qinghai–Tibet Plateau since the late glacial as interpreted from visible reflectance of Qinghai Lake sediments. Earth and Planetary Science Letters 233, 61–70. doi:10.1016/j.epsl.2005.02.025.

Karanovic, I., 2012. Recent freshwater ostracods of the world: Crustacea, Ostracoda, Podocopida. Springer.

Kaufman, A., 1971. U-series dating of Dead Sea basin carbonates. Geochimica et Cosmochimica Acta 35, 1269–1281. doi:10.1016/0016-7037(71)90115-3.

Kaufman, A., Broecker, W.S., Ku, T.L., Thurber, D.L., 1971. The status of U-series methods of mollusk dating. Geochimica et Cosmochimica Acta 35, 1155–1183. doi:10.1016/0016-7037(71)90031-7.

Kaufman, A., Yechieli, Y., Gardosh, M., 1992. Reevaluation of the Lake-Sediment Chronology in the Dead-Sea Basin, Israel, Based on New Th-230/U Dates. Quaternary Research 38, 292–304. doi:10.1016/0033-5894(92)90039-L.

Kelly, S.D., Newville, M.G., Cheng, L., Kemner, K.M., Sutton, S.R., Fenter, P., Sturchio, N.C., Spötl, C., 2003. Uranyl Incorporation in Natural Calcite. Environmental Science & Technology 37, 1284–1287. doi:10.1021/es025962f.

Kelly, S.D., Rasbury, E.T., Chattopadhyay, S., Kropf, A.J., Kemner, K.M., 2006. Evidence of a Stable Uranyl Site in Ancient Organic-Rich Calcite. Environmental Science & Technology 40, 2262–2268. doi:10.1021/es051970v.

Kigoshi, K., 1971. Alpha-Recoil Thorium-234: Dissolution into Water and the Uranium-234/Uranium-238 Disequilibrium in Nature. Science 173, 47–48. doi:10.1126/science.173.3991.47.

Kiro, Y., Goldstein, S., Kushnir, Y., Stein, M., Lazar, B., 2018. Droughts and tropical-induced rainfall in the east mediterranean during warm periods, in: Goldschmidt Abstracts.

Kliem, P., Enters, D., Hahn, A., Ohlendorf, C., Lisé-Pronovost, A., St-Onge, G., Wastegård, S., Zolitschka, B., the Pasado Science Team, 2013. Lithology, radiocarbon chronology and sedimentological interpretation of the lacustrine record from Laguna Potrok Aike, southern Patagonia. Quaternary Science Reviews 71, 54–69. doi:10.1016/j.quascirev.2012.07.019.

König, I., Haeckel, M., Drodt, M., Suess, E., Trautwein, A.X., 1999. Reactive Fe(II) layers in deep-sea sediments. Geochimica et Cosmochimica Acta 63, 1517–1526. doi:10.1016/S0016-7037(99)00104-0.

König, I., Lougear, A., Bruns, P., Grützner, J., Trautwein, A., Dullo, W.C., 2000. Iron oxidation in sediment cores (Site 1062) during six months of storage in the Ocean Drilling Program archive. Proceedings of the Ocean Drilling Program, Scientific Results. volume 172. pp. 1–11.

Kronfeld, J., 1974. Uranium deposition and Th-234 alpha-recoil: An explanation for extreme U-234/U-238 fractionation within the Trinity aquifer. Earth and Planetary Science Letters 21, 327–330. doi:10.1016/0012-821X(74)90169-1.

Kronfeld, J., Godfrey-Smith, D., Johannessen, D., Zentilli, M., 2004. Uranium series isotopes in the Avon Valley, Nova Scotia. Journal of Environmental Radioactivity 73, 335–352. doi:10.1016/j.jenvrad.2003.11.002.

Kronfeld, J., Vogel, J.C., 1991. Uranium isotopes in surface waters from southern Africa. Earth and Planetary Science Letters 105, 191–195. doi:10.1016/0012-821X(91)90130-A.

Ku, T.L., Knauss, K.G., Mathieu, G.G., 1977. Uranium in open ocean: concentration and isotopic composition. Deep Sea Research 24, 1005 – 1017. doi:https://doi.org/10.1016/0146-6291(77)90571-9.

Ku, T.L., Liang, Z.C., 1984. The Dating of Impure Carbonates with Decay-Series Isotopes. Nuclear Instruments and Methods in Physics Research 223, 563–571. doi:10.1360/zd-2013-43-6-1064.

Ku, T.L., Luo, S., Lowenstein, T.K., Li, J., Spencer, R.J., 1998. U-Series Chronology of Lacustrine Deposits in Death Valley, California. Quaternary Research 50, 261–275.

Kutterolf, S., Schindlbeck, J.C., Anselmetti, F.S., Ariztegui, D., Brenner, M., Curtis, J., Schmid, D., Hodell, D., Mueller, A., Pérez, W., Schwalb, A., Frische, M., Wang, K.L., 2016. A 400-ka tephrochronological framework for Central America from Lake Petén Itzá (Guatemala) sediments. Quaternary Science Reviews 150, 200–220. doi:10.1016/j.quascirev.2016.08.023.

Lambert, F., Delmonte, B., Petit, J., Bigler, M., Kaufmann, P., Hutterli, M., Stocker, T., Ruth, U., Steffensen, J., Maggi, V., 2008. Dust-climate couplings over the past 800,000 years from the EPICA Dome C ice core. Nature 452, 616–619. doi:10.1038/nature06763.

Langmuir, D., 1978. Uranium solution-mineral equilibria at low temperatures with applications to sedimentary ore deposits. Geochimica et Cosmochimica Acta 42, 547–569. doi:10.1016/0016-7037(78)90001-7.

Li, J., Lowenstein, T.K., Brown, C.B., Ku, T.L., Luo, S., 1996. A 100 ka record of water tables and paleoclimates from salt cores, Death Valley, California. Palaeogeography, Palaeoclimatology, Palaeoecology 123, 179–203. doi:10.1016/0031-0182(95)00123-9.

Lin, J.C., Broecker, W.S., Anderson, R.F., Hemming, S., Rubenstone, J.L., Bonani, G., 1996. New 230Th/U and 14C ages from Lake Lahontan carbonates, Nevada, USA, and a discussion of the origin of initial thorium. Geochimica et Cosmochimica Acta 60, 2817–2832.

Lin, J.C., Broecker, W.S., Hemming, S.R., Hajdas, I., Anderson, R.F., Smith, G.I., Kelley, M., Bonani, G., 1998. A Reassessment of U-Th and 14C Ages for Late-Glacial High-Frequency Hydrological Events at Searles Lake, California. Quaternary Research 49, 11–23. doi:10.1006/qres.1997.1949.

Lisiecki, L.E., Raymo, M.E., 2005. A Pliocene-Pleistocene stack of 57 globally distributed benthic δ18O records. Paleoceanography 20. doi:10.1029/2004PA001071.

Lowenstein, T.K., Hein, M.C., Bobst, A.L., Jordan, T.E., Ku, T.L., Luo, S., 2003. An assessment of stratigraphic completeness in climate-sensitive closed-basin lake sediments: Salar de Atacama, Chile. Journal of Sedimentary Petrology 73, 91–104. doi:10.1306/061002730091.

Ludwig, K.R., 2003. Mathematical-Statistical Treatment of Data and Errors for 230Th/U Geochronology. Reviews in Mineralogy and Geochemistry 52, 631–656. doi:10.2113/0520631.

Ludwig, K.R., 2012. User's Manual for Isoplot Version 3.75–4.15: A Geochronological Toolkit for Microsoft Excel. Technical Report 5. Berkeley Geochronological Center Special Publication.

Ludwig, K.R., Paces, J.B., 2002. Uranium-series dating of pedogenic silica and carbonate, Crater Flat, Nevada. Geochimica et Cosmochimica Acta 66, 487–506. doi:10.1016/S0016-7037(01)00786-4.

Luo, S., Ku, T.L., 1991. U-series isochron dating: A generalized method employing total-sample dissolution. Geochimica et Cosmochimica Acta 55, 555–564. doi:10.1016/0016-7037(91)90012-T.

Lyle, M., 1983. The brown-green color transition in marine sediments: A marker of the Fe(III)-Fe(II) redox boundary. Limnol. Oceanogr. 28, 1026–1033. doi:10.4319/lo.1983.28.5.1026.

Ma, Z., Wang, Z., Liu, J., Yuan, B., Xiao, J., Zhang, G., 2004. U-series chronology of sediments associated with Lake Quaternary fluctuations, Balikun Lake, northwestern China. Quaternary International 121, 89–98. doi:10.1016/j.quaint.2004.01.025.

Mackay, A.W., Bezrukova, E.V., Boyle, J.F., Holmes, J.A., Panizzo, V.N., Piotrowska, N., Shchetnikov, A., Shilland, E.M., Tarasov, P., White, D., 2013. Multiproxy evidence for abrupt climate change impacts on terrestrial and freshwater ecosystems in the Ol'khon region of Lake Baikal, central Asia. Quaternary International 290-291, 46–56. doi:10.1016/j.quaint.2012.09.031.

McGee, D., Quade, J., Edwards, R.L., Broecker, W.S., Cheng, H., Reiners, P.W., Evenson, N., 2012. Lacustrine cave carbonates: Novel archives of paleohydrologic change in the Bonneville Basin (Utah, USA). Earth and Planetary Science Letters 351-352, 182–194. doi:10.1016/j.epsl.2012.07.019.

McIntyre, G., Brooks, C., Compston, W., Turek, A., 1966. The statistical assessment of Rb-Sr isochrons. Journal of Geophysical Research 71, 5459–5468. doi:10.1029/JZ071i022p05459.

McLaren, S.J., Rowe, P.J., 1996. The reliability of uranium-series mollusc dates from the western Mediterranean basin. Quaternary Science Reviews 15, 709–717. doi:10.1016/0277-3791(96)00032-7.

Metcalfe, S., Say, A., Black, S., McCulloch, R., O'Hara, S., 2002. Wet conditions during the last glaciation in the Chihuahuan Desert, Alta Babicora Basin, Mexico. Quaternary Research 57, 91–101. doi:10.1006/qres.2001.2292.

Mikutta, C., Langner, P., Bargar, J.R., Kretzschmar, R., 2016. Tetra-and hexavalent uranium forms bidentate-mononuclear complexes with particulate organic matter in a naturally uranium-enriched peatland. Environmental science & technology 50, 10465–10475. doi:10.1021/acs.est.6b03688.

Mix, A.C., Harris, S.E., Janecek, T.R., 1995. Estimating lithology from nonintrusive reflectance spectra: Leg 138. Proceedings of the Ocean Drilling Program, Scientific Results 138.

Nagao, S., Nakashima, S., 1992. The factors controlling vertical color variations of North Atlantic Madeira Abyssal Plain sediments. Marine Geology 109, 83–94. doi:10.1016/0025-3227(92)90222-4.

Nowaczyk, N.R., Haltia, E.M., Ulbricht, D., Wennrich, V., Sauerbrey, M.A., Rosén, P., Vogel, H., Francke, A., Meyer-Jacob, C., Andreev, A.A., Lozhkin, A.V., 2013. Chronology of Lake El'gygytgyn sediments – A combined magnetostratigraphic, palaeoclimatic and orbital tuning study based on multi-parameter analyses. Climate of the Past 9, 2413–2432. doi:10.5194/cp-9-2413-2013.

Osmond, J.K., May, J.P., Tanner, W.F., 1970. Age of the Cape Kennedy Barrier-and-Lagoon Complex. Journal of Geophysical Research 75, 469–479. doi:10.1029/JB075i002p00469.

Palacios-Fest, M.R., Alin, S.R., Cohen, A.S., Tanner, B., Heuser, H., 2005. Paleolimnological investigations of anthropogenic environmental change in Lake Tanganyika: IV. Lacustrine paleoecology. Journal of Paleolimnology 34, 51–71. doi:10.1007/s10933-005-2397-1.

Peng, T.H., Goddard, J.G., Broecker, W.S., 1978. A Direct Comparison of 14C and 230Th Ages at Searles Lake, California. Quaternary Research 9, 319–329. doi:10.1016/0033-5894(78)90036-4.

Pérez, L., Lorenschat, J., Bugja, R., Brenner, M., Scharf, B., Schwalb, A., 2010. Distribution, diversity and ecology of modern freshwater ostracodes (Crustacea), and hydrochemical characteristics of Lago Petén Itzá, Guatemala. Journal of Limnology 69, 146–159. doi:10.3274/JL10-69-1-14.

Petit, J., Jouzel, J., Raynaud, D., Barkov, N., Barnola, J.M., Basile, I., Bender, M., Chappellaz, J., Davis, M., Delaygue, G., Delmotte, M., Kotlyakov, V., Legrand, M., Lipenkov, V., Lorius, C., Pépin, L., Ritz, C., Saltzman, E., Stievenard, M., 1999. Climate and atmospheric history of the past 420,000 years from the Vostok ice core, Antarctica. Nature 399, 429–436. doi:10.1038/20859.

Phillips, F.M., Zreda, M.G., Ku, T.L., Luo, S., Huang, Q., Elmore, D., Kubik, P.W., Sharma, P., 1993. 230Th/234U and 36Cl dating of evaporite deposits from the western Qaidam Basin, China: Implications for glacial-period dust export from Central Asia. Geological Society of America Bulletin 105, 1606–1616. doi:10.1130/0016-7606(1993)105<1606:TUACDO>2.3.CO;2.

Plater, A.J., Ivanovich, M., Dugdale, R.E., 1992. Uranium series disequilibrium in river sediments and waters: the significance of anomalous activity ratios. Applied Geochemistry 7, 101–110. doi:10.1016/0883-2927(92)90029-3.

Porcelli, D., Andersson, P., Wasserburg, G., Ingri, J., Baskaran, M., 1997. The importance of colloids and mires for the transport of uranium isotopes through the Kalix River watershed and Baltic Sea. Geochimica et Cosmochimica Acta 61, 4095–4113. doi:10.1016/S0016-7037(97)00235-4.

Powell, R., Hergt, J., Woodhead, J., 2002. Improving isochron calculations with robust statistics and the bootstrap. Chemical Geology 185, 191–204. doi:10.1016/S0009-2541(01)00403-X.

Prokopenko, A.A., Hinnov, L.A., Williams, D.F., Kuzmin, M.I., 2006. Orbital forcing of continental climate during the Pleistocene: a complete astronomically tuned climatic record from Lake Baikal, SE Siberia. Quaternary Science Reviews 25, 3431–3457. doi:10.1016/j.quascirev.2006.10.002.

Przybylowicz, W., Schwarcz, H.P., Latham, A.G., 1991. Dirty calcites 2. Uranium-series dating of artificial calcite-detritus mixtures. Chemical Geology: Isotope Geoscience Section 86, 161–178. doi:10.1016/0168-9622(91)90060-A.

Reeder, R.J., Nugent, M., Lamble, G.M., Tait, C.D., Morris, D.E., 2000. Uranyl Incorporation into Calcite and Aragonite: XAFS and Luminescence Studies. Environmental Science & Technology 34, 638–644. doi:10.1021/es990981j.

Reeder, R.J., Nugent, M., Tait, C.D., Morris, D.E., Heald, S.M., Beck, K.M., Hess, W.P., Lanzirotti, A., 2001. Coprecipitation of Uranium(VI) with Calcite: XAFS, micro-XAS, and luminescence characterization. Geochimica et Cosmochimica Acta 65, 3491–3503. doi:10.1016/S0016-7037(01)00647-0.

Roberts, H.M., Bryant, C.L., Huws, D.G., Lamb, H.F., 2018. Generating long chronologies for lacustrine sediments using luminescence dating: a 250,000 year record from Lake Tana, Ethiopia. Quaternary Science Reviews 202, 66–77. doi:10.1016/j.quascirev.2018.10.037.

Robinson, L.F., Adkins, J.F., Fernandez, D.P., Burnett, D.S., Wang, S.L., Gagnon, A.C., Krakauer, N., 2006. Primary U distribution in scleractinian corals and its implications for U series dating. Geochemistry, Geophysics, Geosystems 7. doi:10.1029/2005GC001138.

Robinson, L.F., Henderson, G.M., Hall, L., Matthews, I., 2004. Climatic Control of Riverine and Seawater Uranium-Isotope Ratios. Science 305, 851–854. doi:10.1126/science.1099673.

Robinson, L.F., Henderson, G.M., Slowey, N.C., 2002. U-Th dating of marine isotope stage 7 in Bahamas slope sediments. Earth and Planetary Science Letters 196, 175–187. doi:10.1016/S0012-821X(01)00610-0.

Rodbell, D.T., Abbott, M.B., the 2011 ICDP Lake Junin Working Group, 2012. Workshop on drilling of Lake Junin, Peru: Potential for development of a continuous tropical climate record. Scientific Drilling 3, 58–60. doi:10.2204/iodp.sd.13.10.2011.

Rosholt, J.H., 1976. 230Th/234U dating of travertine and caliche rinds. Geological Society of America Abstracts with Programs 8, 1076.

Rowe, P.J., Richards, D.A., Atkinson, T.C., Bottrell, S.H., Cliff, R.A., 1997. Geochemistry and radiometric dating of a Middle Pleistocene peat. Geochimica et Cosmochimica Acta 61, 4201–4211. doi:10.1016/S0016-7037(97)00213-5.

Rudnick, R., Gao, S., 2003. Composition of the Continental Crust, in: Treatise on Geochemistry. Elsevier. volume 3, pp. 1–64. doi:10.1016/B0-08-043751-6/03016-4.

Sarin, M.M., Krishnaswami, S., Somayajulu, B., Moore, W.S., 1990. Chemistry of uranium, thorium, and radium isotopes in the Ganga-Brahmaputra river system: Weathering processes and fluxes to the Bay of Bengal. Geochimica et Cosmochimica Acta 54, 1387–1396. doi:10.1016/0016-7037(90)90163-F.

Schmeide, K., Pompe, S., Bubner, M., Heise, K.H., Bernhard, G., Nitsche, H., 2000. Uranium(VI) sorption onto phyllite and selected minerals in the presence of humic acid. Radiochimica Acta 88, 723–728. doi:10.1524/ract.2000.88.9-11.723.

Schnurrenberger, D., Russell, J., Kelts, K., 2003. Classification of lacustrine sediments based on sedimentary components. Journal of Paleolimnology 29, 141–154. doi:10.1023/A:1023270324800.

Schoene, B., Condon, D.J., Morgan, L., McLean, N., 2013. Precision and Accuracy in Geochronology. Elements 9, 19–24. doi:10.2113/gselements.9.1.19.

Scholz, D., Tolzmann, J., Hoffmann, D.L., Jochum, K.P., Spötl, C., Riechelmann, D.F., 2014. Diagenesis of speleothems and its effect on the accuracy of 230Th/U-ages. Chemical Geology 387, 74–86. doi:10.1016/j.chemgeo.2014.08.005.

Schwalb, A., Locke, S.M., Dean, W.E., 1995. Ostracode δ^{18}O and δ^{13}C evidence of Holocene environmental changes in the sediments of two Minnesota lakes. Journal of Paleolimnology 14, 281–296. doi:10.1007/BF00682429.

Schwarcz, H.P., Latham, A.G., 1989. Dirty calcites 1. Uranium-series dating of contaminated calcite using leachates alone. Chemical Geology: Isotope Geoscience Section 80, 35–43. doi:10.1016/0168-9622(89)90046-8.

Seltzer, G., Rodbell, D., Burns, S., 2000. Isotopic evidence for late Quaternary climatic change in tropical South America. Geology 28, 35. doi:10.1130/0091-7613(2000)28<35:IEFLQC>2.0.CO;2.

Shanahan, T.M., Peck, J.A., McKay, N., Heil, C.W., King, J., Forman, S.L., Hoffmann, D.L., Richards, D.A., Overpeck, J.T., Scholz, C., 2013. Age models for long lacustrine sediment records using multiple dating approaches – An example from Lake Bosumtwi, Ghana. Quaternary Geochronology 15, 47–60. doi:10.1016/j.quageo.2012.12.001.

Shen, C.C., Lawrence Edwards, R., Cheng, H., Dorale, J.A., Thomas, R.B., Bradley Moran, S., Weinstein, S.E., Edmonds, H.N., 2002. Uranium and thorium isotopic and concentration measurements by magnetic sector inductively coupled plasma mass spectrometry. Chemical Geology 185, 165–178. doi:10.1016/S0009-2541(01)00404-1.

Shen, C.C., Wu, C.C., Cheng, H., Edwards, R.L., Hsieh, Y.T., Gallet, S., Chang, C.C., Li, T.Y., Lam,

D.D., Kano, A., Hori, M., Spötl, C., 2012. High-precision and high-resolution carbonate 230Th dating by MC-ICP-MS with SEM protocols. Geochimica et Cosmochimica Acta 99, 71 – 86. doi:10.1016/j.gca.2012.09.018.

Siegel, D.I., Rodbell, D.T., Mark, B., Brigham-Grette, J., Smith, J., 2005. Memorial to geoffrey owen seltzer (1959–2005). Geological Society of America Memorials 34.

Skrivanek, A., Li, J., Dutton, A., 2018. Relative sea-level change during the Last Interglacial as recorded in Bahamian fossil reefs. Quaternary Science Reviews 200, 160–177. URL: https://linkinghub.elsevier.com/retrieve/pii/S0277379118304384, doi:10.1016/j.quascirev.2018.09.033.

Smith, A.J., Delorme, L.D., 2010. Ostracoda. Ecology and Classification of North American Freshwater Invertebrates , 725–771doi:10.1016/B978-0-12-374855-3.00019-4.

Smith, J.A., Finkel, R.C., Farber, D.L., Rodbell, D.T., Seltzer, G.O., 2005a. Moraine preservation and boulder erosion in the tropical Andes: Interpreting old surface exposure ages in glaciated valleys. Journal of Quaternary Science 20, 735–758. doi:10.1002/jqs.981.

Smith, J.A., Seltzer, G.O., Farber, D.L., Rodbell, D.T., Finkel, R.C., 2005b. Early local last glacial maximum in the tropical Andes. Science 308, 678–681. doi:10.1126/science.1107075.

Stein, M., Goldstein, S.L., 2006. U-Th and radiocarbon chronologies of late Quaternary lacustrine records of the Dead Sea basin: Methods and applications, in: Enzel, Y., Agnon, A., Stein, M. (Eds.), New frontiers in Dead Sea paleoenvironmental research: Geological Society of America Special Paper 401. Geological Society of America. volume 401, pp. 141–154. doi:10.1130/2006.2401(09).

Stirling, C.H., Andersen, M.B., 2009. Uranium-series dating of fossil coral reefs: Extending the sea-level record beyond the last glacial cycle. Earth and Planetary Science Letters 284, 269–283. doi:10.1016/j.epsl.2009.04.045.

Stockhecke, M., Kwiecien, O., Vigliotti, L., Anselmetti, F.S., Beer, J., Çağatay, M.N., Channell, J.E., Kipfer, R., Lachner, J., Litt, T., Pickarski, N., Sturm, M., 2014. Chronostratigraphy of the 600,000 year old continental record of Lake Van (Turkey). Quaternary Science Reviews 104, 8–17. doi:10.1016/j.quascirev.2014.04.008.

Thompson, W.G., Spiegelman, M.W., Goldstein, S.L., Speed, R.C., 2003. An open-system model for U-series age determinations of fossil corals. Earth and Planetary Science Letters 210, 365–381. doi:10.1016/S0012-821X(03)00121-3.

Thurber, D.L., 1962. Anomalous U^{234}/U^{238} in nature. Journal of Geophysical Research 67, 4518–4520. doi:10.1029/JZ067i011p04518.

Tomlinson, C.W., 1916. The origin of red beds: a study of the conditions of origin of the Permo-Carboniferous and Triassic red beds of the western United States. The Journal of Geology 24, 153–179. doi:10.1086/622326.

Torfstein, A., Goldstein, S.L., Kagan, E.J., Stein, M., 2013. Integrated multi-site U-Th chronology of the last glacial Lake Lisan. Geochimica et Cosmochimica Acta 104, 210–231. doi:10.1016/j.gca.2012.11.003.

Torfstein, A., Goldstein, S.L., Kushnir, Y., Enzel, Y., Haug, G., Stein, M., 2015. Dead Sea drawdown and monsoonal impacts in the Levant during the last interglacial. Earth and Planetary Science Letters 412, 235–244. doi:10.1016/j.epsl.2014.12.013.

Trachsel, M., Telford, R.J., 2017. All age-depth models are wrong, but are getting better. The Holocene 27, 860–869. doi:10.1177/0959683616675939.

Van Der Wijk, A., El-Daoushy, F., Arends, A.R., Mook, W.G., 1986. Dating peat with U/Th disequilibrium: Some geochemical considerations. Chemical Geology: Isotope Geoscience Section 59, 283–292. doi:10.1016/0168-9622(86)90077-1.

Vermeesch, P., 2018. IsoplotR: A free and open toolbox for geochronology. Geoscience Frontiers 9, 1479–1493. doi:10.1016/j.gsf.2018.04.001, arXiv:0-387-31073-8.

Wang, J., Fang, X., Appel, E., Zhang, W., 2013. Magnetostratigraphic and radiometric constraints on salt formation in the Qaidam Basin, NE Tibetan Plateau. Quaternary Science Reviews 78, 53–64. doi:10.1016/j.quascirev.2013.07.017.

Wang, Y.J., Cheng, H., Edwards, R.L., An, Z.S., Wu, J.Y., Shen, C.C., Dorale, J.A., 2001. A high-resolution absolute-dated late Pleistocene Monsoon record from Hulu Cave, China. Science 294, 2345–2348. doi:10.1126/science.1064618.

Wendt, I., Carl, C., 1991. The statistical distribution of the mean squared weighted deviation. Chemical Geology: Isotope Geoscience section 86, 275–285. doi:10.1016/0168-9622(91)90010-T.

Winograd, I.J., Coplen, T.B., Landwehr, J.M., Riggs, A.C., Ludwig, K.R., Szabo, B.J., Kolesar, P.T., Revesz, K.M., 1992. Continuous 500,000-Year Climate Record From Vein Calcite in Devils-Hole, Nevada. Science 258, 255–260. doi:10.1126/science.258.5080.255.

Wipperfurth, S.A., Guo, M., Šrámek, O., McDonough, W.F., 2018. Earth's chondritic th/u: Negligible fractionation during accretion, core formation, and crust–mantle differentiation. Earth and Planetary Science Letters 498, 196–202. doi:10.1016/j.epsl.2018.06.029.

Wong, B., 2011. Points of view: Color blindness. Nature Methods 8. doi:10.1038/nmeth.1618.

Woods, A., Rodbell, D., Abbott, M., Hatfield, R.G., Chen, C.Y., Lehmann, S., McGee, D., Weidhaas, N., Tapia, P.M., Valero-Garcés, B.L., Bush, M., Stoner, J.S., 2019. Abrupt Arctic Warming Repeatedly Led to Prolonged Drought and Glacial Retreat in the Tropical Andes During the Last Glacial Cycle. EarthArXiv doi:10.31223/osf.io/7hd3a.

Wright, H.E., 1983. Late-Pleistocene Glaciation and Climate around the Junín Plain, Central Peruvian Highlands. Geografiska Annaler. Series A, Physical Geography 65, 35–43. doi:10.2307/520719.

Wrozyna, C., Frenzel, P., Daut, G., Mäusbacher, R., Zhu, L., Schwalb, A., 2012. Holocene Lake-Level Changes of Lake Nam Co, Tibetan Plateau, Deduced from Ostracod Assemblages and δ^{18}O and δ^{13}C Signatures of Their Valves. Developments in Quaternary Science 17, 281–295. doi:10.1016/B978-0-444-53636-5.00016-0.

York, D., 1968. Least squares fitting of a straight line with correlated errors. Earth and Planetary Science Letters 5, 320–324. doi:10.1016/S0012-821X(68)80059-7.

Supplementary Materials

S1. Further details of U-Th measurements, and methods of U-Th dating of materials from 1996 piston core

Samples from the PLJ-1 core were processed from March 2016 to July 2019. As mentioned in the main text, sample powders were spiked with a ^{229}Th-^{233}U-^{236}U isotope tracer. The tracer was made in-house by mixing an IRMM-3636a reference solution (a 1:1 ^{233}U-^{236}U double spike) with a ^{229}Th solution purified from ^{233}U by Aaron Pietruszka (Univ. of Hawaii at Manoa). The isotopic composition of this tracer was then calibrated by combining it with a U-Th gravimetric standard prepared from the New Brunswick Laboratories CRM 112-A uranium metal isotopic standard and an Ames Laboratory thorium metal bar, and then measuring the ^{238}U/^{236}U and ^{232}Th/^{229}Th in the resulting mixed solution.

Replicate analyses from the PLJ-1 core were processed in 21 batches. Powders were dissolved in Teflon beakers cleaned via a boiling-washing procedure with concentrated HNO_3, HCl, and aqua regia. Total procedural blanks were included in each chemistry set and were, on average, 0.13 ± 0.28 fg ^{230}Th, 5.6 ± 7.8 pg ^{232}Th, 0.48 ± 0.91 fg ^{234}U, and 7.6 ± 8.3 pg ^{238}U. The large standard deviations reflect the impact of ∼5 batches for which high blanks were observed. For added context, the median values for the procedural blanks was 0.04 fg ^{230}Th, 2.4 ^{232}Th, 0.09 fg ^{234}U, and 4.0 pg ^{238}U. All analyses were corrected for the contribution from procedural blanks.

On the Nu Plasma II-ES multi-collector ICP-MS at MIT, uranium solutions ranging from 5–40 ppb in concentration and thorium solutions ranging <1–30 ppb in concentration were measured separately. For uranium, the intensities of ^{238}U, ^{236}U, ^{235}U, and ^{233}U were measured on Faraday detectors while ^{234}U was measured on the Secondary Electron Multiplier (SEM) detector. For thorium, ^{232}Th and ^{229}Th were measured on Faraday detectors and ^{230}Th on the SEM detector. The Faraday cup measuring ^{233}U and ^{229}Th had a 10^{12} Ohm resistor in order to measure beam intensities as low as 5 mV without compromising the signal-to-noise ratio.

In addition to being corrected for mass bias and variable SEM yield via bracketing uranium and thorium standards, reported ratios were also corrected for instrument background by measuring 2% HNO_3 solution blanks bracketing each sample and standard analysis. Reported ratios were also corrected for dead time on the ion counter and peak tailing from ^{238}U, ^{236}U, ^{235}U, and ^{232}Th. We also correct for uranium hydride interference with ^{234}U (^{233}U-H$^+$). To date, we have not observed a relationship between mass bias or ion counter gain with signal intensity on this instrument. Measured isotope ratios were also corrected for analyte isotopes contributed by the spike. The uncertainties associated with all these corrections are included in the reported uncertainties.

In October 2016, four aliquots of the GC-1 secular equilibrium standard from Cheng et al. (2013) were prepared and analyzed at MIT applying the same methods as those described in this work. The results gave a mean ^{230}Th/^{238}U activity ratio of 1.001 ± 0.002 and a mean ^{234}U/^{238}U activity ratio of 1.0000 ± 0.0008.

U-Th measurements on materials from the 1996 core were performed at the University of Minnesota. For the first set of samples, processed in approximately 1999, mollusc shell fragments were removed prior to chemical processing. For the second set processed in 2011, mollusc shell fragments were not comprehensively removed. Sample preparation was identical to the procedures described in Section 3.2. Samples for the first set were analyzed on a Finnigan Element I using methods described in Shen et al. (2002). Samples for the second set were analyzed using a ThermoScientific Neptune multi-collector ICP-MS in peak-jumping mode using methods described in Shen et al.

(2012) and Cheng et al. (2013).

S2. Methods of other datasets used to interpret U-Th data

Elemental concentration data. We measured 55 sediment samples for elemental concentrations of Ca, Mg, Sr, Al, Ti, P, V, Mn, and Fe. Samples of ∼1–2 mg in weight were dissolved and diluted in 3% HNO_3 and then measured on an Agilent 7900 ICP-MS at the MIT Center for Environmental and Health Sciences. Sample analyses were bracketed by a multi-element standard. Two measurements each were also made on two certified multi-element reference standards, PACS-2 and BCR-2. Data were corrected for blank intensities. Uncertainties for each element were determined by calculating the average percent difference between recommended values and measured values in PACS-2 and BCR-2, and then applying the larger percent difference on measured sample values. For example, the average percent difference between measured and recommended values in Mg (wt %) was 6% for PACS-2 and 2% for BCR-2; thus, all Mg measurements for samples were assigned an uncertainty of 6% of the measured Mg value. Of the 55 samples analyzed, 48 corresponded to U-Th analyses.

Total Inorganic Carbon/Total Organic Carbon. We measured weight percentage total carbon (TC) and weight percentage total inorganic carbon (TIC) by coulometry. For the measurement of TC, we combusted samples at 1000°C using a UIC 5200 automated furnace, and analyzed the resultant CO_2 by coulometry using a UIC 5014 coulometer. Similarly, we measured TIC by acidifying samples with 10% H_3PO_4 using an Automate acidification module and measured the resultant CO_2 by coulometry. We calculated weight percentage total organic carbon (TOC) from TOC = TC–TIC; weight percentage TIC was converted to percent calcite based on stoichiometry.

Color reflectance spectrophotometry. Color reflectance data were measured using a Geotek multi-sensor automated core logger (MSCL-XYZ) on split core sections at LacCore. To calculate sediment optical lightness, we took the sum total of light in the visible region of the electromagnetic spectrum, between 400 and 700 nm, following Balsam et al. (1999).

Mineralogy. In order to characterize the carbonate mineralogy of the drill core and to discern possible mineralogical differences between endogenic and detrital $CaCO_3$, 25 samples were selected from intervals with variable $CaCO_3$ abundance (0–85%) from throughout the core. In addition, 6 samples of carbonate bedrock from within the Junín drainage basin on both the eastern and western sides of the lake were also analyzed. All samples were pretreated with 35% H_2O_2 and 1M NaOH to remove organic matter and biogenic silica, respectively. Samples were then disaggregated with a solution of NaO_3P combined with ultrasonication, and then washed through 53 and 25 µm sieves to isolate fractions >53 µm, 25–53 µm, and, <25 µm. These fractions were then scanned on a Phillips PW 1840 diffractometer at 45 kW and 35 mA. Each subsample was scanned twice, wide scans were conducted at 0.6° (2Θ) per minute from 4.0–70° (2Θ) whereas narrow, more focused, scans were performed at 0.3° per minute from 28.0–31.0°.

Ostracode assemblage analysis. A total of 22 sediment samples corresponding to U-Th analyses were selected for ostracode analysis. One 0.25-g aliquot per sample was removed for most ostracode analyses. Prior to sieving, samples were gently disaggregated with three freeze/thaw cycles, since sediments were densely compacted. Then, samples were wet-sieved using a 63 µm sieve. Ostracodes were extracted with fine brushes, identified and enumerated with respect to numbers per 0.25 g dry sediment. Analysis was done using a Leica M80 stereo-microscope. Adult and juvenile intact and broken valves were differentiated. Broken valves were counted if >50% was encountered and when identification was still possible. Fossil ostracodes were identified down to

family level following procedures described in Pérez et al. (2010) and Karanovic (2012).

Additionally, we made a brief sediment description that included information of other fauna, vegetation and minerals found in the observed sediment samples.

We calculated different ratios to facilitate taphonomy interpretations and for a better understanding of processes such as remineralization and reworking in samples. The broken:intact (B:I) ratio was calculated for each sample to identify samples with relatively high numbers of broken shells. Similarly the adult:juvenile (A:I) ratio was used to identify samples with a high number of adult valves, that could indicate transportation of the lighter juvenile valves to deeper waters. The nektobenthic:benthic (NB:B) was calculated to evaluate shifts in the relative abundance of bottom-swimming versus bottom-dwelling individuals.

Shell coloration was taken into account as well when enumerating ostracode shells. We were able to distinguish 7 different shell colorations: 1. Translucent, 2. White, 3. Partly light grey, 4. Completely light grey, 5. Partly dark grey, 6. Completely dark grey, 7. Completely black. Additionally, we used a Scanning Electron Microscope (SEM) TM3000 Hitachi with BSE Detector II for taking pictures of uncoated specimens to facilitate ostracode identification and to detect elements of ostracode shells using EDX analysis. All ostracode analyses were conducted at the Institut für Geosysteme und Bioindikation (IGeo) of TU-Braunschweig.

S3. Calculation of $\delta^{234}U_{iec}$

Here we derive our formula for calculating the $\delta^{234}U$ of the initial endogenic carbonate ($\delta^{234}U_{iec}$) for a given bulk sediment sample. We make this calculation in order to account for the amount of initial detrital ^{234}U included in our samples. Our calculations assume that each sample is a mixture of two isotopically homogeneous sources—endogenic carbonate and detritus—and that the detrital component has a $^{232}Th/^{238}U$ activity ratio equivalent to the average value of the upper continental crust ($[^{232}Th/^{238}U]_{det} = 1.2 \pm 0.6$) and isotope ratios in the ^{238}U decay chain that are at secular equilibrium ($[^{234}U/^{238}U]_{det} = [^{230}Th/^{238}U]_{det} = 1.0 \pm 0.5$). The uncertainties are set to a conservative $\pm$ 50% to account for variability and unknown unknowns, following Dutton et al. (2017).

The initial uranium isotopic composition of a sample is defined as follows:

$$\left[\frac{^{234}U}{^{238}U}\right]_{initial} = \left[\frac{^{234}U}{^{238}U}\right]_{det} f_{det} + \left[\frac{^{234}U}{^{238}U}\right]_{iec} (1 - f_{det}), \tag{S1}$$

where the subscript *initial* refers to the initial isotope ratio of the sample, f_{det} is the fraction of uranium in the sample that is detrital, and brackets indicate activities. We rearrange Equation S1 and convert to delta notation to solve for $\delta^{234}U_{iec}$:

$$\delta^{234}U_{iec} = \left(\frac{[^{234}U/^{238}U]_{initial} - [^{234}U/^{238}U]_{det} \times f_{det}}{1 - f_{det}} - 1\right) \times 1000. \tag{S2}$$

Here, f_{det} is defined as follows:

$$f_{det} = \frac{^{238}U_{det}}{^{238}U_{samp}}, \tag{S3}$$

where the subscript *samp* refers to the total bulk sample and subscript *det* refers to the detrital component of the bulk sample. The unknown in the above formula is the amount of $^{238}U_{det}$, since

the amount of $^{238}U_{samp}$ is a quantity we measure. Because we also measure $^{232}Th_{samp}$, we can use these quantities and our assumption for $[^{232}Th/^{238}U]_{det}$ to solve for f_{det}:

$$f_{det} = [^{232}Th]_{samp} \times \frac{1}{[^{232}Th/^{238}U]_{det}} \times [^{238}U]_{samp}. \quad \text{(S4)}$$

Substituting Equation S4 for f_{det} in Equation S2 and using the assumed isotopic values for the detrital component of the sample, we can solve for $\delta^{234}U_{iec}$.

For the uncertainty of $\delta^{234}U_{iec}$, we propagate the uncertainties on all measured quantities and assumed detrital activity ratios through differentiation:

$$\sigma_{\delta^{234}U_{iec}} = \sqrt{\frac{\sigma_c^2(a-b)^2 + \sigma_a^2(c-1)^2 + \sigma_b^2(c-1)^2c^2}{(c-1)^4}} \times 1000, \quad \text{(S5)}$$

where a is $\left[\frac{^{234}U}{^{238}U}\right]_{initial}$, b is $\left[\frac{^{234}U}{^{238}U}\right]_{det}$, c is f_{det}, and σ is the standard deviation of each of the aforementioned quantities. To calculate σ_c, the standard deviation of f_{det}, we propagate uncertainties of the quantities shown in Equation S4.

S4. Failure to build isochrons

As mentioned in Section 4, determining dates from isochron plots failed, with high MSWDs and probabilities of fit that are close to 0% (Fig. S3). We used the Isoplot 4.1 program by Ludwig (2012) to generate isochron plots of various replicate analyses from bulk sample material, as well as analyses from adjacent clean-dirty sample pairs. Isochron plots assume that the detrital component of a sample is isotopically homogeneous. The top left panel in Fig. S3 is an idealized isochron, which shows replicate analyses following a linear trend in $^{230}Th/^{238}U$-$^{232}Th/^{238}U$ activity space (an "Osmond" isochron diagram). If analyses sufficiently contain variable proportions of detritus, the analyses will plot along a range of $^{232}Th/^{238}U$ activity values ordered from detritus-rich to detritus-poor (see varying shades of gray of ellipses in the idealized isochron of Fig. S3). The y-intercept of the line-of-best-fit through the data marks the $^{230}Th/^{238}U$ activity ratio of the detritus-free endogenic carbonate; when this information is combined with the line-of-best-fit through the same data in $^{234}U/^{238}U$-$^{232}Th/^{238}U$ activity space, which reveals the detritus-free $\delta^{234}U_{initial}$ value, we can calculate a U-Th date.

Contrasting the idealized isochron, the other panels in Fig. S3 are examples of five isochron plots of data from the PLJ-1 core. None of these data exhibit linear coherence along a mixing line, even in isochron plots which display data from adjacent clean-dirty sample pairs (see dark- versus light-colored ellipses) to ensure sufficient spread in $^{232}Th/^{238}U$ activity ratios. In these situations of "excess scatter" or "over-dispersion," a common practice is to expand the uncertainties (the size of the ellipses) by a factor of $\sqrt{MSWD}$ to account for unknown unknowns (e.g., Ludwig, 2003; Vermeesch, 2018). Unfortunately, doing so here does not improve the fit through data in a meaningful way. Thus, the scatter of these data are further evidence of the existence of open system behavior occurring in these sediments.

S5. Parameters and priors used for Bacon age-depth model

We used the following parameters and priors for our Bacon age-depth model: `thickness` = 50 cm; `acc.mean` = 80 yr/cm; `acc.shape` = 2.0; `mem.strength` = 15; and `mem.mean` = 0.8. The

age-depth model was generated by executing the following command:

```
Bacon(core = "PLJ_dates_d234U_50", acc.mean = 80, acc.shape = 2, mem.mean = 0.8,
mem.strength = 15, thick = 50, ssize = 10000, burnin = 2000, suggest = FALSE, depths.file
= TRUE, yr.max = 800000, MaxYr=781000, d.max = 8800);
```

The Baconvergence test was run and yielded a Gelman and Rubin Reduction Factor of 1.031463, which fell below the 1.05 safety threshold and indicates robust mixing of Markov Chain Monte Carlo iterations.

Trachsel and Telford (2017) tested Bacon and showed that the `thickness` parameter (the segment length) had an unpredictable effect on the size of the error envelope. They also found that the impact of different values for `thickness` was dependent on `acc.shape`, the accumulation shape prior. As Blaauw and Christen (2011) did not explicitly make any recommendations for how to choose an appropriate value for `thickness`, Trachsel and Telford (2017) suggested that the length be shorter than the mean distance between dated intervals and to choose a value that allowed for faster model convergence.

As can be seen from Fig. 16, the chronological constraints of the PLJ-1 splice are not equally spaced. The average distance between radiocarbon data in the upper 20 m of the core is 24 cm; when considering all radiometric data (radiocarbon and U-Th), the average spacing is 72 cm.

Thus, we carried out a comparison of age-depth models generated using different lengths for the `thickness` parameter, keeping the accumulation shape prior constant. Fig. S4 shows that while the difference in the mean of the age-depth models does not vary by more than 8 kyr at any point in the record, there are 5–30 kyr differences in the width of the error envelope.

Unfortunately, there is no rule of thumb or other external information that can help us determine which length for the `thickness` parameter is most appropriate. At this point, the decisions for how to generate the age-depth model are, regrettably, more of an art. Thus, we collectively settled on using 50 cm as the length for the `thickness` parameter, for no other reason other than it seeming "reasonable." We encourage others to use the chronological constraints generated in this study and others at Lake Junín to create better age-depth models with improved estimates of uncertainties.

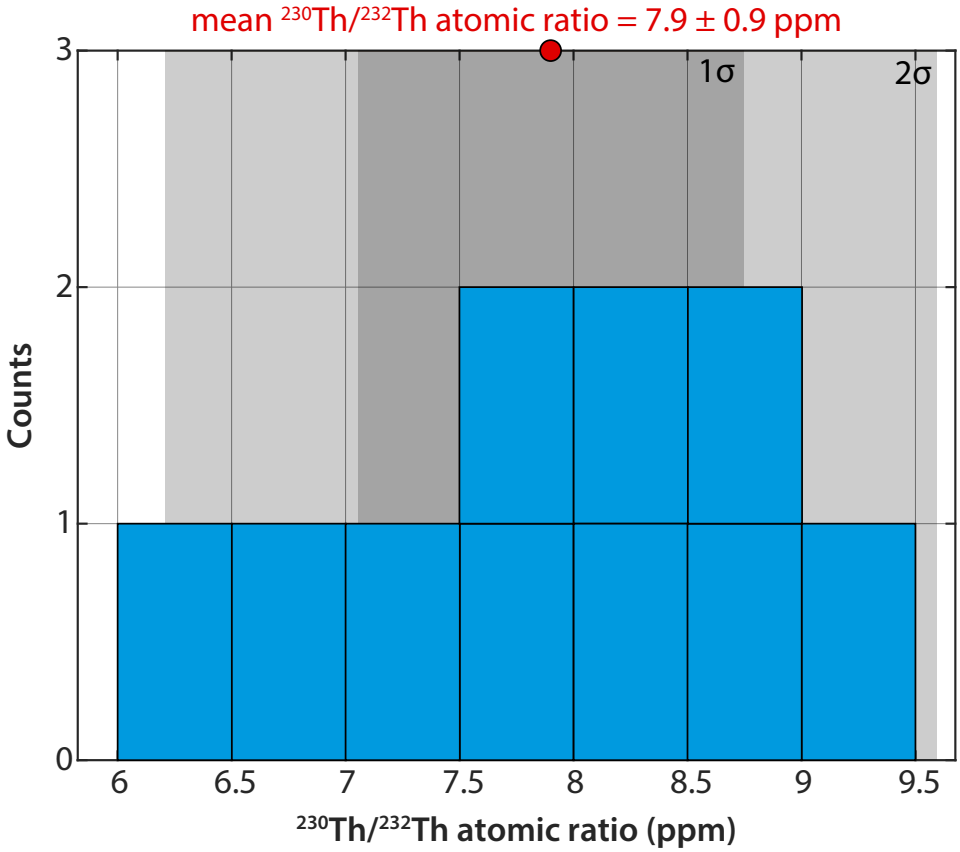

Figure S1: Histogram of ^{230}Th/^{232}Th atomic ratio of indeterminate samples from the 1996 core ($N = 10$). The average ^{230}Th/^{232}Th ratio of these samples is 7.9 ± 0.9 ppm (1-σ); the mean is represented by the red circle and the one- and two-sigma ranges of these data are represented by the shaded gray areas.

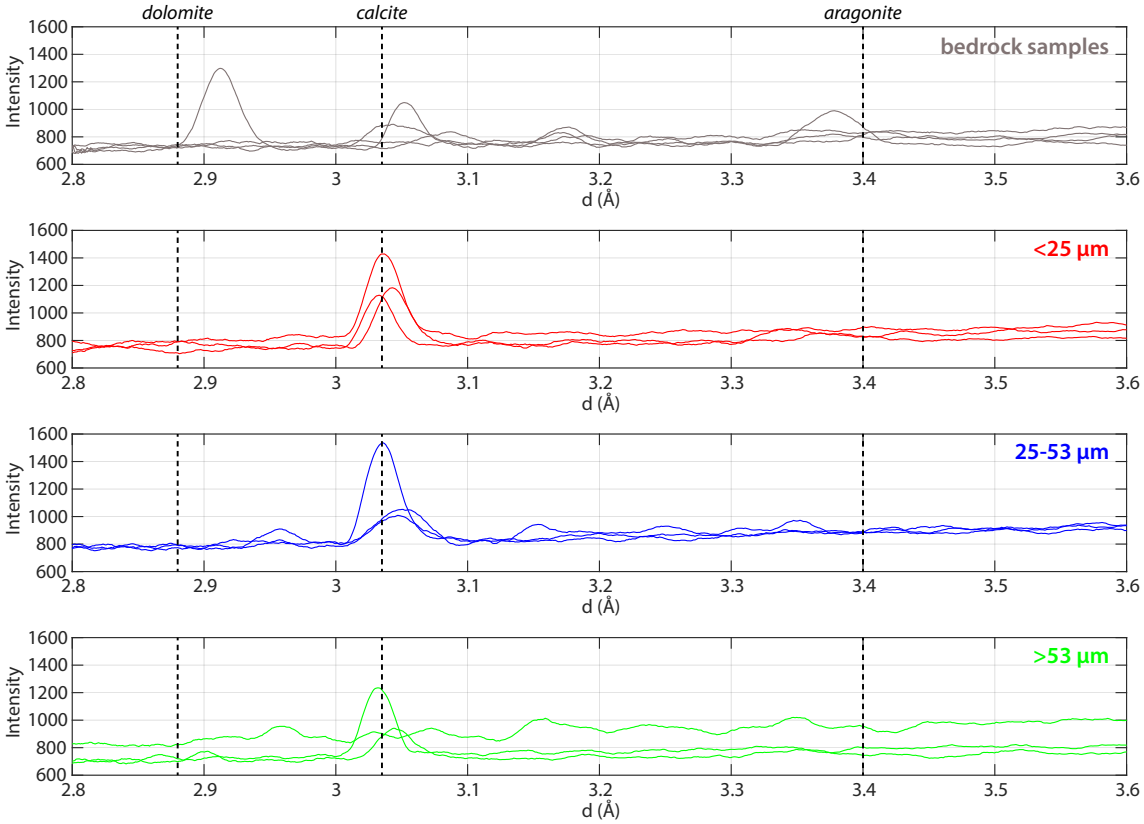

Figure S2: Comparison of XRD spectra between four bedrock carbonate samples collected within the Lake Junín drainage basin (top) and specific grain size fractions of three core catcher samples from high carbonate intervals (>70%) in the PLJ-1 core. The different grain size fractions analyzed were <25 µm, 25–53 µm, and >53 µm. The three core catcher samples plotted here are 1E-15H-3 (∼73 m CCLF), 1D-18H-3 (∼53 m CCLF), and 1D-23H-3 (∼67 m CCLF). The four bedrock samples are from Huarmipuquio (11.167°S, 76.046°W, 4115 masl), Ondors (11.098°S, 76.127°W, 4115 masl), El Mirador (11.057°S, 76.158°W, 4118 masl), and the east side of Lake Junín (10.864°S, 75.987°W, 4470 masl).

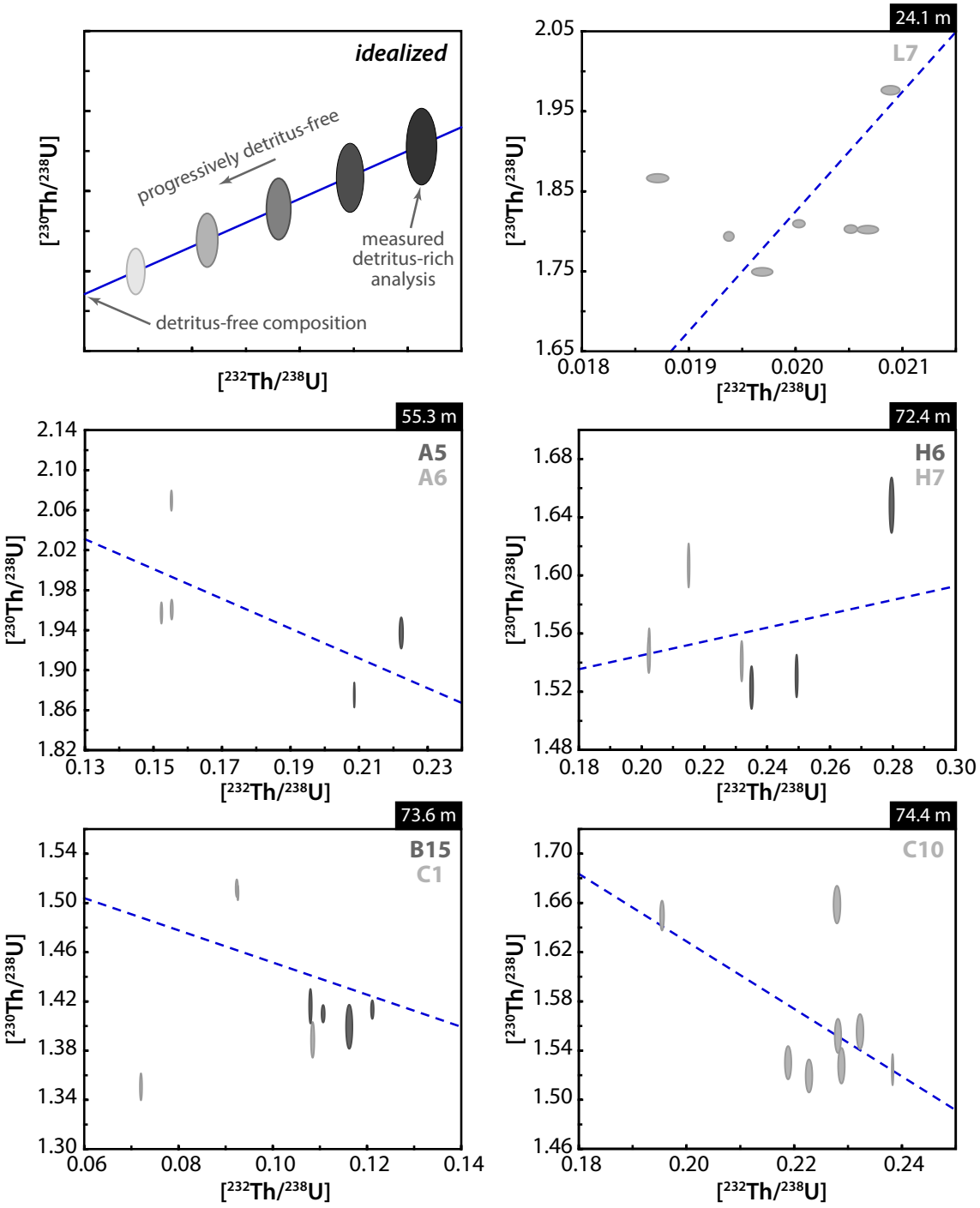

Figure S3: Examples of five isochron diagrams ("Osmond" type) made from replicates of samples from the PLJ-1 core. Each ellipse represents the 2-σ uncertainties of a replicate analysis for activity ratios $^{232}Th/^{238}U$ and $^{230}Th/^{238}U$. Blue dashed lines represent the error-weighted, least-squares regression through shown data. Top left panel shows an idealized version of an isochron plot, in which replicate analyses fall along a regression line with a high probability of fit. In the remaining five panels, the CCLF depth of the analyses is indicated in the black rectangular box, and the corresponding Sample ID is listed in the top right corner. For some plots, replicate analyses from two unique samples are shown; these are instances in which two samples immediately adjacent to one another were collected. For these sample pairs, analyses from the sample that was visually assessed as 'dirtier' are represented by a dark gray ellipse. Isochron diagrams were made using Isoplot 4.1 (Ludwig, 2003).

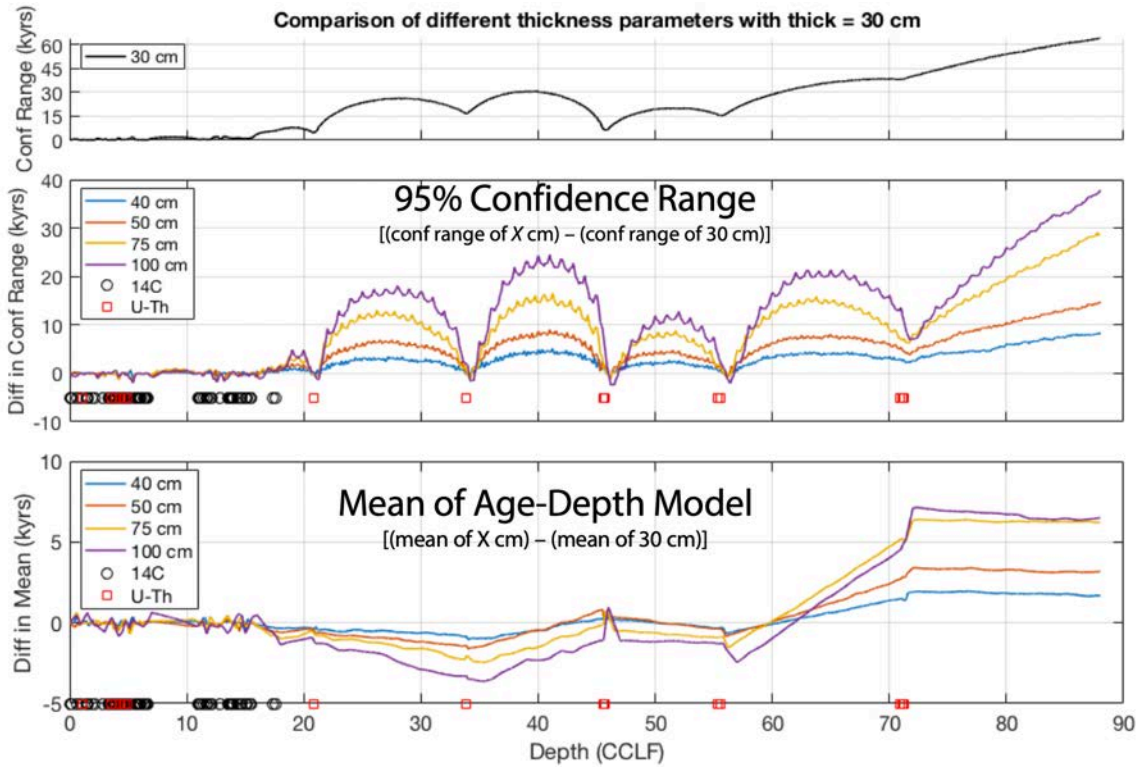

Figure S4: Comparison of the size of the 95% confidence range and mean of Bacon age-depth models run with varying lengths of the `thickness` parameter. Middle and bottom plots compare the age-depth models to the results of the model where `thickness` = 30 cm. The top plot shows the size of the 95% confidence range for the age-depth model where `thickness` = 30 cm.

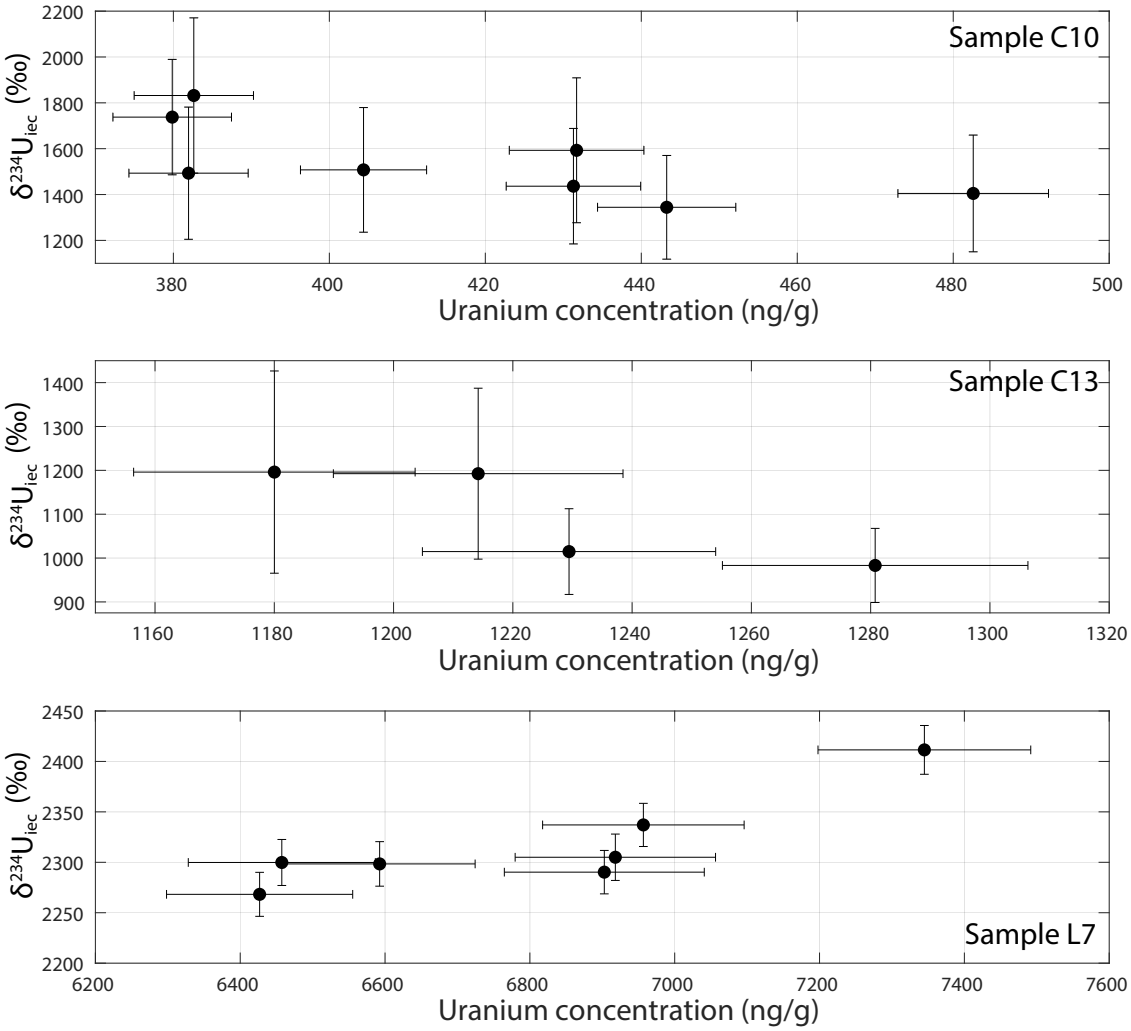

Figure S5: Comparison of uranium concentration and $\delta^{234}U_{iec}$ for three samples of the CMC facies: C10 (top), C13 (middle), and L7 (bottom). Samples C10 and C13 show some evidence of the inverse relationship between uranium concentration and $^{234}U_{iec}$, as would be predicted if there was preferential loss of ^{234}U (Robinson et al., 2006). However, L7—the sample with the highest mean uranium concentrations out of any sample analyzed—does not show a trend that is consistent with the prediction. All errors are at the 2-σ level.